

## Supplementary Information

### Rhenium Complexation-Dissociation Strategy for Synthesizing Fluorine-18 Labelled Pyridine Bidentate Structures

Mitchell A. Klenner, Bo Zhang, James Howard, Gianluca Ciancaleoni, James Howard, Helen E. Maynard-Casely, Jack Clegg, Massimiliano Massi, Benjamin H. Fraser,\* Giancarlo Pascali.\*

Email: [gianp@ansto.gov.au](mailto:gianp@ansto.gov.au), [bfr@ansto.gov.au](mailto:bfr@ansto.gov.au), [mitchk@ansto.gov.au](mailto:mitchk@ansto.gov.au).

## Table of Contents

S.1	Alternative SI Nomenclature for Rhenium Complexes and Precursors .....	3
S.2	Spectroscopy and Mass Spectrometry Data of Rhenium Complexes.....	5
S.3	Synthesis Characterisation Data of Rhenium Complexes .....	39
S.4	Radiochemical Yield vs. Reaction Temperature Plots .....	46
S.5	Computational Details of the Reaction Mechanism .....	63
S.6	Photophysical Analyses of Quantum Yields .....	69
S.7	Syntheses of Fluorinated Ligands .....	73
S.8	Instrumentation and Reagents .....	95
S.9	Microfluidic Set-Up.....	96
S.10	Ellipsoid Plots .....	97
S.11	References .....	100

## S.1 Alternative SI Nomenclature for Rhenium Complexes and Precursors

The rhenium complexes and precursors detailed within this supplementary information follow an alternative style of nomenclature as listed in Table S1. The nomenclature describes whether the ligands refers to the 2,2'-bipyridine (**BiPy**), 1,10-phenanthroline (**Phen**) or 8-hydroxyquinoline (**8HQ**) structure, alongside their substitution pattern. For example, **6ClBiPy** refers to 6-fluoro-2,2-bipyridine.

Table S1. Alternative nomenclatures used to describe the ligands and rhenium complexes in the supplementary information compared to the manuscript.

<b>Manuscript Nomenclature</b>	<b>SI Nomenclature</b>	<b>Manuscript Nomenclature</b>	<b>SI Nomenclature</b>
<b>L1a</b>	<b>BiPy</b>	[Re(CO) <sub>3</sub> ( <b>L1a</b> )Cl]	<b>ReBiPy</b>
<b>L1b</b>	<b>6ClBiPy</b>	[Re(CO) <sub>3</sub> ( <b>L1b</b> )Cl]	<b>Re6ClBiPy</b>
<b>L1c</b>	<b>5ClBiPy</b>	[Re(CO) <sub>3</sub> ( <b>L1c</b> )Cl]	<b>Re5ClBiPy</b>
<b>L1d</b>	<b>4ClBiPy</b>	[Re(CO) <sub>3</sub> ( <b>L1d</b> )Cl]	<b>Re4ClBiPy</b>
<b>L1e</b>	<b>6BrBiPy</b>	[Re(CO) <sub>3</sub> ( <b>L1e</b> )Cl]	<b>Re6BrBiPy</b>
<b>L1f</b>	<b>6FBiPy</b>	[Re(CO) <sub>3</sub> ( <b>L1f</b> )Cl]	<b>Re6FBiPy</b>
<b>L1g</b>	<b>5FBiPy</b>	[Re(CO) <sub>3</sub> ( <b>L1g</b> )Cl]	<b>Re5FBiPy</b>
<b>L1h</b>	<b>4FBiPy</b>	[Re(CO) <sub>3</sub> ( <b>L1h</b> )Cl]	<b>Re4FBiPy</b>
<b>L2a</b>	<b>Phen</b>	[Re(CO) <sub>3</sub> ( <b>L2a</b> )Cl]	<b>RePhen</b>
<b>L2b</b>	<b>2ClPhen</b>	[Re(CO) <sub>3</sub> ( <b>L2b</b> )Cl]	<b>Re2ClPhen</b>
<b>L2c</b>	<b>5ClPhen</b>	[Re(CO) <sub>3</sub> ( <b>L2c</b> )Cl]	<b>Re5ClPhen</b>
<b>L2d</b>	<b>2BrPhen</b>	[Re(CO) <sub>3</sub> ( <b>L2d</b> )Cl]	<b>Re2BrPhen</b>
<b>L2e</b>	<b>5NO<sub>2</sub>Phen</b>	[Re(CO) <sub>3</sub> ( <b>L2e</b> )Cl]	<b>Re5NO<sub>2</sub>Phen</b>
<b>L2f</b>	<b>2FPhen</b>	[Re(CO) <sub>3</sub> ( <b>L2f</b> )Cl]	<b>Re2FPhen</b>

<b>L2g</b>	<b>5FPhen</b>	[Re(CO) <sub>3</sub> (L2g)Cl]	<b>Re5FPhen</b>
<b>L3a</b>	<b>8HQ</b>	[Re(CO) <sub>3</sub> (L3a)(NCCH <sub>3</sub> )]	<b>Re8HQ</b>
<b>L3b</b>	<b>2Cl8HQ</b>	[Re(CO) <sub>3</sub> (L3b)(NCCH <sub>3</sub> )]	<b>Re2Cl8HQ</b>
<b>L3c</b>	<b>5Cl8HQ</b>	[Re(CO) <sub>3</sub> (L3c)(NCCH <sub>3</sub> )]	<b>Re5Cl8HQ</b>
<b>L3d</b>	<b>5NO<sub>2</sub>8HQ</b>	[Re(CO) <sub>3</sub> (L3d)(NCCH <sub>3</sub> )]	<b>Re5NO<sub>2</sub>8HQ</b>
<b>L3e</b>	<b>2F8HQ</b>	[Re(CO) <sub>3</sub> (L3e)(NCCH <sub>3</sub> )]	<b>Re2F8HQ</b>
<b>L3f</b>	<b>5F8HQ</b>	[Re(CO) <sub>3</sub> (L3f)(NCCH <sub>3</sub> )]	<b>Re5F8HQ</b>
<b>L3b-OBn</b>	<b>2Cl8HQ-OBn</b>	-	-
<b>L3e-OBn</b>	<b>2F8HQ-OBn</b>	-	-

## S.2 Spectroscopy and Mass Spectrometry Data of Rhenium Complexes

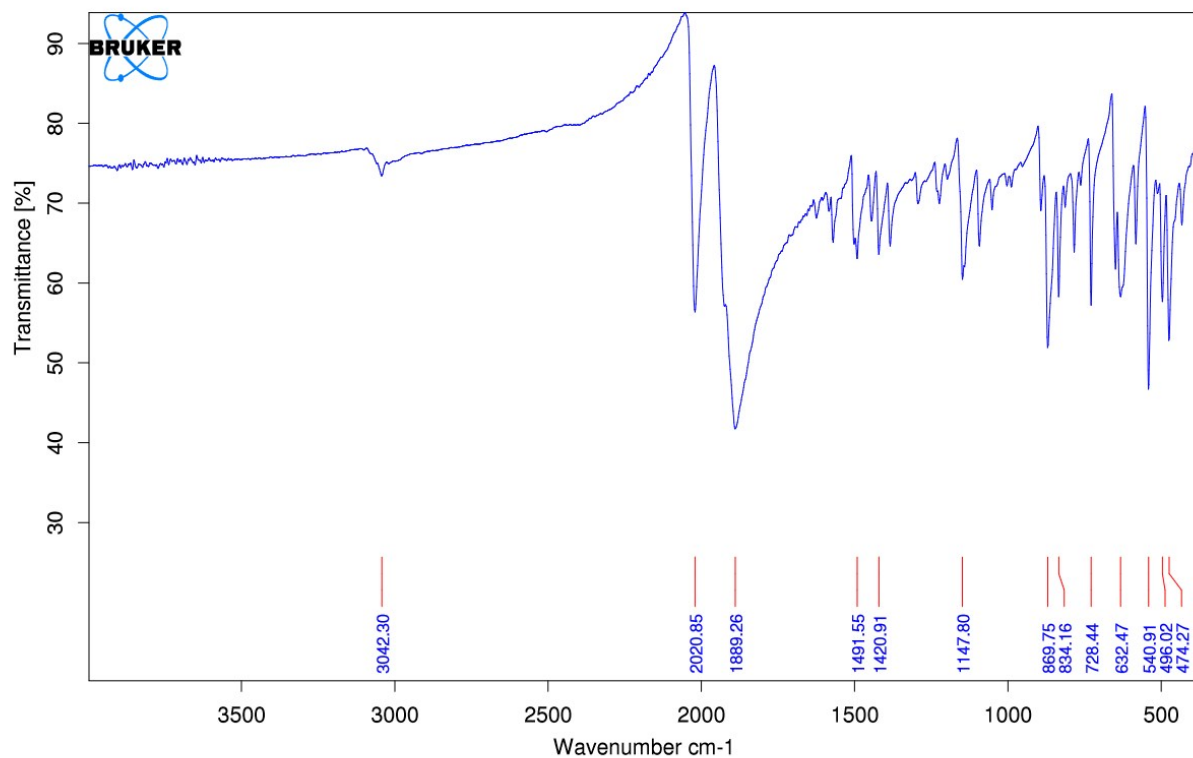


Figure S1. FTIR spectrum of **Re<sub>2</sub>CIPhen** exhibiting the two distinctive C≡O stretching IR absorption bands at 2020 cm<sup>-1</sup> and 1889 cm<sup>-1</sup> belonging to A'(1) and A'(2) & A'' coupled irreducible representations respectively. A weak sp<sup>2</sup> hybridised C–H bond stretch is also observed at 3042 cm<sup>-1</sup> from the phenanthroline ligand.

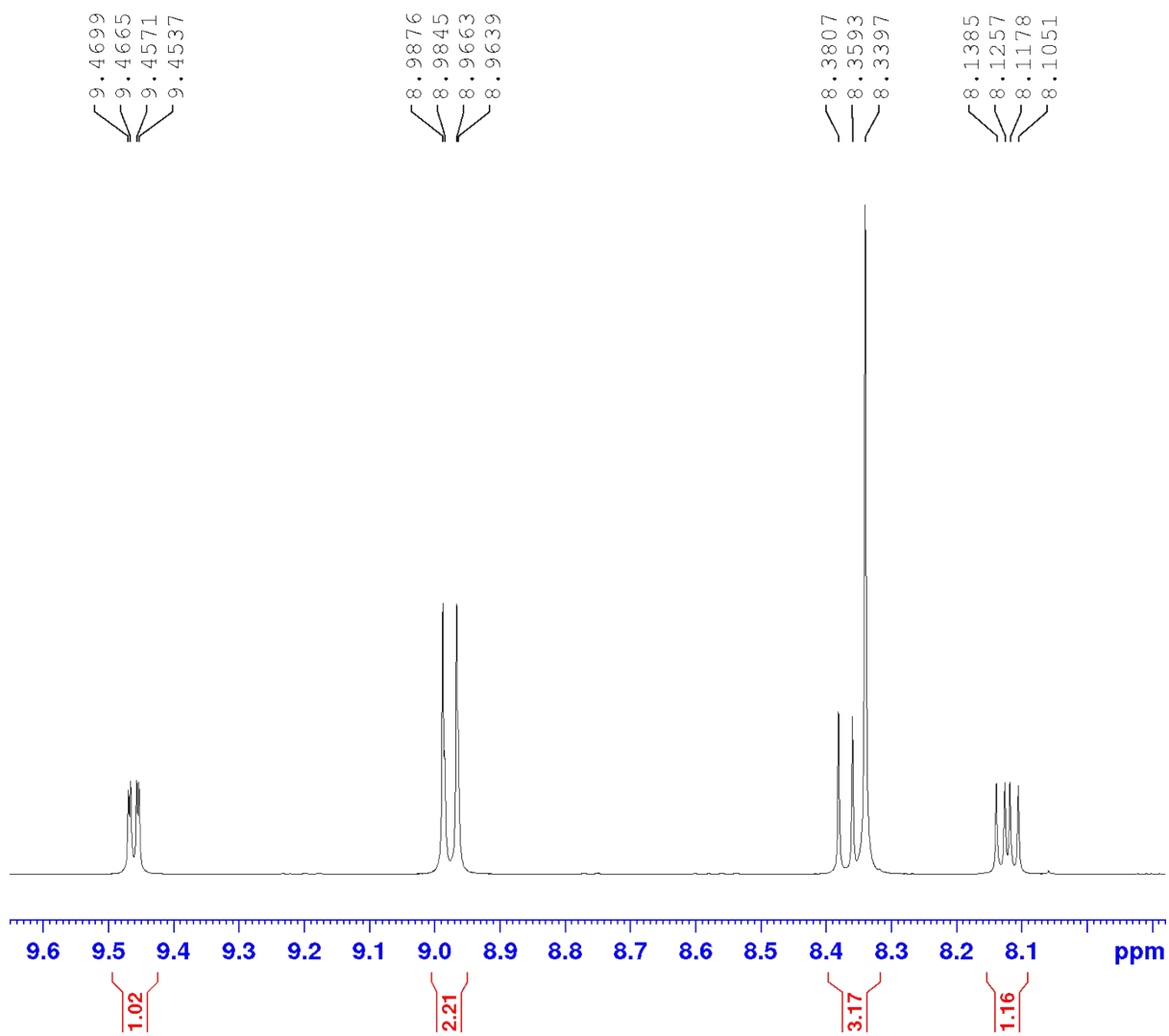


Figure S2.  $^1\text{H-NMR}$  spectrum of **Re2ClPhen** showing the expected integration for seven protons in the aromatic region, alongside simplified splitting patterns and the corresponding chemical shifts for each signal in  $\text{DMSO-d}_6$  solution.

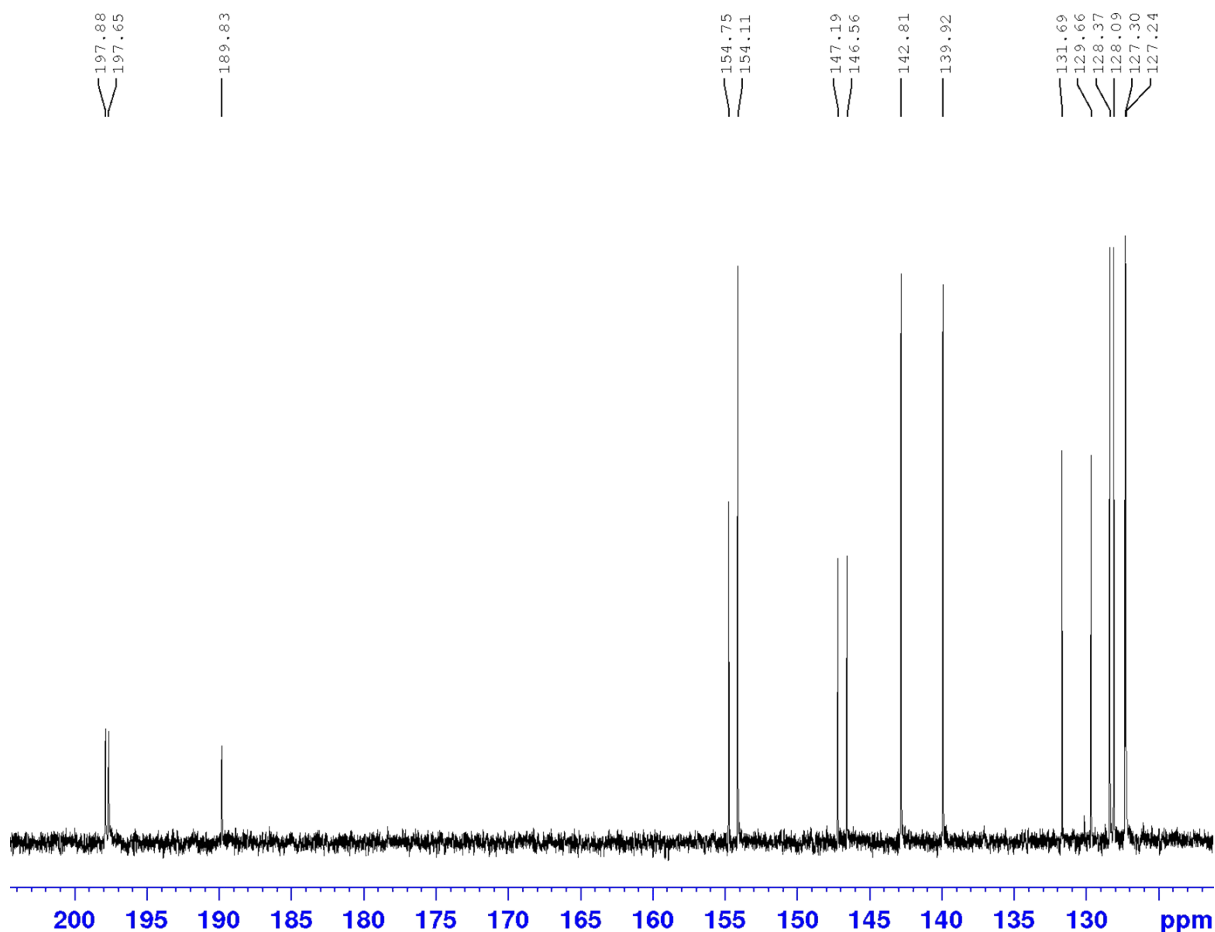


Figure S3.  $^{13}\text{C}$ -NMR spectrum of **Re<sub>2</sub>ClPhen** showing the expected fifteen carbon signals for each carbon nuclei within the molecule. The twelve carbon-13 signals between 120 – 160 ppm correspond with the carbon atoms on the phenanthroline ring, whereas the three less intense signals between 185 – 200 ppm correspond with the heavily electron withdrawn carbonyl groups bonded to the rhenium centre.

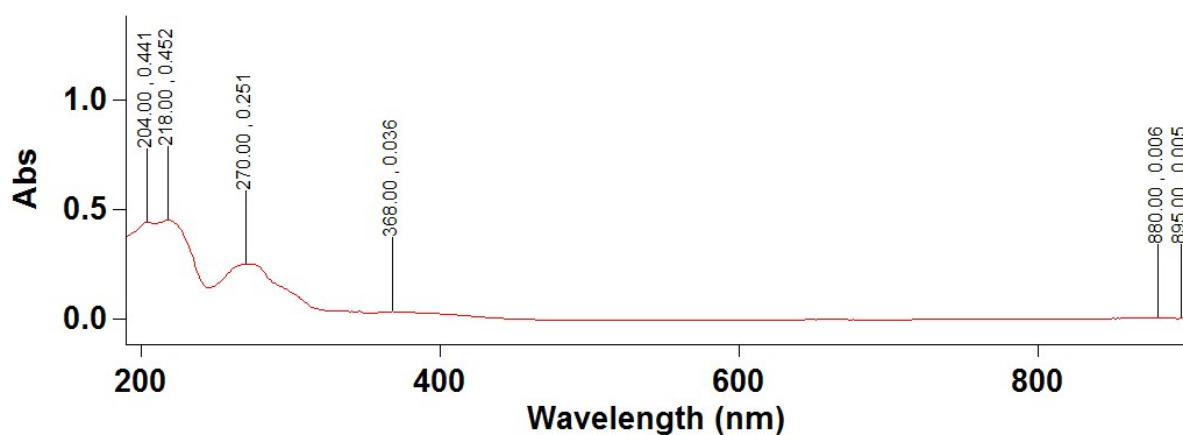


Figure S4. UV-Vis spectrum of **Re<sub>2</sub>ClPhen** exhibiting the typical  $d\pi \rightarrow \pi^*$  transition to the MLCT excited state at 368 nm. Higher energy transitions at the lower wavelengths correspond to the intraligand  $\pi \rightarrow \pi^*$  electronic transitions with greater molar absorptivities.

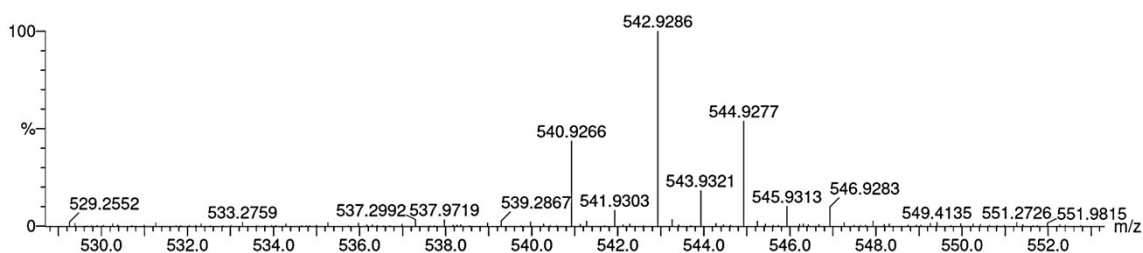


Figure S5. HRMS spectrum of **Re<sub>2</sub>CIPhen** verifying the presence of the bromine dissociated  $[\text{Na}+\text{M}-\text{Br}]^+$  sodium-adduct ion signal with an observed  $m/z$  ratio of 540.9266 against a calculated  $m/z$  ratio of 540.9261 ( $\Delta$  0.5 ppm) for the  $^{185}\text{Re}$  isotope (37.4% abundance). The accompanying MS signal for the more abundant  $^{187}\text{Re}$  isotope (62.6 %) is also observed at  $m/z$  542.9286.

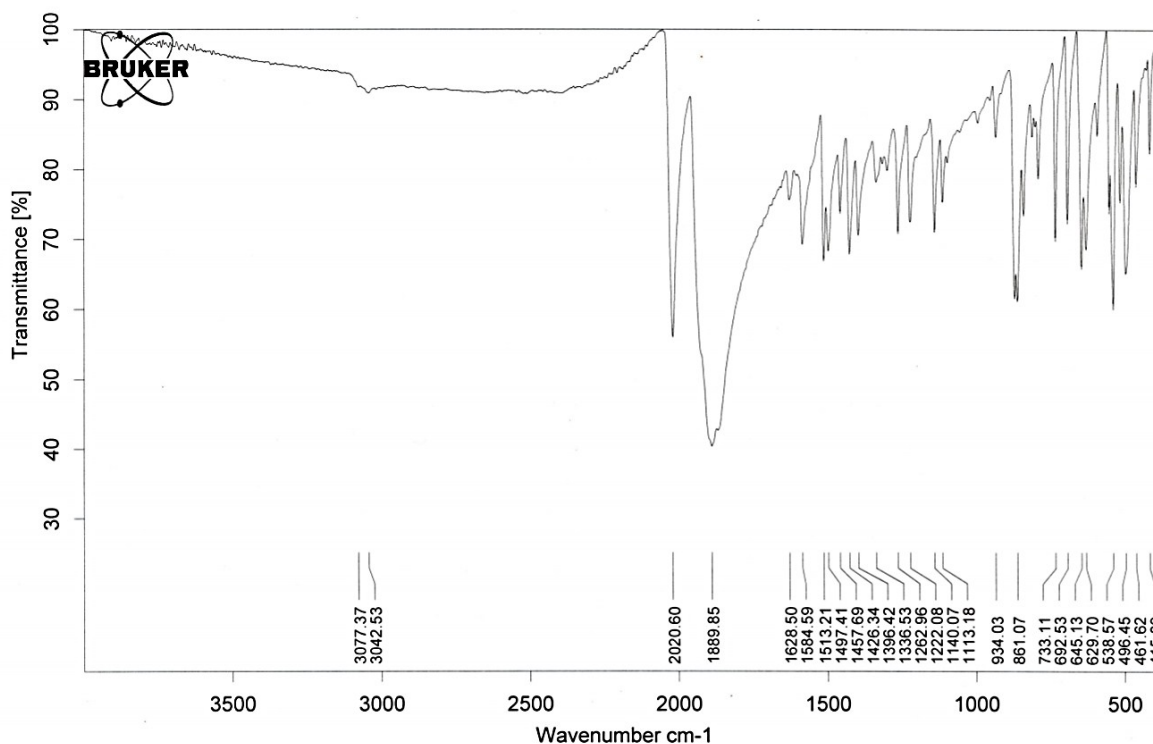


Figure S6. FTIR spectrum of **Re<sub>2</sub>FPhen** exhibiting the two distinctive  $\text{C}\equiv\text{O}$  stretching IR absorption bands at  $2021\text{ cm}^{-1}$  and  $1890\text{ cm}^{-1}$  with  $A'(1)$  and  $A'(2) \& A''$  coupled irreducible representations respectively. Weak  $\text{sp}^2$  hybridised  $\text{C}-\text{H}$  bond stretches are also observed at  $3077\text{ cm}^{-1}$  and  $3043\text{ cm}^{-1}$  from the complexed phenanthroline ligand.

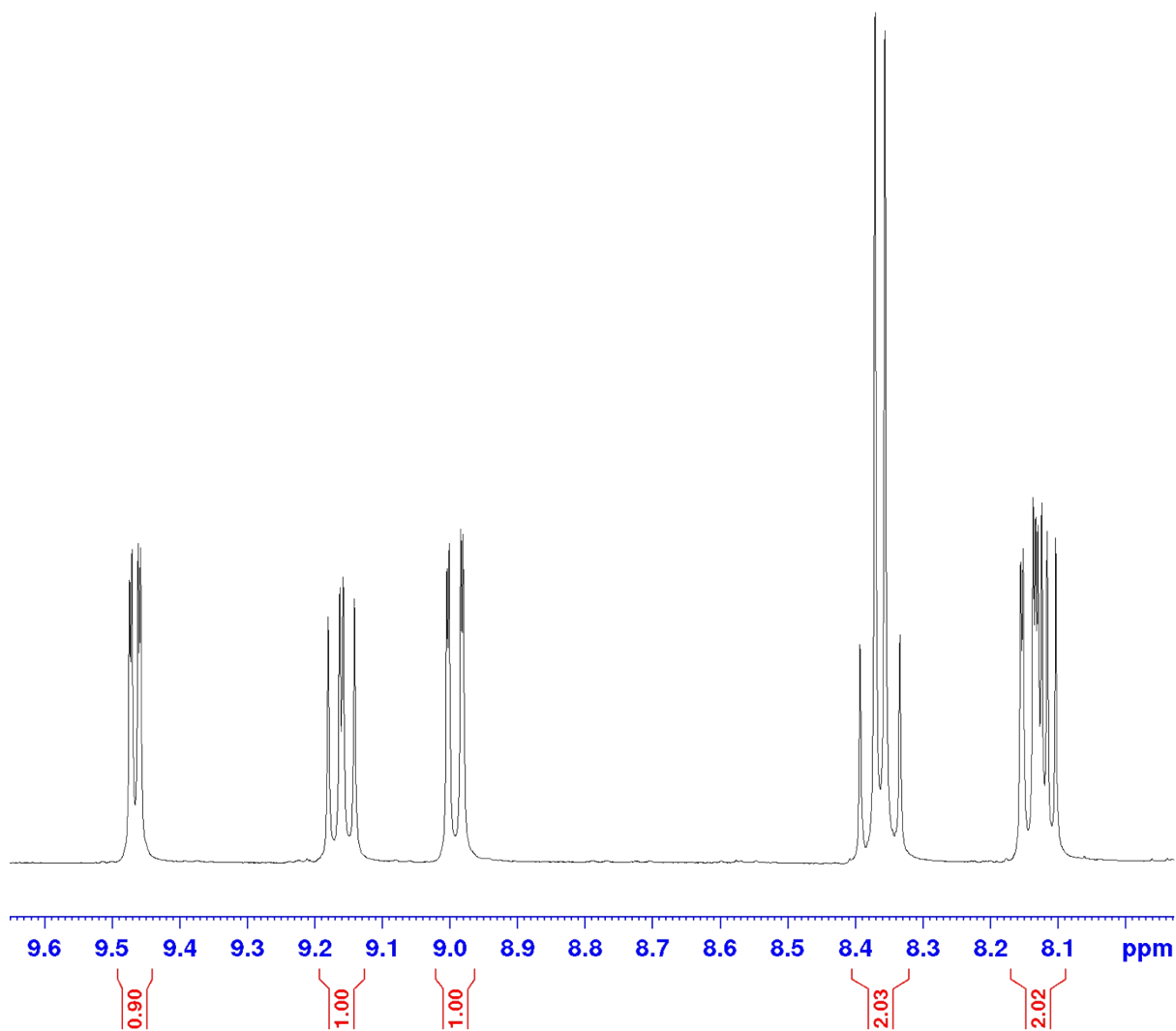


Figure S7.  $^1\text{H}$ -NMR spectrum of **Re<sub>2</sub>FPhen** showing the expected integration for seven protons in the aromatic region in DMSO- $d_6$  solution. The splitting patterns are slightly more complicated due to the additional spin-spin coupling between the hydrogen protons and NMR active fluorine-19 nucleus.

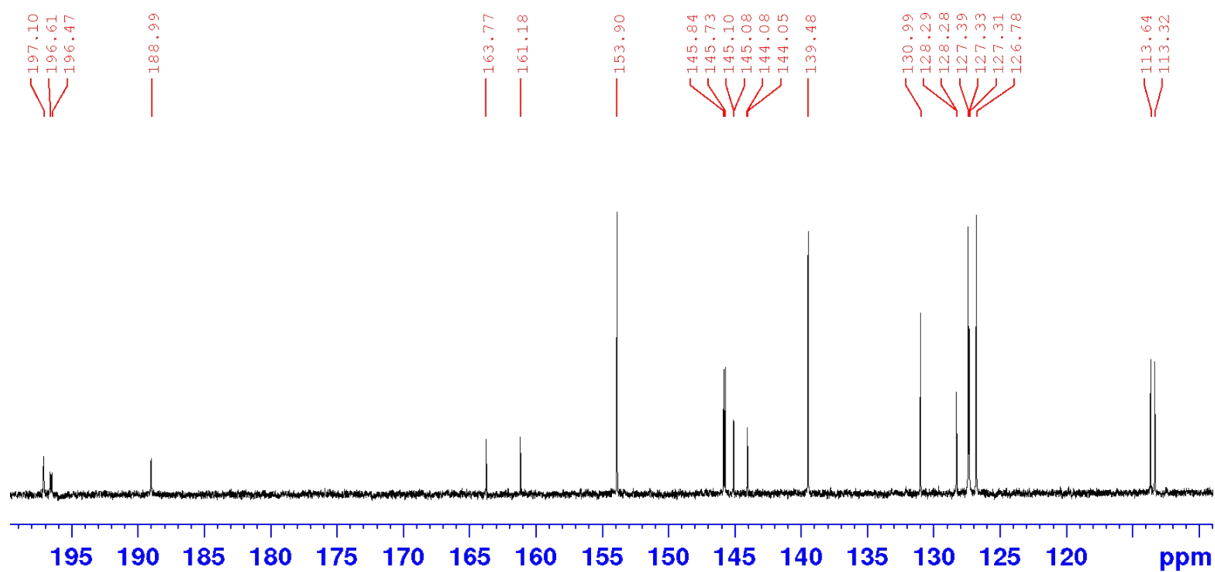


Figure S8. Complex splitting patterns observed in the  $^{13}\text{C}$ -NMR spectrum of **Re2FPhen** in  $\text{DMSO-d}_6$  due to coupling with the fluorine-19 nucleus.

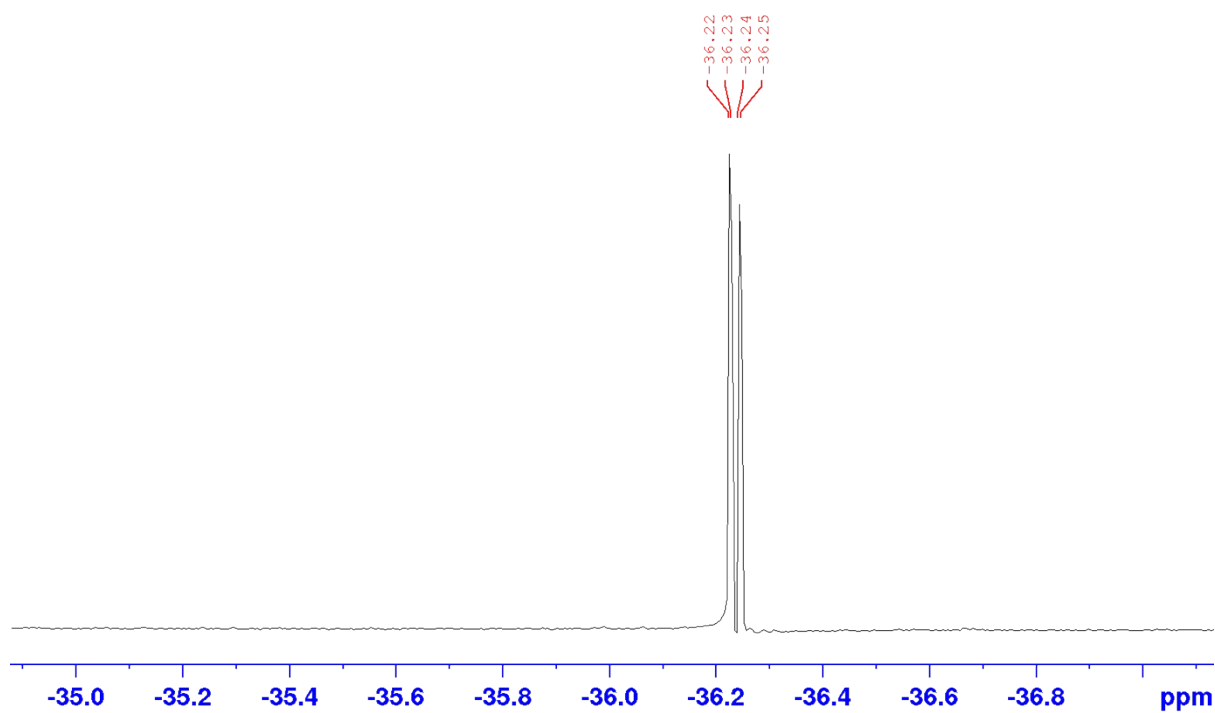


Figure S9. Coupling observed in the  $^{19}\text{F}$ -NMR spectrum of **Re2FPhen** in  $\text{DMSO-d}_6$  leads to a quartet-like splitting pattern.

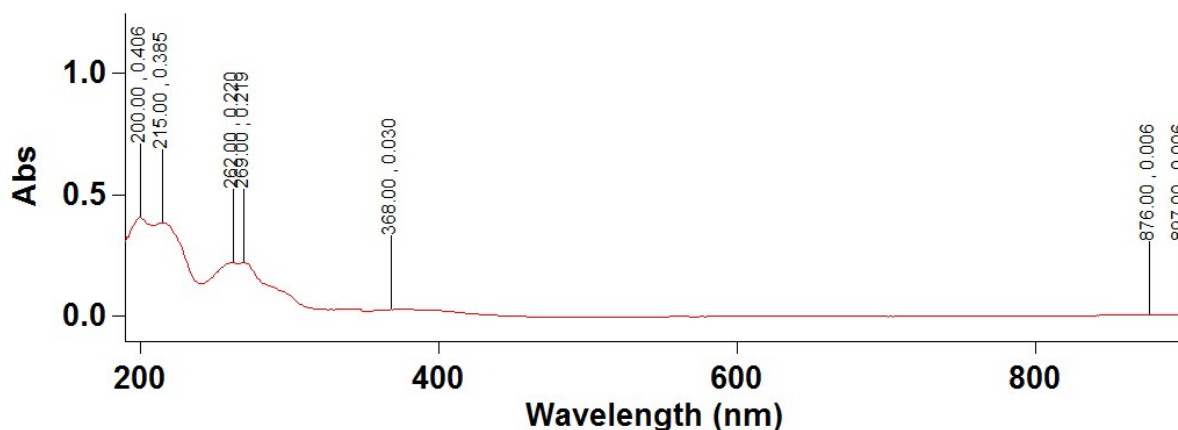


Figure S10. UV-Vis spectrum of **Re2FPhen** exhibiting the typical  $d\pi \rightarrow \pi^*$  transition to the MLCT excited state at 368 nm. Higher energy transitions at the lower wavelengths correspond to the intraligand  $\pi \rightarrow \pi^*$  electronic transitions with greater molar absorptivities.

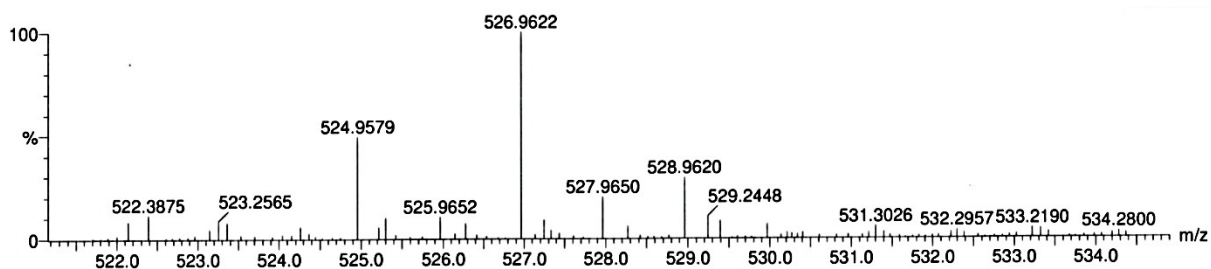


Figure S11. HRMS spectrum of **Re2FPhen** verifying the presence of the chlorine dissociated  $[\text{Na}+\text{M}-\text{Cl}]^+$  sodium-adduct ion signal with an observed  $m/z$  ratio of 524.9579 against a calculated  $m/z$  ratio of 524.9557 ( $\Delta$  2.2 ppm) for the  $^{185}\text{Re}$  isotope (37.4% abundance). The accompanying MS signal for the more abundant  $^{187}\text{Re}$  isotope (62.6%) is also observed at  $m/z$  526.9622.

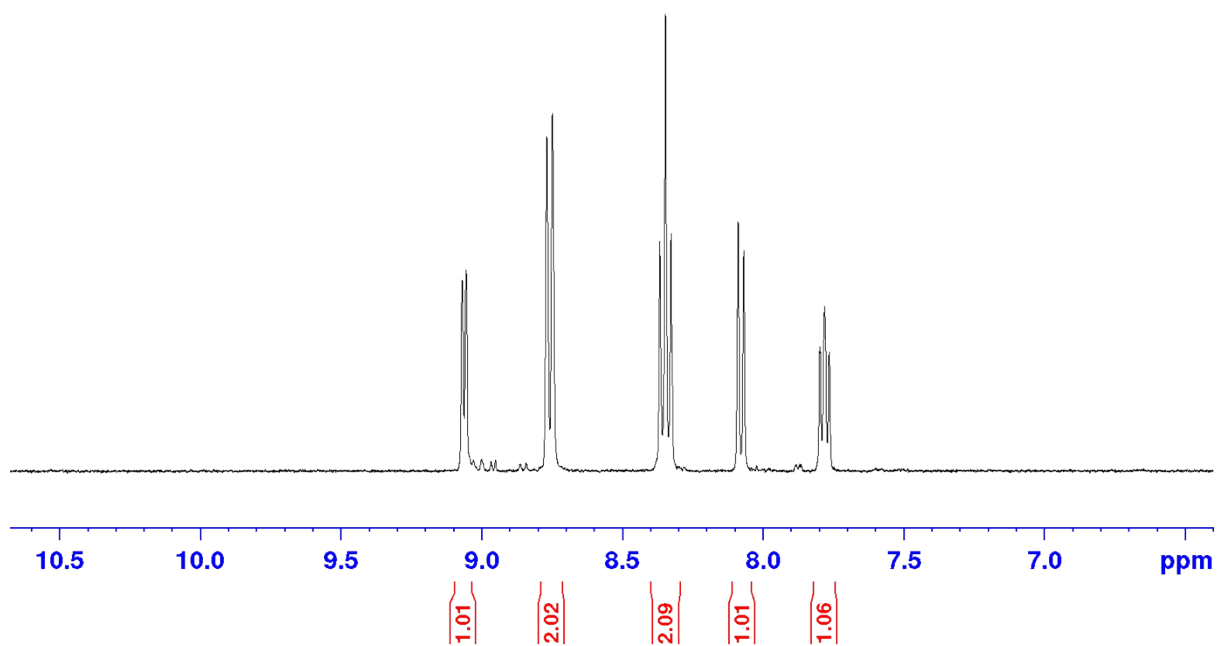


Figure S12. <sup>1</sup>H-NMR spectrum of **Re6ClBiPy** in DMSO-d<sub>6</sub>, showing the expected peak area integration for the seven protons in the aromatic region which were shifted downfield with respect to the ligand.

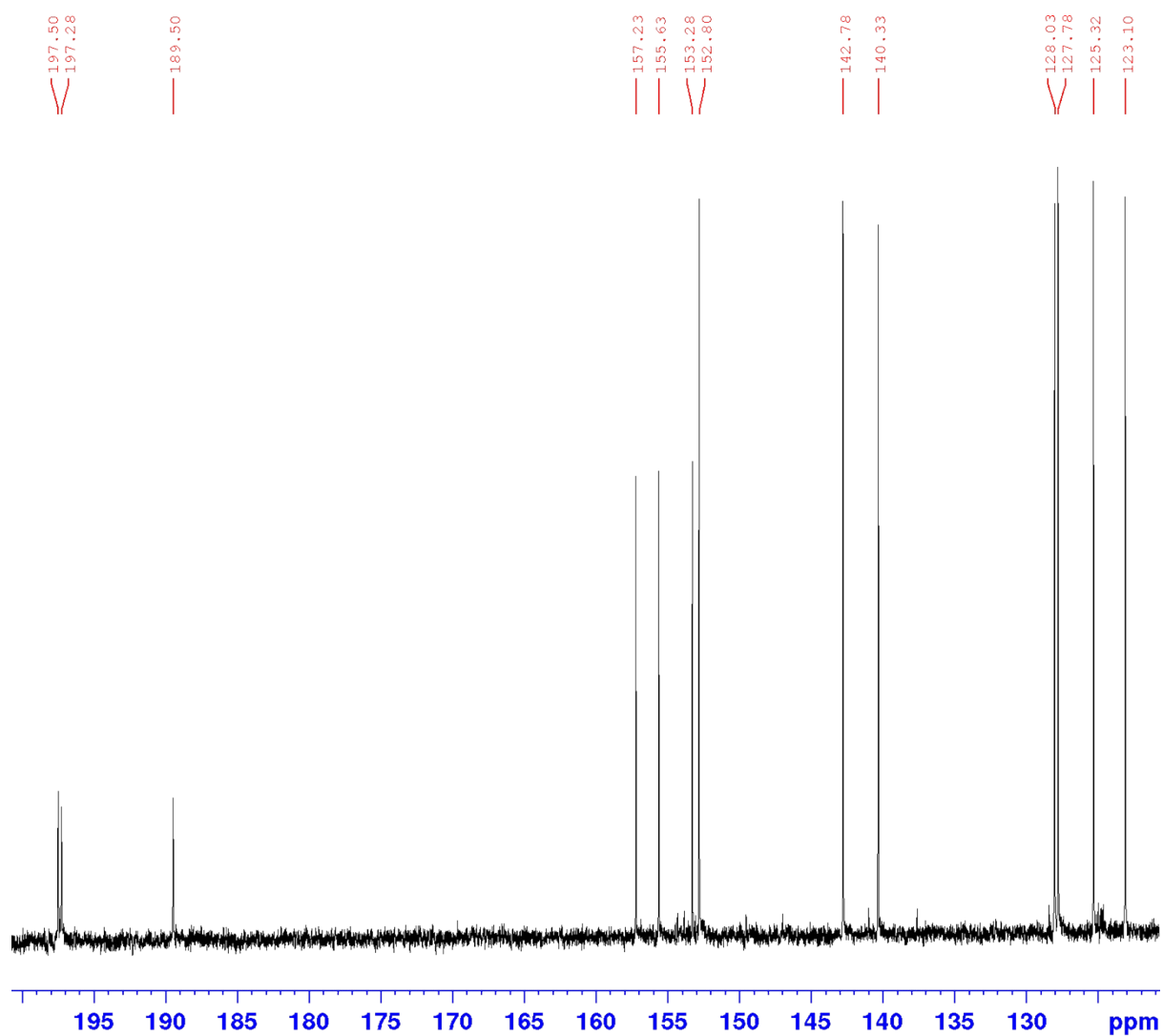


Figure S13.  $^{13}\text{C}$ -NMR spectrum of **Re6ClBiPy** in  $\text{DMSO-d}_6$ , exhibiting not only the ten aromatic carbon-13 signals from the bipyridine system though also showing the three downfield shifted carbonyl signals of the rhenium complex (189.5, 197.3 & 197.5 ppm).

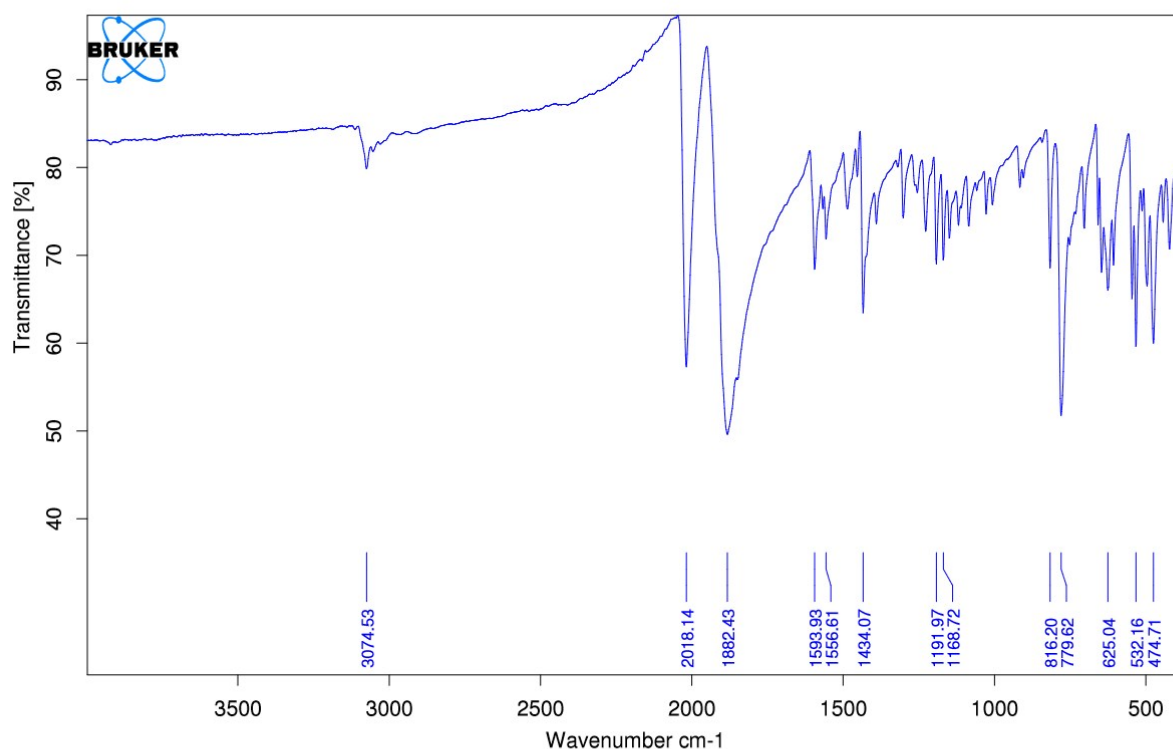


Figure S14. FTIR spectrum of **Re6ClBiPy** exhibiting the distinctive A'(1) C≡O stretching IR absorption band at 2018 cm<sup>-1</sup> and the overlapping A'(2) & A'' C≡O stretching band at 1882 cm<sup>-1</sup>. A weak sp<sup>2</sup> hybridised C–H bond stretch is also observed at 3075 cm<sup>-1</sup> from the bipyridine ligand.

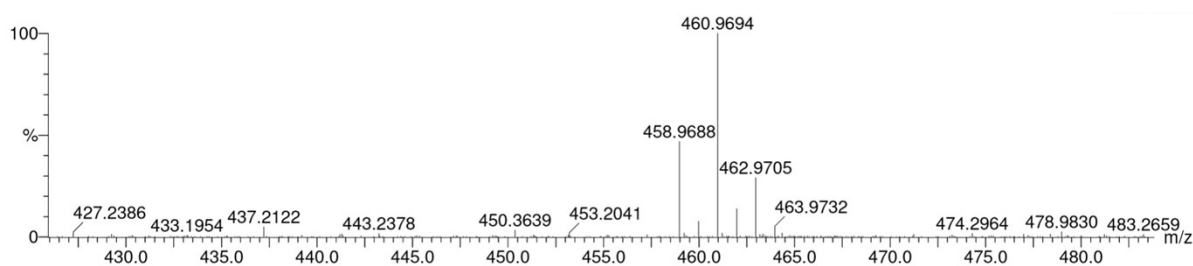


Figure S15. HRMS spectrum of **Re6ClBiPy** depicting the chlorine-dissociated [M-Cl]<sup>+</sup> ion signal observable at  $m/z$  460.9694 with a calculated ratio of  $m/z$  460.9703 ( $\Delta$  - 0.9 ppm) for the complex incorporating the <sup>187</sup>Re isotope in 62.6% natural abundance. An additional signal with  $m/z$  458.9688 is also observed for the same ion incorporating the <sup>185</sup>Re isotope in 37.4% natural abundance.

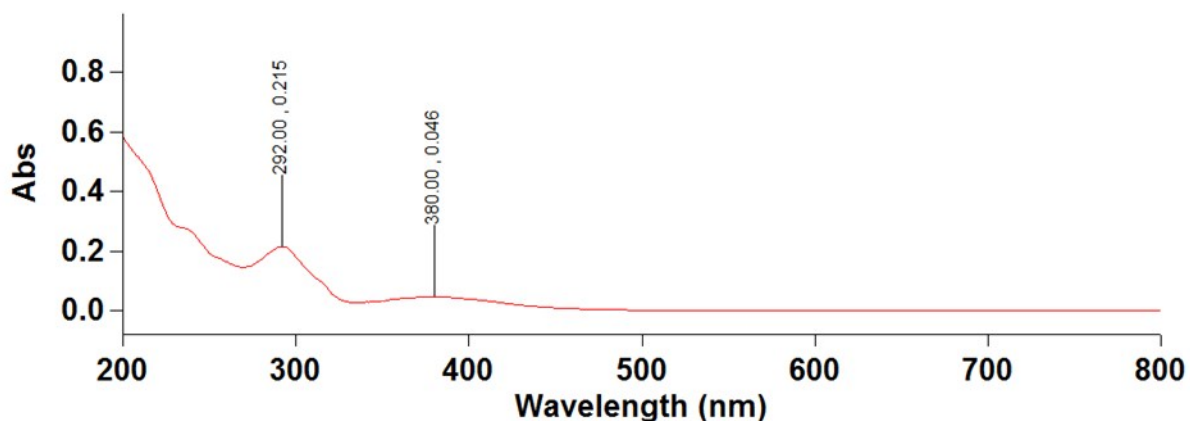


Figure S16. UV-Vis spectrum of **Re6ClBiPy** ( $2 \mu\text{g}\cdot\text{mL}^{-1}$  in acetonitrile) showing the absorption band for the  $d\pi \rightarrow \pi^*$  electronic transition to the MLCT excited state at 380 nm, alongside higher energy  $\pi \rightarrow \pi^*$  transitions to LC excited states with greater molar absorptivities.

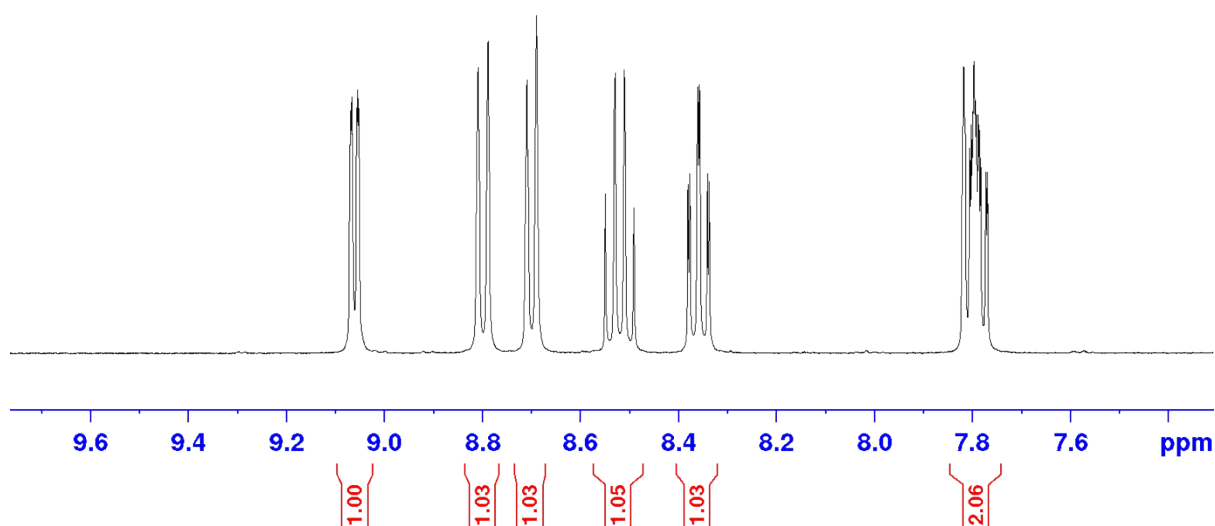


Figure S17.  $^1\text{H}$ -NMR spectrum of **Re6FBiPy** in  $\text{DMSO-d}_6$ , showing the expected peak area integration for the seven protons in the aromatic region which were shifted downfield with respect to the ligand. The peaks exhibit more complex splitting patterns on account of the coupling between the fluorine-19 isotope present in the molecule.

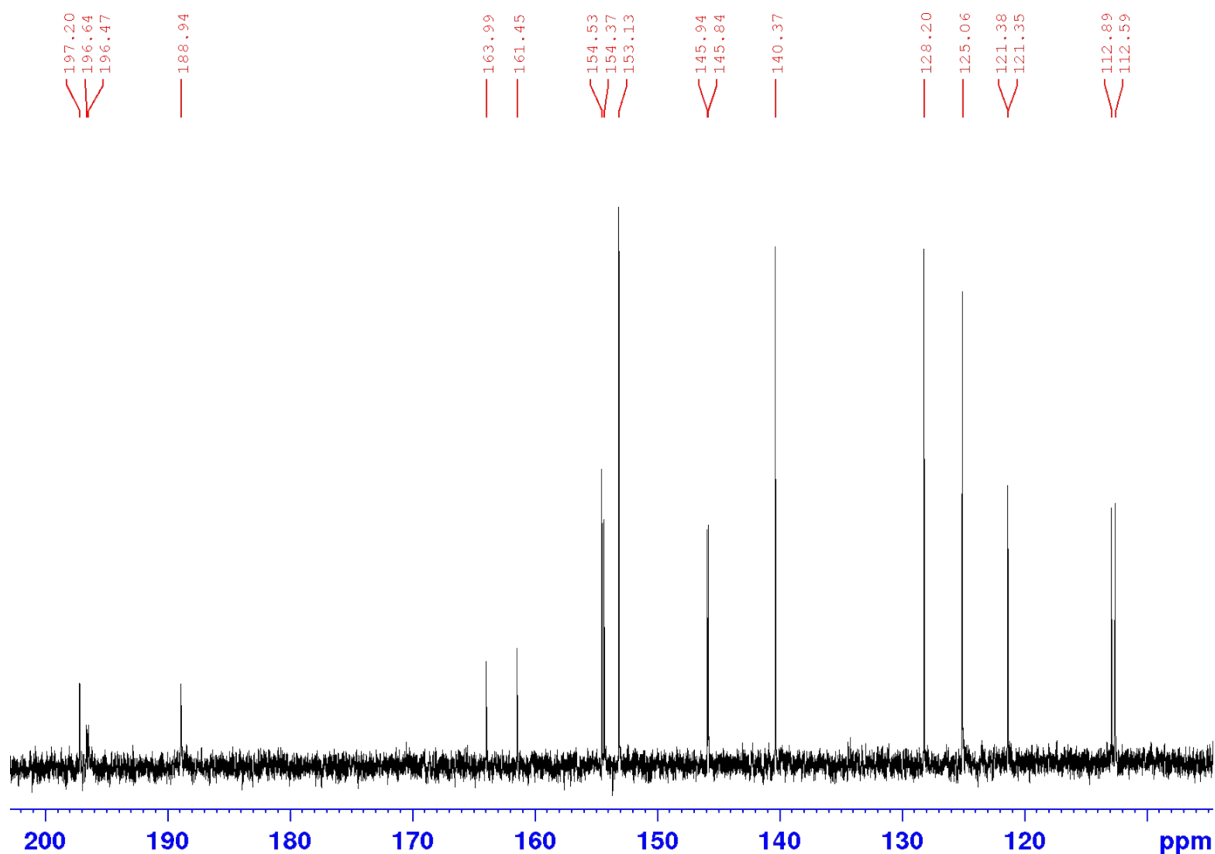


Figure S18.  $^{13}\text{C}$ -NMR spectrum of **Re6FBiPy** in  $\text{DMSO-d}_6$ , showing the downfield shifted carbonyl signals with respect to the carbon-13 aromatic signals from the bipyridine ring. Complex splitting is observed due to the coupling between the carbon-13 and fluorine-19 nuclei.

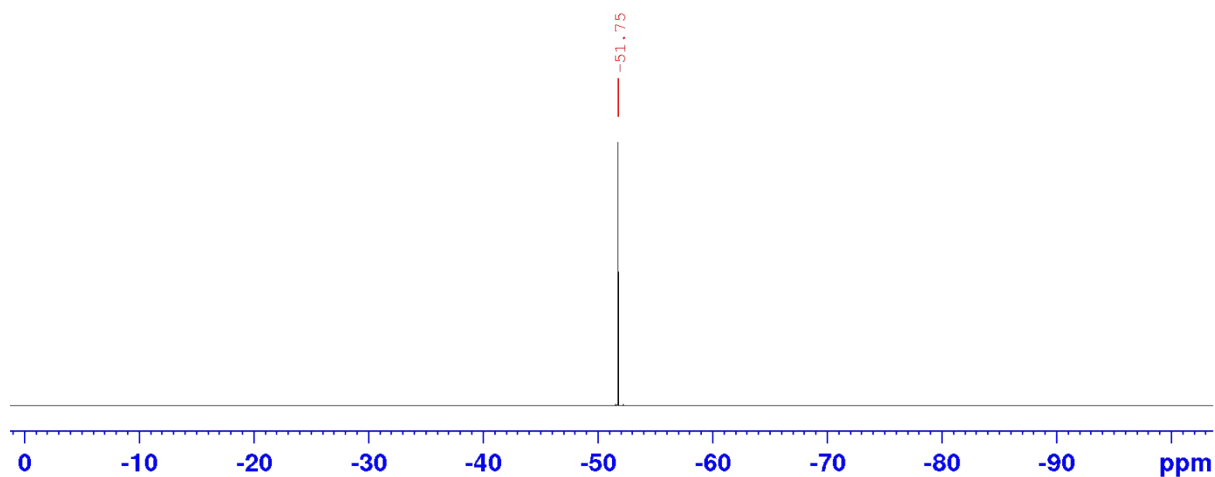


Figure S19. Decoupled  $^{19}\text{F}$ -NMR spectrum of **R62FBiPy** in  $\text{DMSO-d}_6$  displaying the signal for the sole fluorine-19 nucleus in the molecule at -50.75 ppm.

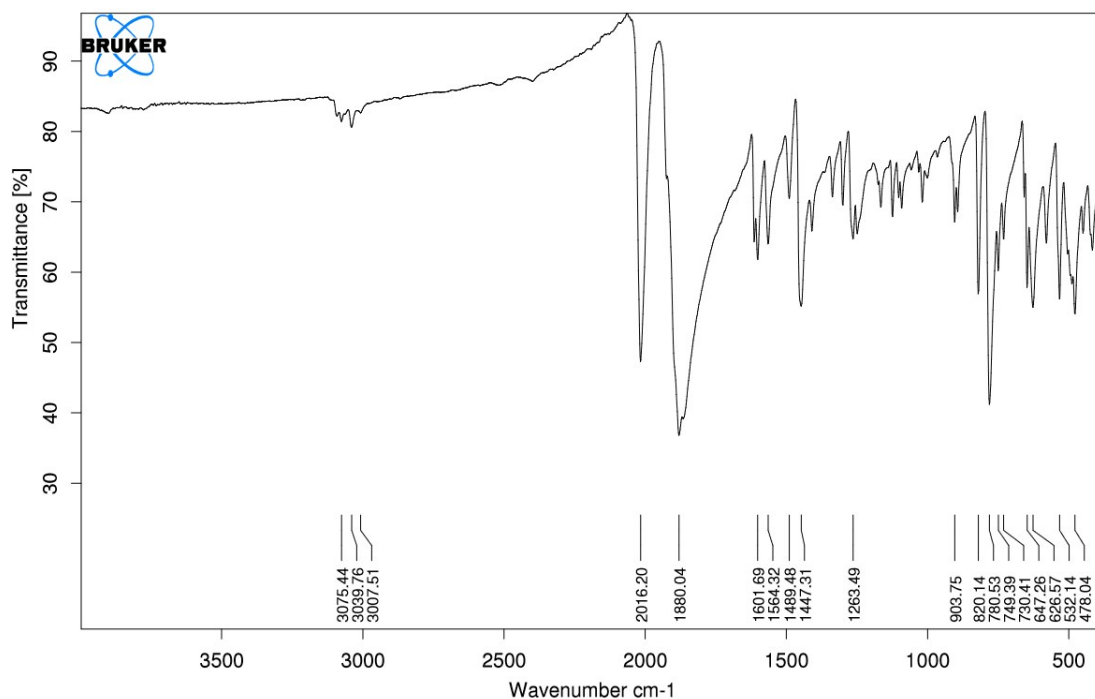


Figure S20. FTIR spectrum of **Re6FBiPy** exhibiting the distinctive A'(1) C≡O stretching IR absorption band at 2016 cm<sup>-1</sup> and the overlapping A'(2) & A'' C≡O stretching band at 1880 cm<sup>-1</sup>. Weak sp<sup>2</sup> hybridised C–H bond stretches are also observed at higher wavenumbers (*circa* 3039 cm<sup>-1</sup>) from the bipyridine ligand.

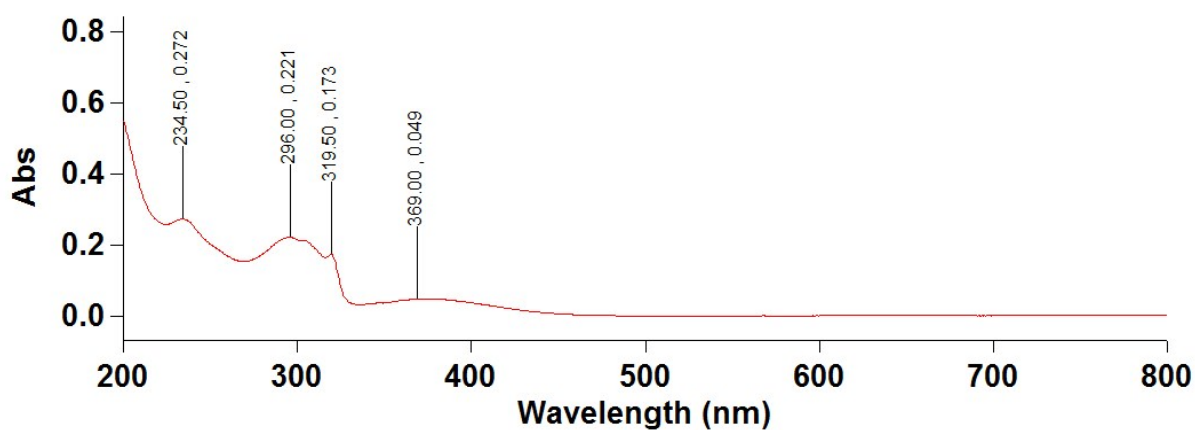


Figure S21. UV-Vis spectrum of **Re6FBiPy** (2 μg.mL<sup>-1</sup> in acetonitrile) showing the absorption band for the dπ → π\* electronic transition to the MLCT excited state at 369 nm, alongside higher energy π → π\* transitions to LC excited states with greater molar absorptivities.

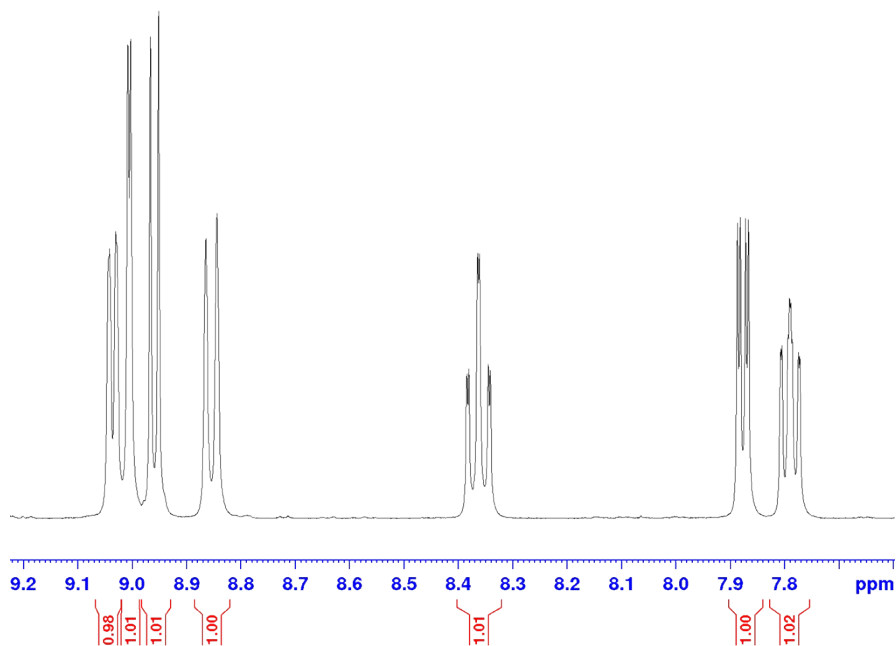


Figure S22.  $^1\text{H-NMR}$  spectrum of  $\text{Re}_4\text{CIBiPy}$  in  $\text{DMSO-d}_6$ , showing the expected peak area integration for the seven protons in the aromatic region which were shifted downfield with respect to the ligand.

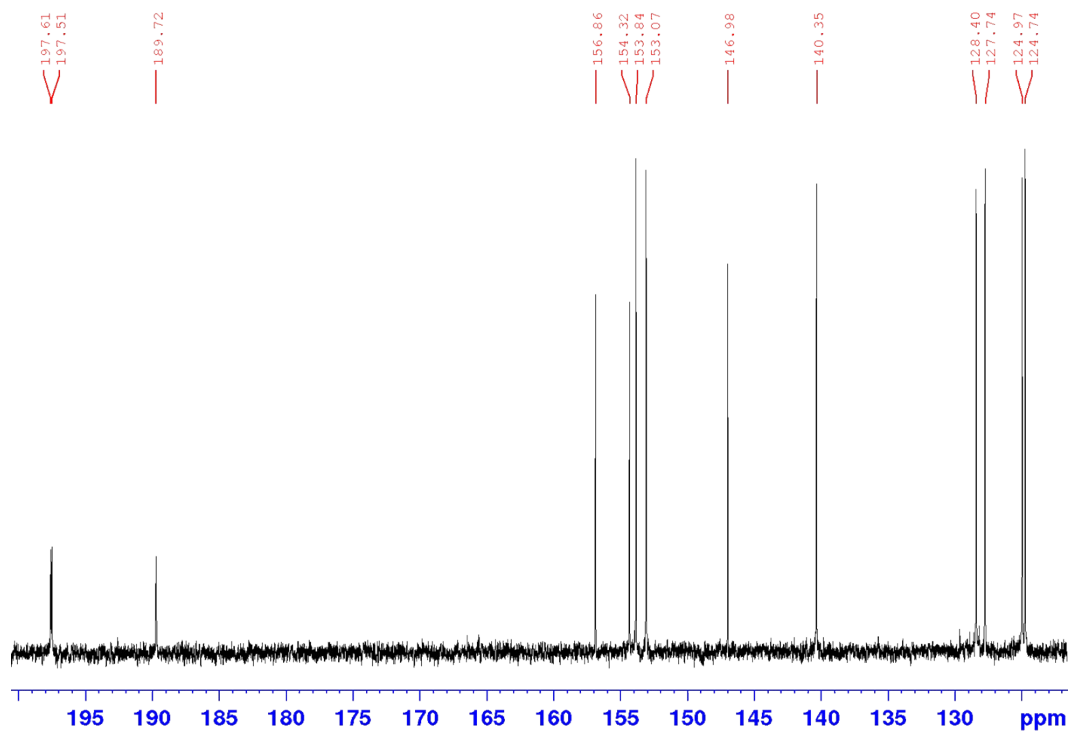


Figure S23.  $^{13}\text{C-NMR}$  spectrum of  $\text{Re}_4\text{CIBiPy}$  in  $\text{DMSO-d}_6$ , showing the three downfield shifted carbonyl signals with respect to the carbon-13 aromatic signals from the bipyridine ring.

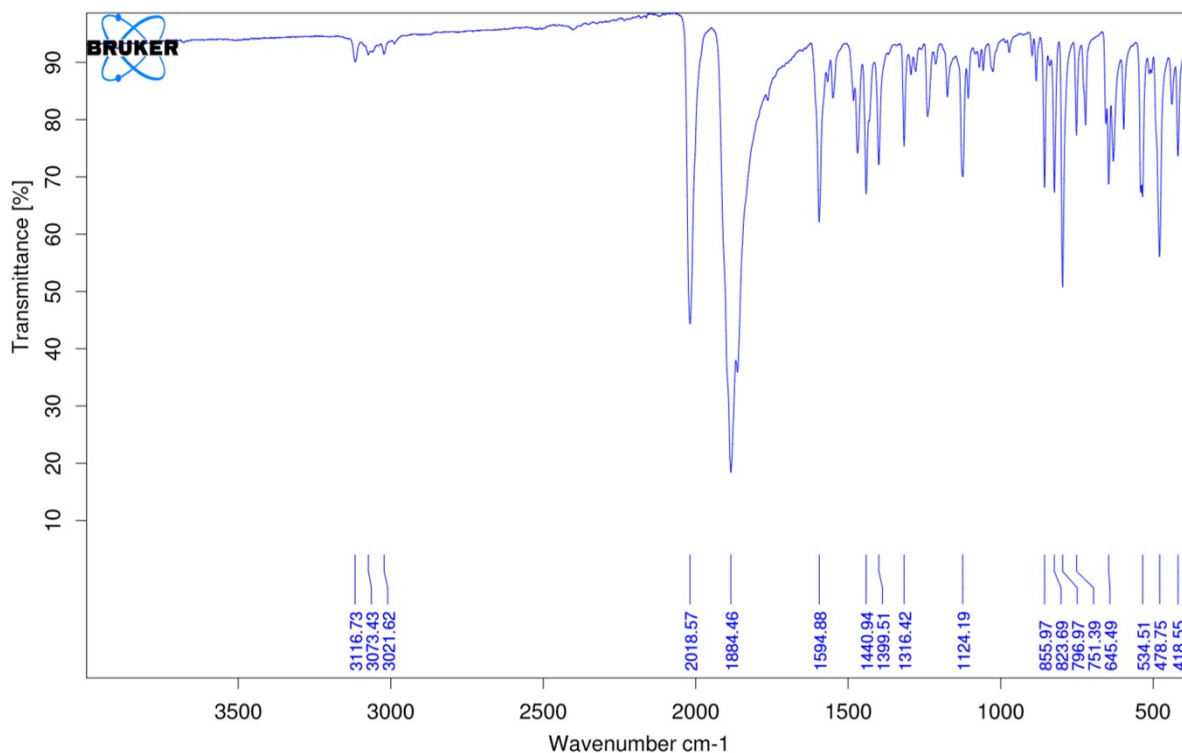


Figure S24. FTIR spectrum of **Re<sub>4</sub>ClBiPy** exhibiting the distinctive A'(1) C≡O stretching IR absorption band at 2019 cm<sup>-1</sup> and the overlapping A'(2) & A'' C≡O stretching band at 1884 cm<sup>-1</sup>. Weak sp<sup>2</sup> hybridised C–H bond stretches are also observed at higher wavenumbers (*circa* 3073 cm<sup>-1</sup>) from the bipyridine ligand.

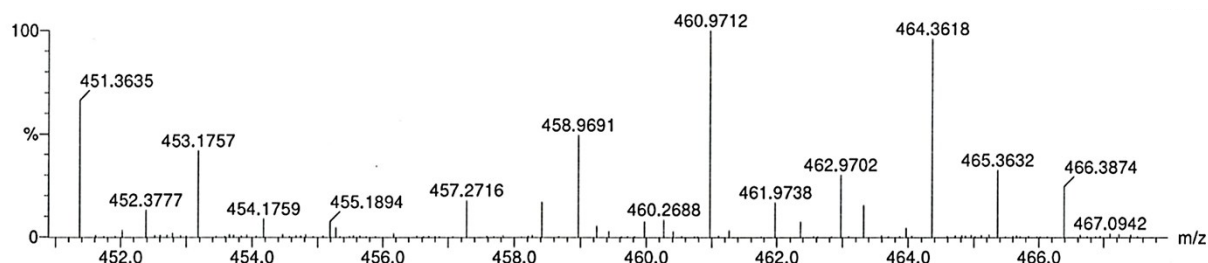


Figure S25. HRMS spectrum of **Re<sub>4</sub>ClBiPy** depicting the chlorine-dissociated [M-Cl]<sup>+</sup> ion signal observable at  $m/z$  460.9712 with a calculated ratio of  $m/z$  460.9703 ( $\Delta$  0.9 ppm) for the complex incorporating the <sup>187</sup>Re isotope in 62.6% natural abundance. An additional signal with  $m/z$  458.9691 is also observed for the same ion incorporating the <sup>185</sup>Re isotope in 37.4% natural abundance.

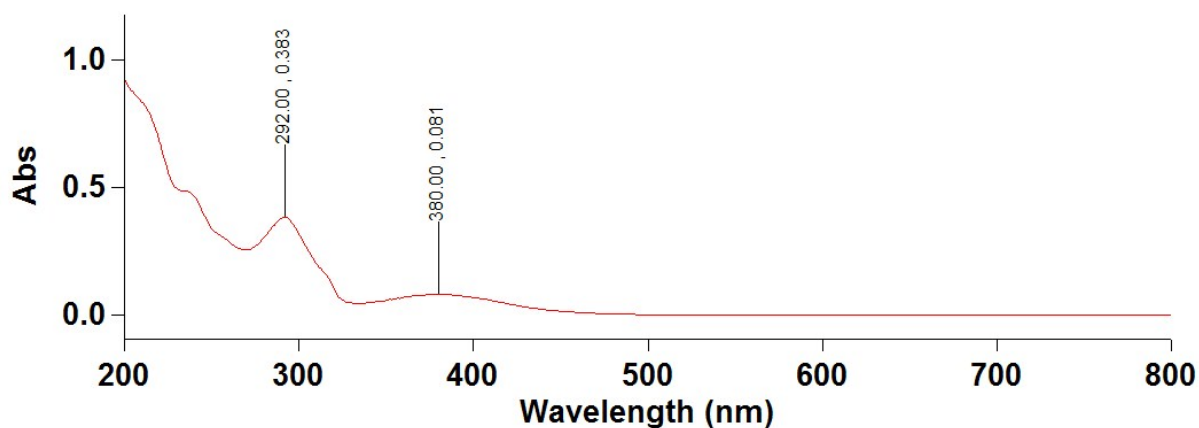


Figure S26. UV-Vis spectrum of **Re4CIBiPy** ( $5 \mu\text{g}\cdot\text{mL}^{-1}$  in acetonitrile) showing the absorption band for the  $d\pi \rightarrow \pi^*$  electronic transition to the MLCT excited state at 369 nm, alongside higher energy  $\pi \rightarrow \pi^*$  transitions to LC excited states with greater molar absorptivities.

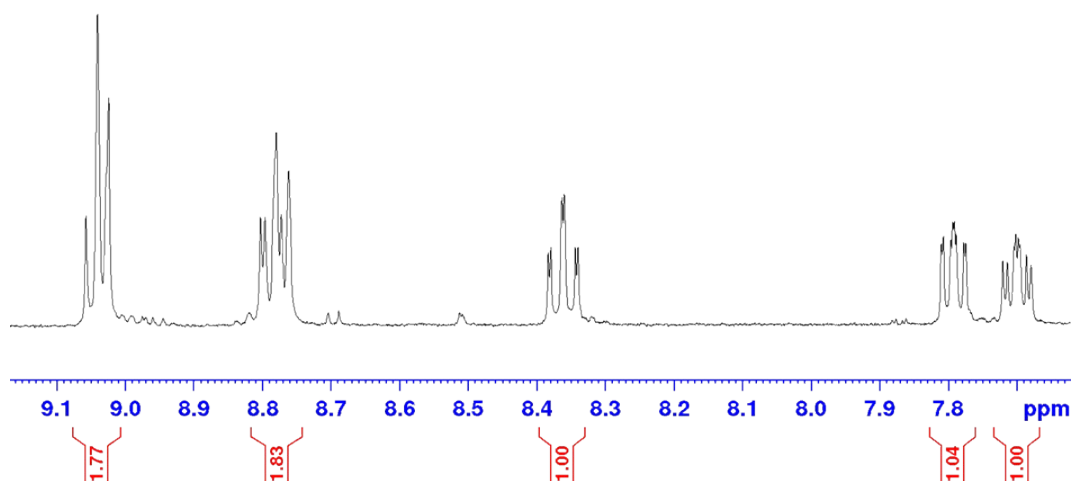


Figure S27.  $^1\text{H}$ -NMR spectrum of **Re4FBiPy** in  $\text{DMSO-d}_6$ , showing the expected peak area integration for the seven protons in the aromatic region which were shifted downfield with respect to the ligand. The peaks exhibit more complex splitting patterns on account of the coupling between the fluorine-19 isotope present in the molecule.

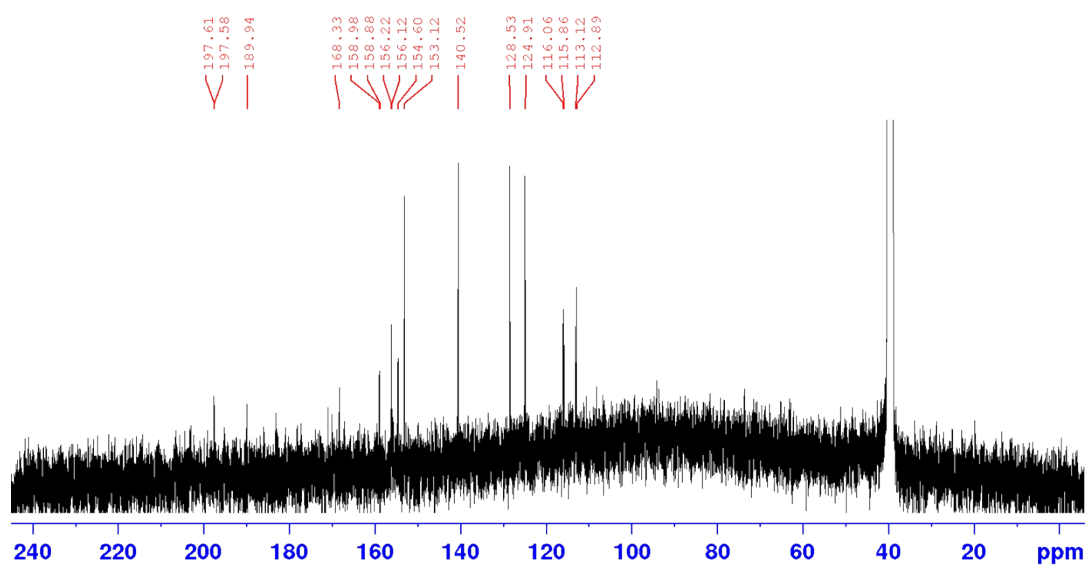


Figure S28.  $^{13}\text{C}$ -NMR spectrum of **Re4FBiPy** in  $\text{DMSO-d}_6$ , showing the downfield shifted carbonyl signals with respect to the carbon-13 aromatic signals from the bipyridine ring. Complex splitting is observed due to the coupling between the carbon-13 and fluorine-19 nuclei.

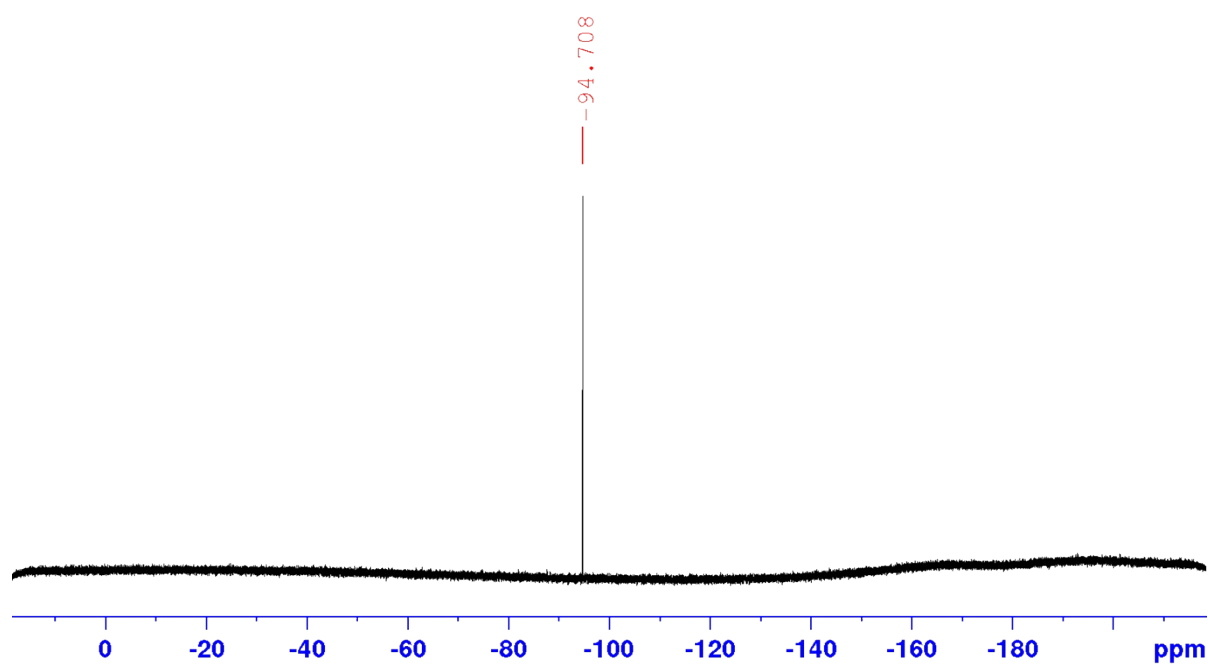


Figure S29. CPD  $^{19}\text{F}$ -NMR spectrum of **Re4FBiPy** in  $\text{DMSO-d}_6$  displaying the signal for the sole fluorine-19 nucleus in the molecule at -94.71 ppm.

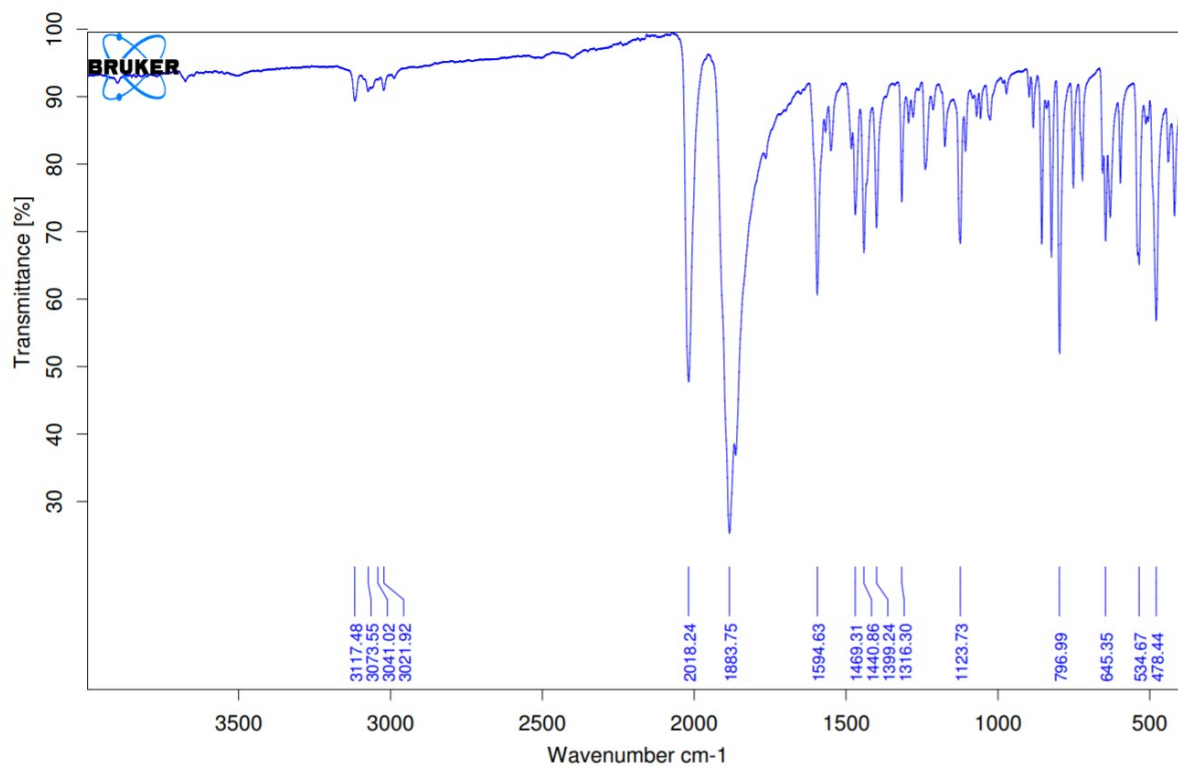


Figure S30. FTIR spectrum of **Re<sub>4</sub>FBiPy** exhibiting the distinctive A'(1) C≡O stretching IR absorption band at 2018 cm<sup>-1</sup> and the overlapping A'(2) & A'' C≡O stretching band at 1884 cm<sup>-1</sup>. Weak sp<sup>2</sup> hybridised C–H bond stretches are also observed at higher wavenumbers (*circa* 3041 cm<sup>-1</sup>) from the bipyridine ligand.

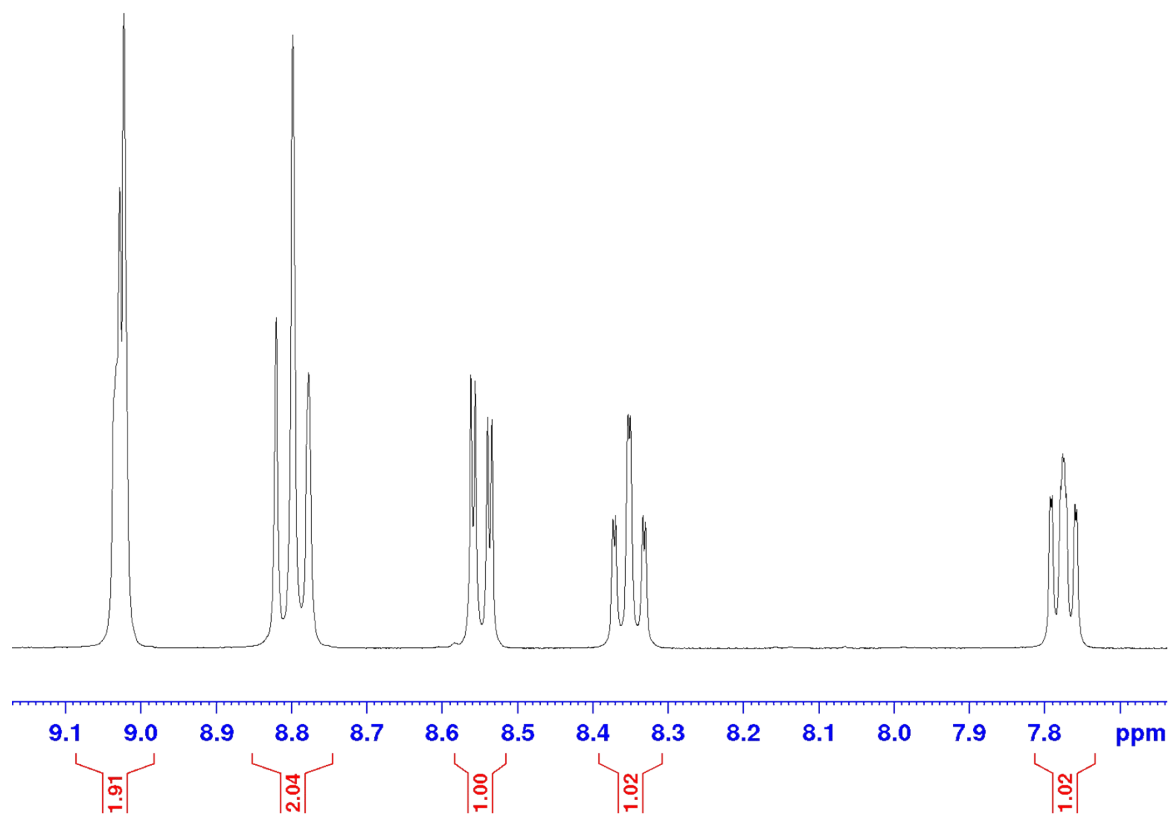


Figure S31.  $^1\text{H}$ -NMR spectrum of **Re5CIBiPy** in  $\text{DMSO-d}_6$ , showing the expected peak area integration for the seven protons in the aromatic region which were shifted downfield with respect to the ligand.

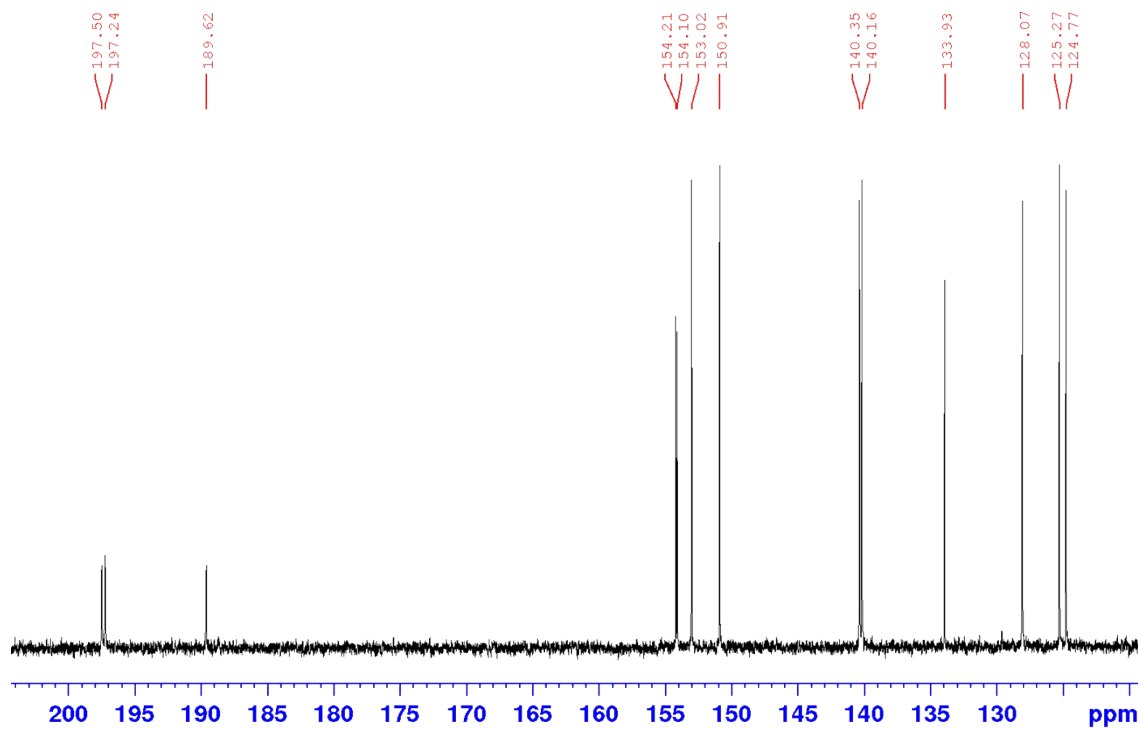


Figure S32.  $^{13}\text{C}$ -NMR spectrum of **Re5CIBiPy** in  $\text{DMSO-d}_6$ , showing the three downfield shifted carbonyl signals with respect to the carbon-13 aromatic signals from the bipyridine ring.

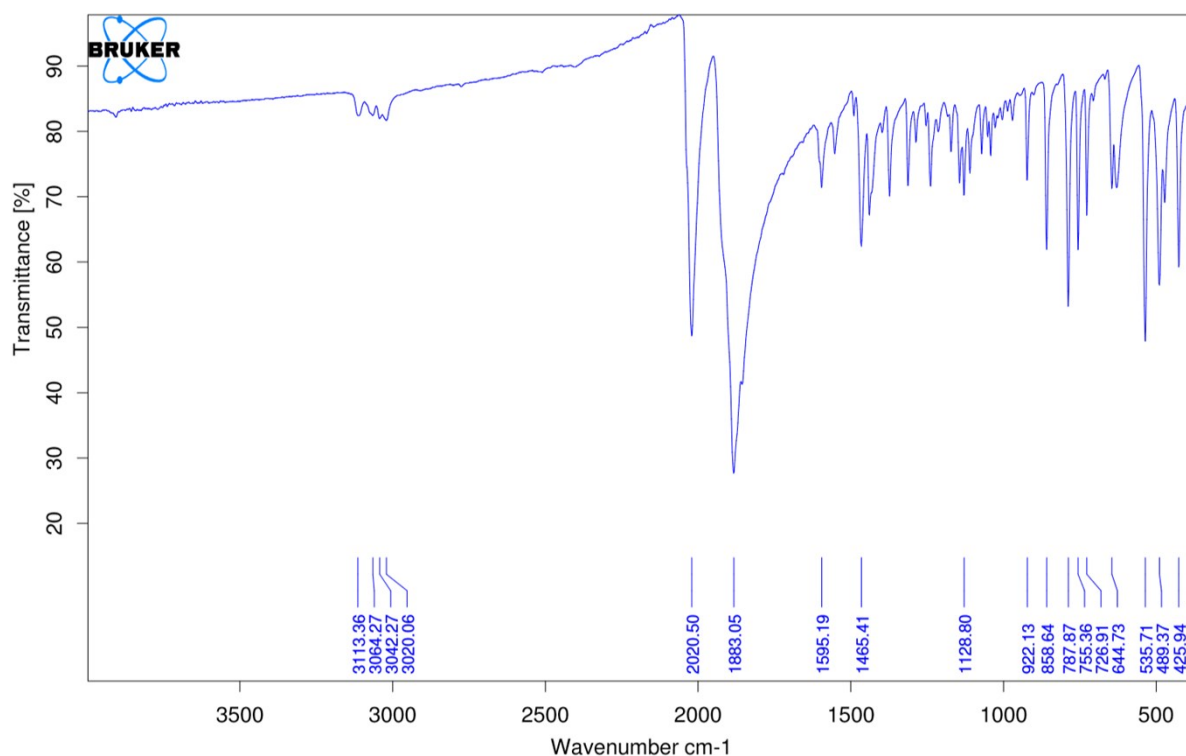


Figure S33. FTIR spectrum of **Re5ClBiPy** exhibiting the distinctive A'(1) C≡O stretching IR absorption band at 2021 cm<sup>-1</sup> and the overlapping A'(2) & A'' C≡O stretching band at 1883 cm<sup>-1</sup>. Weak sp<sup>2</sup> hybridised C–H bond stretches are also observed at higher wavenumbers (*circa* 3064 cm<sup>-1</sup>) from the bipyridine ligand.

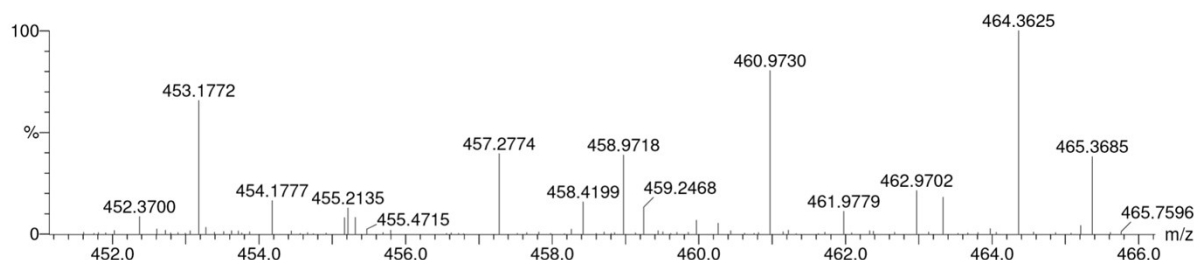


Figure S34. HRMS spectrum of **Re5ClBiPy** depicting the chlorine-dissociated [M-Cl]<sup>+</sup> ion signal observable at  $m/z$  460.9730 with a calculated ratio of  $m/z$  460.9703 ( $\Delta$  5.9 ppm) for the complex incorporating the <sup>187</sup>Re isotope in 62.6% natural abundance. An additional signal with  $m/z$  458.9718 is also observed for the same ion incorporating the <sup>185</sup>Re isotope in 37.4% natural abundance.

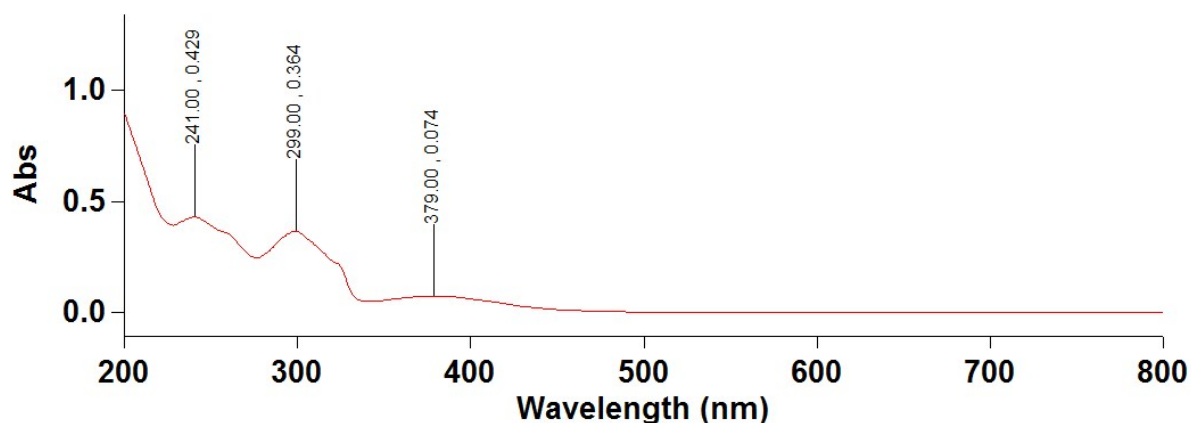


Figure S35. UV-Vis spectrum of **Re5ClBiPy** ( $5 \mu\text{g}\cdot\text{mL}^{-1}$  in acetonitrile) showing the absorption band for the  $d\pi \rightarrow \pi^*$  electronic transition to the MLCT excited state at 379 nm, alongside higher energy  $\pi \rightarrow \pi^*$  transitions to LC excited states with greater molar absorptivities.

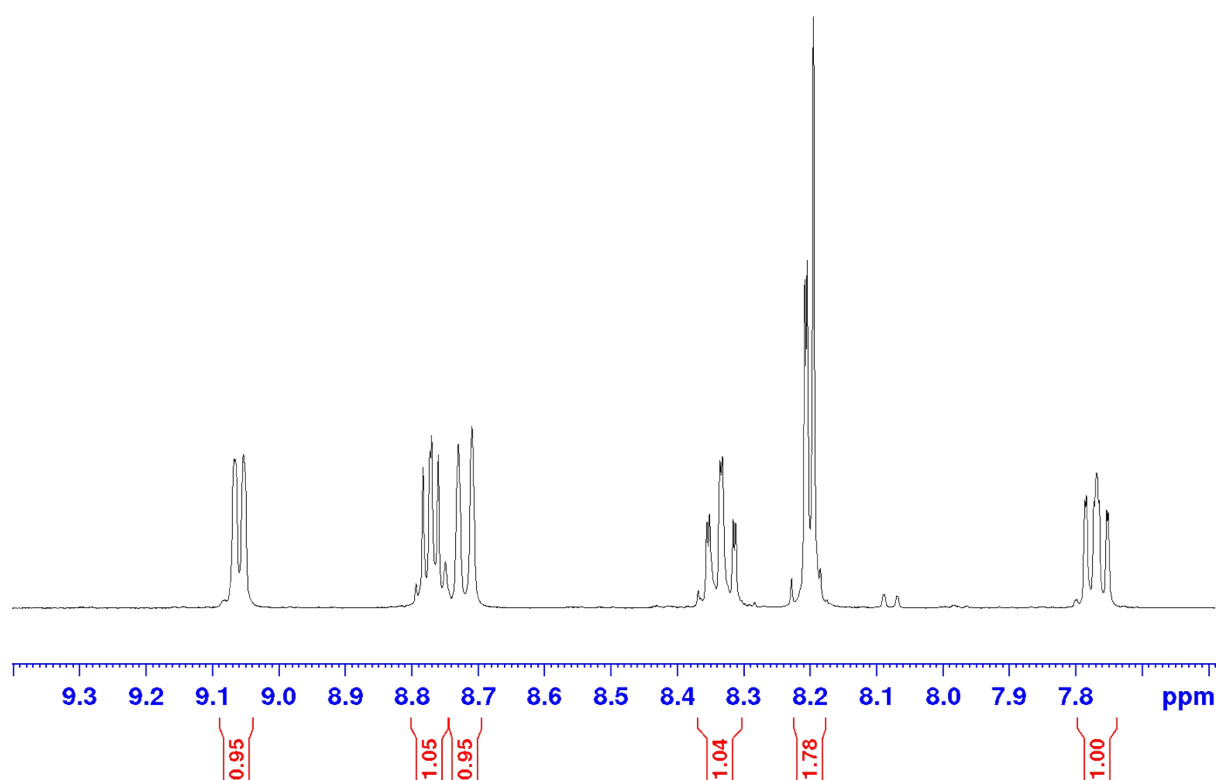


Figure S36.  $^1\text{H}$ -NMR spectrum of **Re6BrBiPy** in  $\text{DMSO-d}_6$ , showing the expected peak area integration for the seven protons in the aromatic region which were shifted downfield with respect to the ligand.

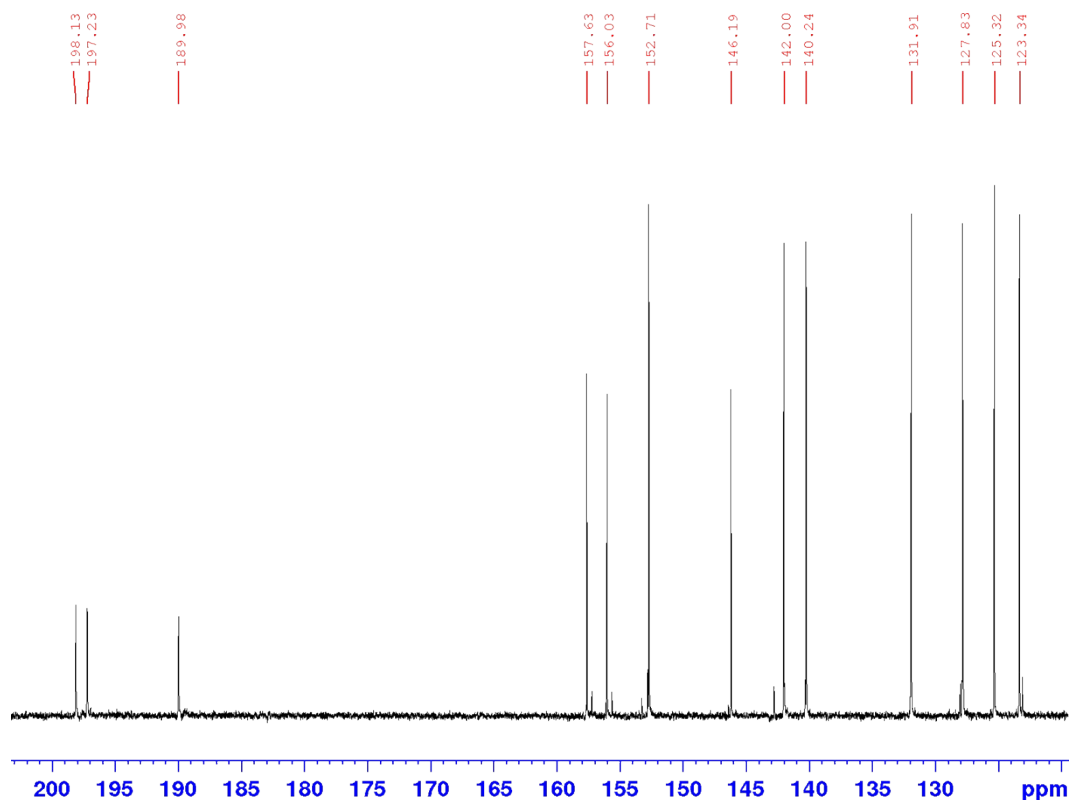


Figure S37.  $^{13}\text{C}$ -NMR spectrum of **Re6BrBiPy** in  $\text{DMSO-D}_6$ , exhibiting not only the ten aromatic carbon-13 signals from the bipyridine system though also showing the three downfield shifted carbonyl signals of the rhenium complex (190.0, 197.2 & 198.1 ppm).

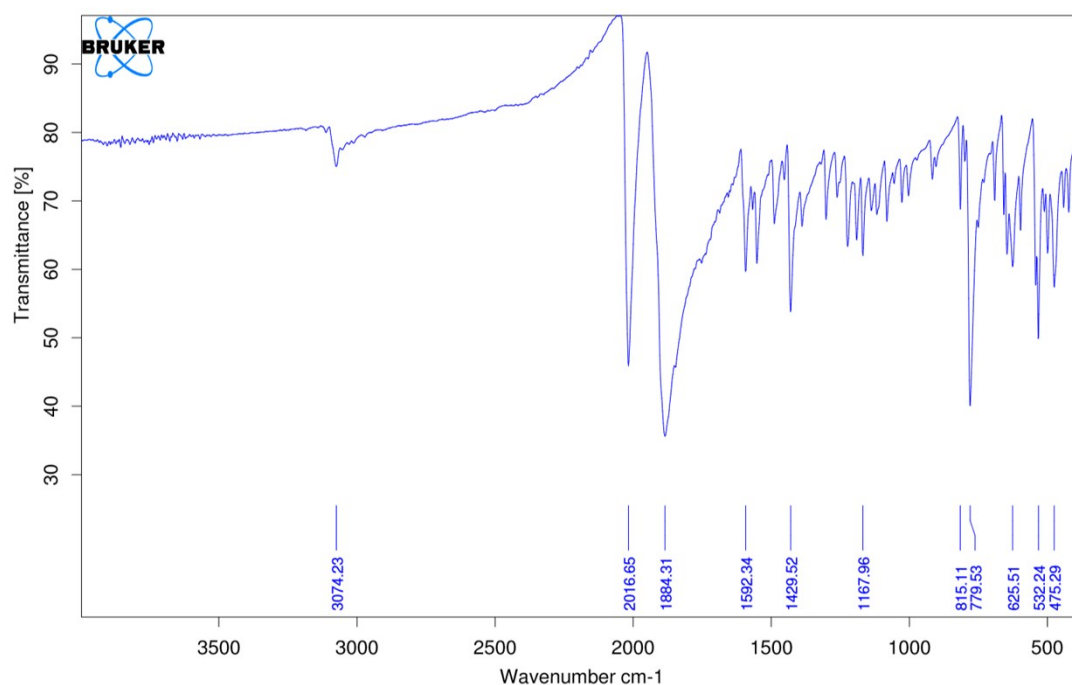


Figure S38. FTIR spectrum of **Re6BrBiPy** exhibiting the distinctive  $\text{A}'(1)$   $\text{C}\equiv\text{O}$  stretching IR absorption band at  $2017\text{ cm}^{-1}$  and the overlapping  $\text{A}'(2)$  &  $\text{A}''$   $\text{C}\equiv\text{O}$  stretching band at  $1884\text{ cm}^{-1}$ . A weak  $\text{sp}^2$  hybridised  $\text{C-H}$  bond stretch is also observed at  $3074\text{ cm}^{-1}$  from the bipyridine ligand.

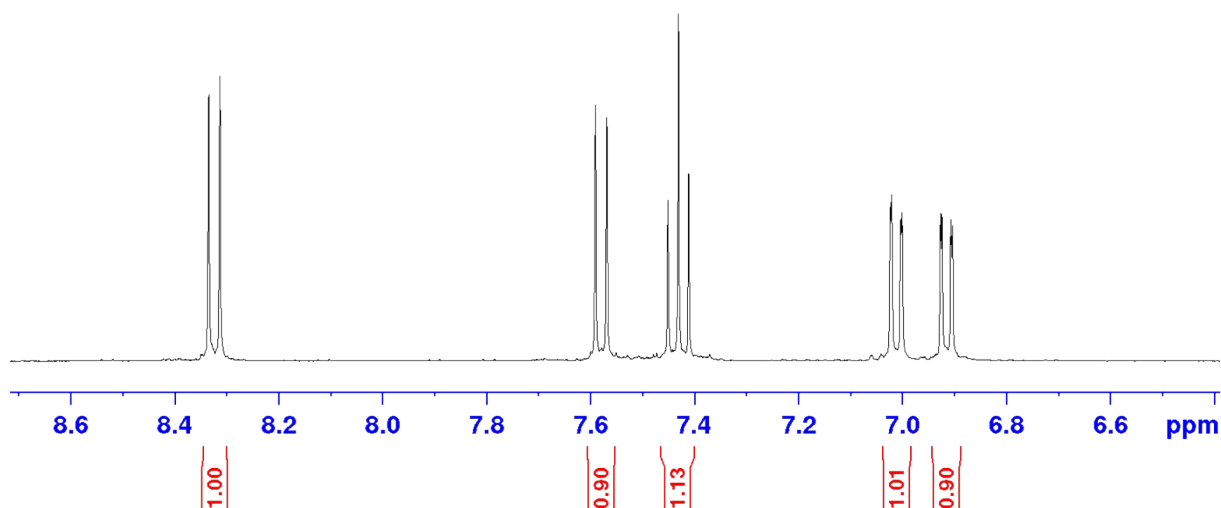


Figure S39. <sup>1</sup>H-NMR spectrum of **Re2Cl8HQ** in acetonitrile-d<sub>3</sub> showing the expected integration for five protons in the aromatic region. The resonance signal for the methyl group of the acetonitrilo ancillary ligand is masked behind the residual solvent peak.

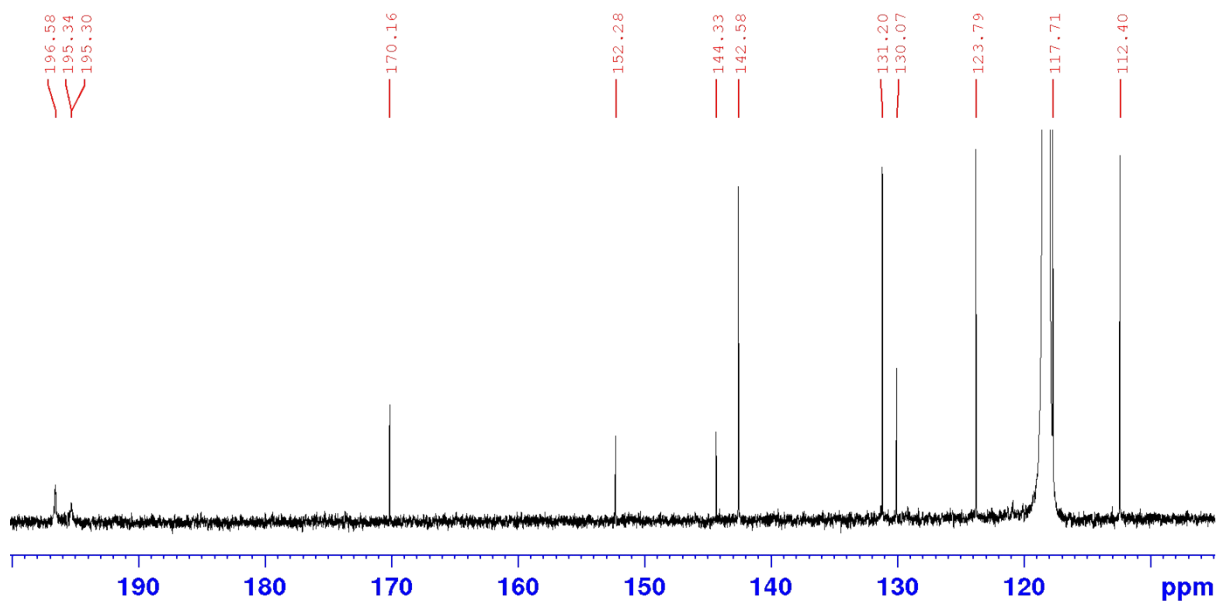


Figure S40. <sup>13</sup>C-NMR spectrum of **Re2Cl8HQ** in acetonitrile-d<sub>3</sub> showing the three downfield shifted carbon-13 resonance signals of the carbonyl ligands and the nine carbon-13 resonance signals of the quinoline ring.

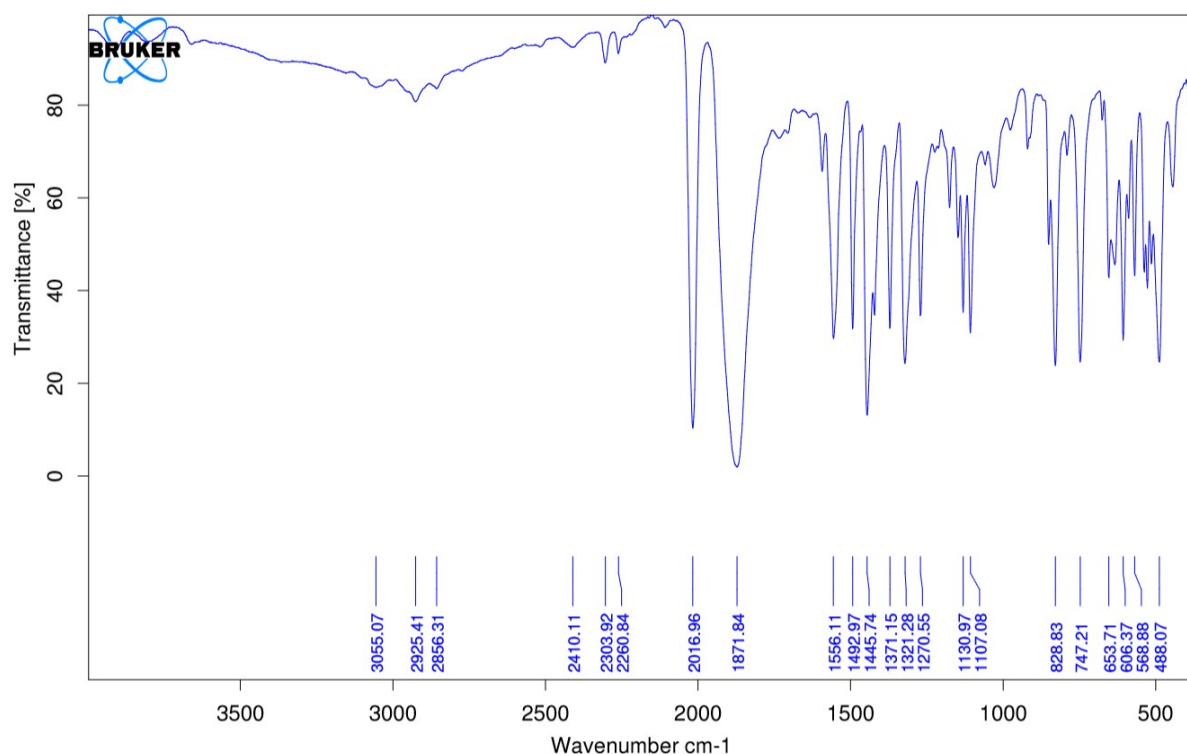


Figure S41. FTIR spectrum of **Re<sub>2</sub>Cl<sub>8</sub>HQ** exhibiting the distinctive A'(1) C≡O stretching frequency at 2017 cm<sup>-1</sup> and the overlapping A'(2) & A'' C≡O stretching frequencies at 1880 cm<sup>-1</sup>. Weaker sp<sup>2</sup> hybridised C–H bond stretches are also observed at higher wavenumbers (*circa* 2925 cm<sup>-1</sup>) from the quinoline ring, and the absence of a broad O–H vibrational band at higher wavenumbers suggests the absence, and thus the coordination, of the hydroxyl group.

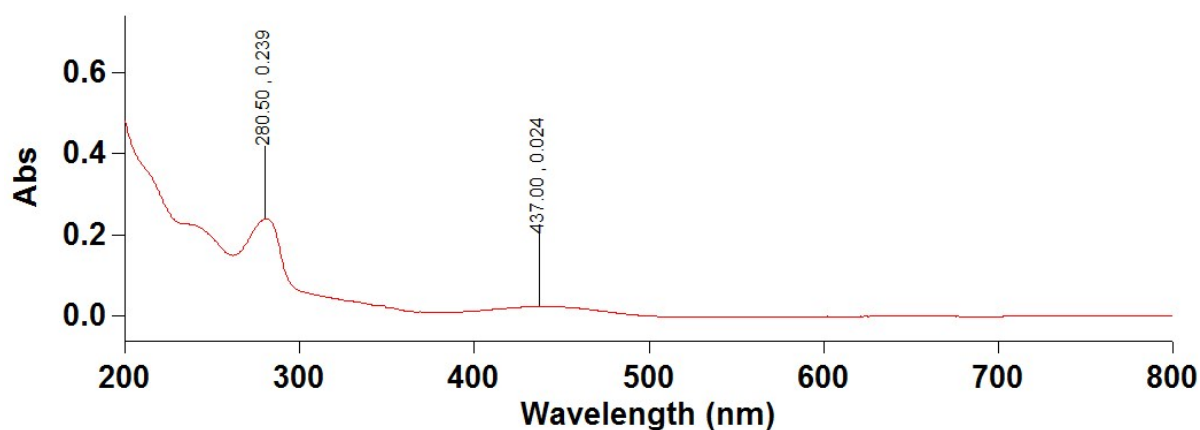


Figure S42. UV-Vis spectrum of **Re<sub>2</sub>Cl<sub>8</sub>HQ** (5 μg.mL<sup>-1</sup>) in acetonitrile exhibiting the absorption band for the dπ → π\* electronic transition to the MLCT excited state at 437 nm, alongside a very distinctive π → π\* transition to a LC excited state at 281 nm.

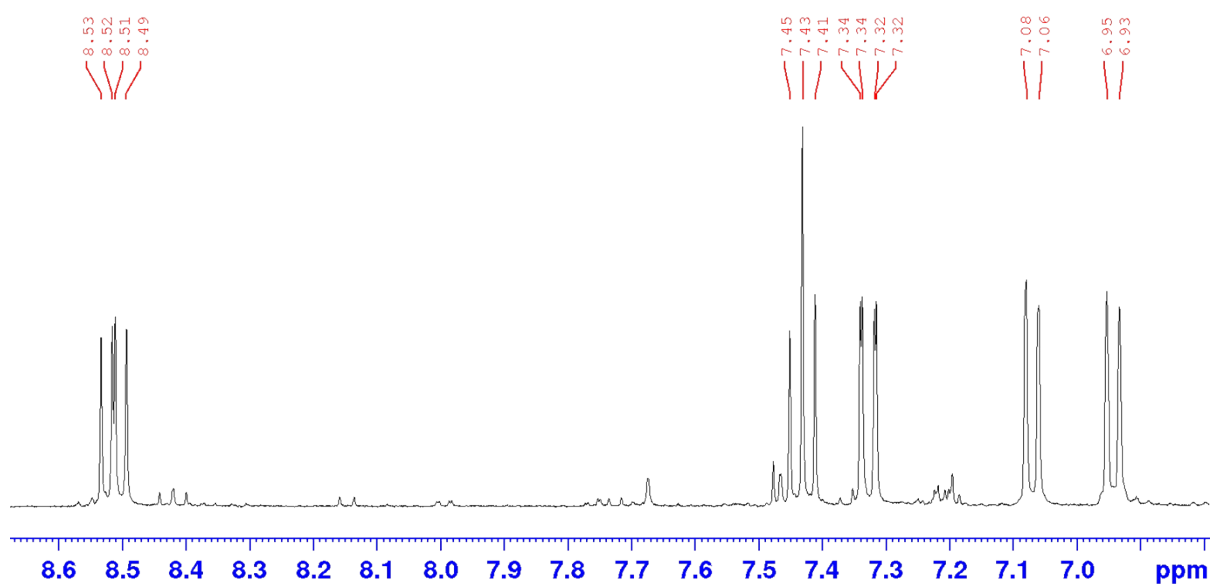


Figure S43.  $^1\text{H}$ -NMR spectrum of **Re2F8HQ** in acetonitrile- $\text{d}_3$  showing the expected integration for five protons in the aromatic region. The resonance signal for the methyl group of the acetonitrilo ancillary ligand is masked behind the residual solvent peak.

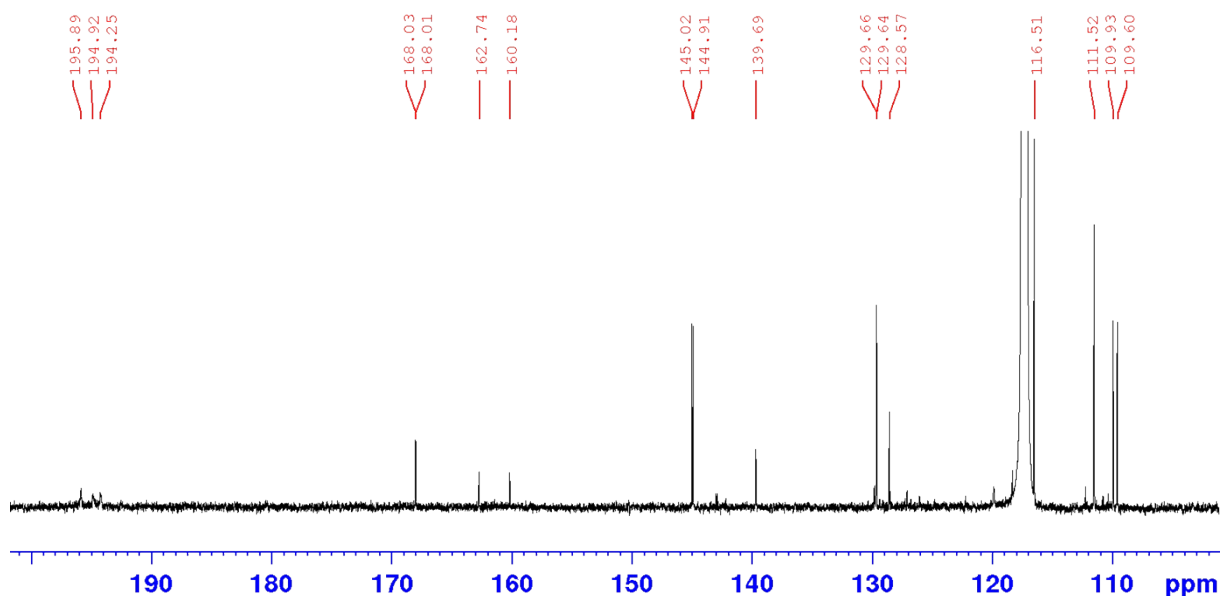


Figure S44.  $^{13}\text{C}$ -NMR spectrum of **Re2F8HQ** in acetonitrile- $\text{d}_3$  showing the three downfield shifted carbon-13 resonance signals of the carbonyl ligands and the nine carbon-13 resonance signals (five split into doublets due to fluorine-19 coupling) of the quinoline ring.

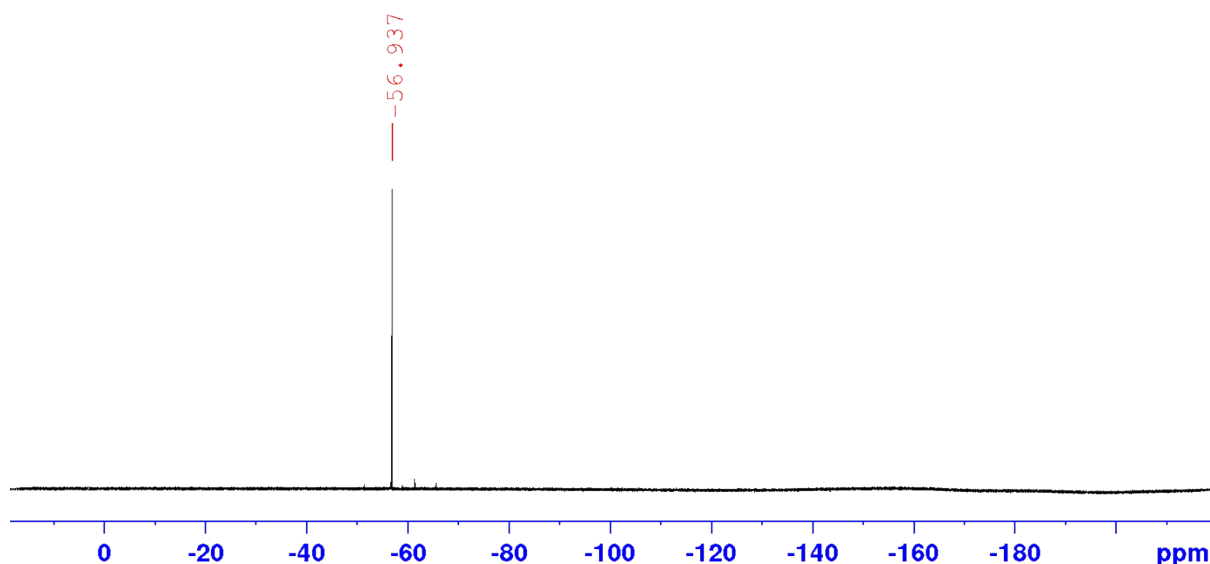


Figure S45. CPD  $^{19}\text{F}$ -NMR spectrum of **Re<sub>2</sub>F<sub>8</sub>HQ** in acetonitrile- $\text{d}_3$ , showing the magnetic resonance signal for the sole fluorine-19 nucleus in the molecule at -56.94 ppm.

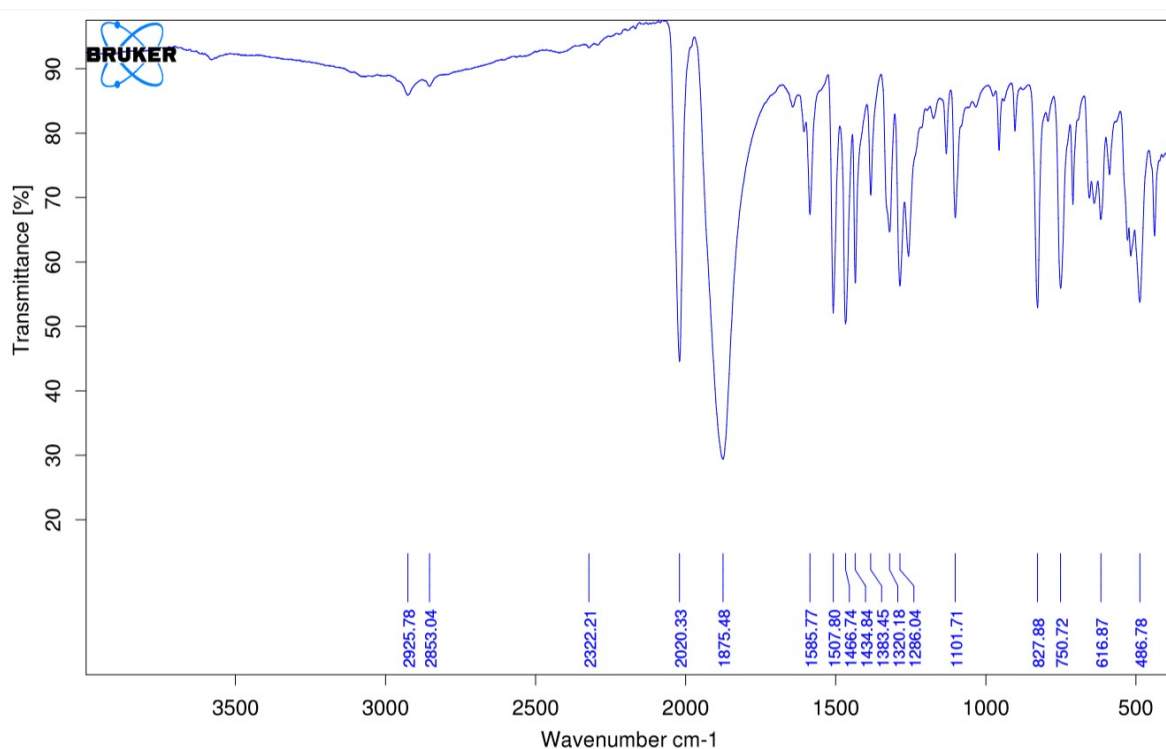


Figure S46. FTIR spectrum of **Re<sub>2</sub>F<sub>8</sub>HQ** exhibiting the distinctive A'(1) C≡O stretching frequency at 2020  $\text{cm}^{-1}$  and the overlapping A'(2) & A'' C≡O stretching frequencies at 1875  $\text{cm}^{-1}$ . Weaker  $\text{sp}^2$  hybridised C–H bond stretches are also observed at higher wavenumbers (circa 2926  $\text{cm}^{-1}$ ) from the quinoline ring, and the absence of a broad O–H vibrational band at higher wavenumbers suggests the absence, and thus the coordination, of the hydroxyl group.

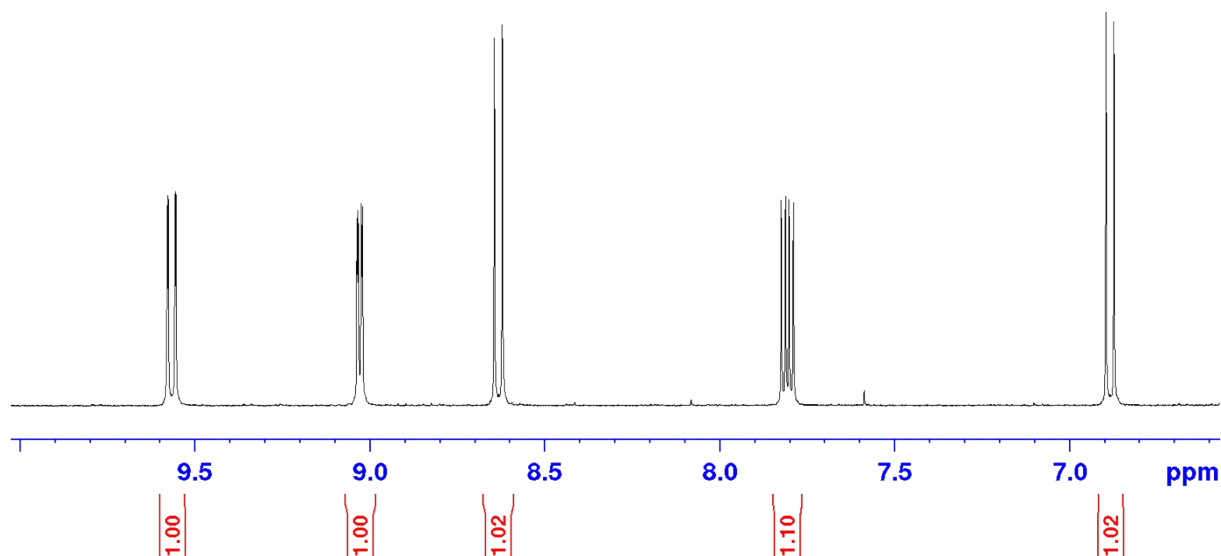


Figure S47.  $^1\text{H-NMR}$  spectrum of **Re5NO<sub>2</sub>8HQ** in acetonitrile- $\text{d}_3$  showing the expected integration for five protons in the aromatic region. The resonance signal for the methyl group of the acetonitrilo ancillary ligand is masked behind the residual solvent peak.

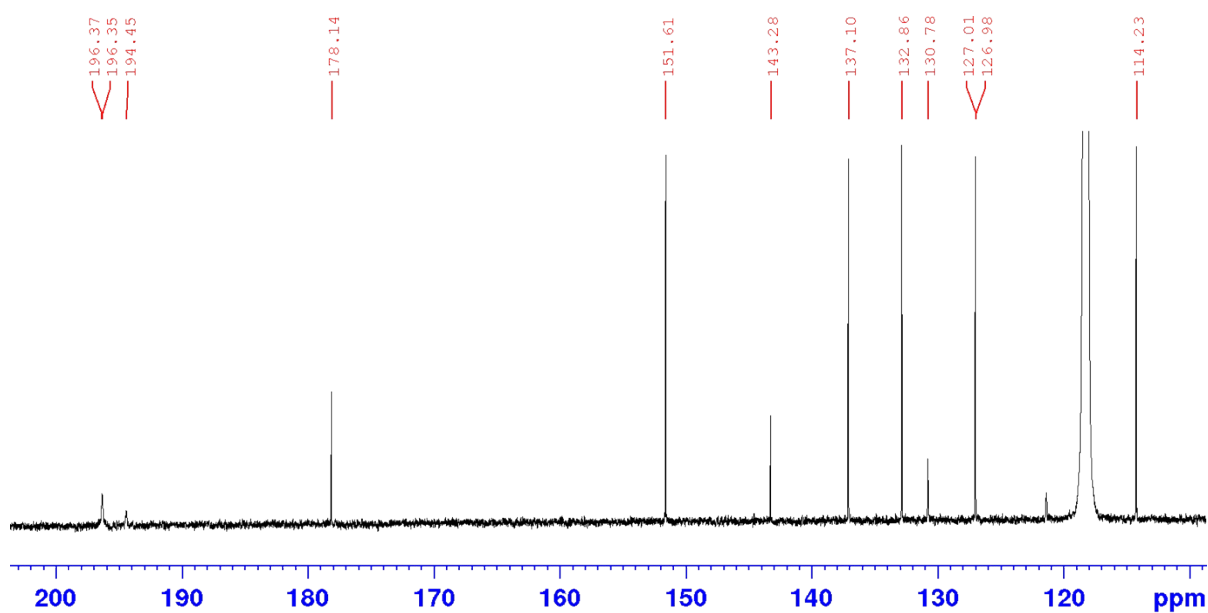


Figure S48.  $^{13}\text{C-NMR}$  spectrum of **Re5NO<sub>2</sub>8HQ** in acetonitrile- $\text{d}_3$  showing the three downfield shifted carbon-13 resonance signals of the carbonyl ligands and the nine carbon-13 resonance signals of the quinoline ring.

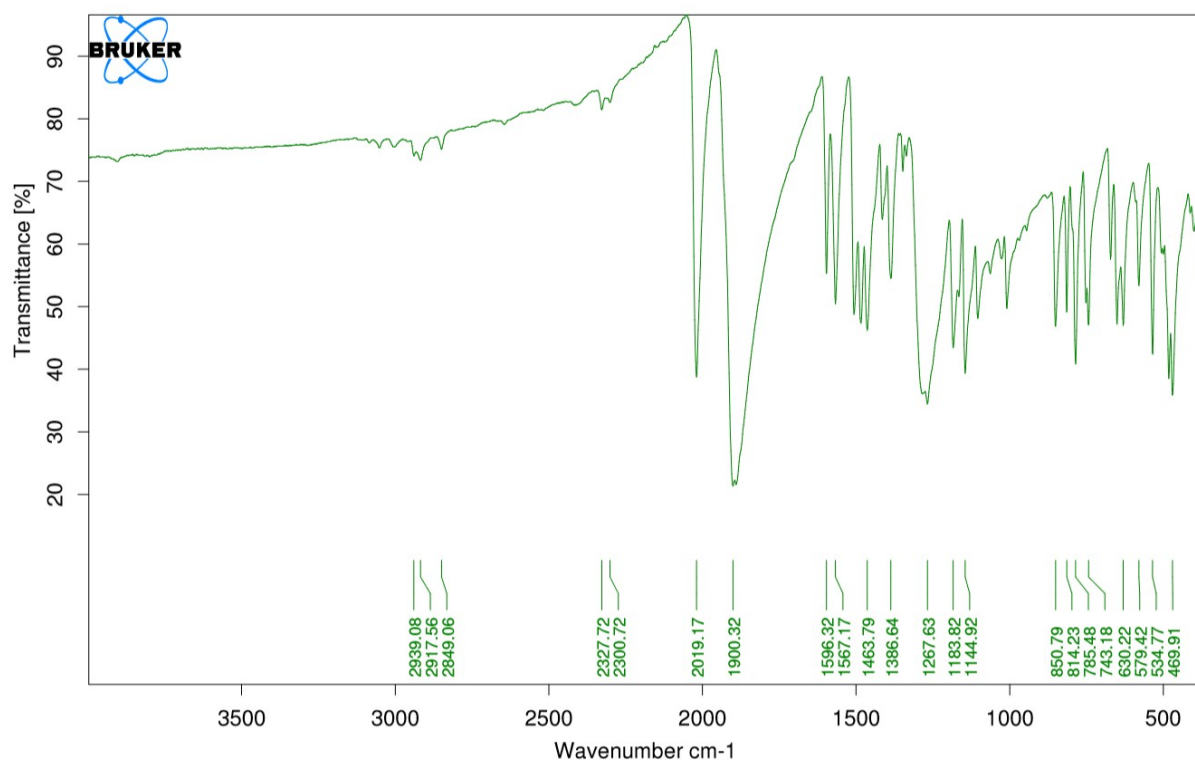


Figure S49. FTIR spectrum of **Re5NO<sub>2</sub>8HQ** exhibiting the distinctive A'(1) C≡O stretching frequency at 2019 cm<sup>-1</sup> and the overlapping A'(2) & A'' C≡O stretching frequencies at 1900 cm<sup>-1</sup>. Weaker sp<sup>2</sup> hybridised C–H bond stretches are also observed at higher wavenumbers (*circa* 2918 cm<sup>-1</sup>) from the quinoline ring, and the absence of a broad O–H vibrational band at higher wavenumbers suggests the absence, and thus the coordination, of the hydroxyl group.

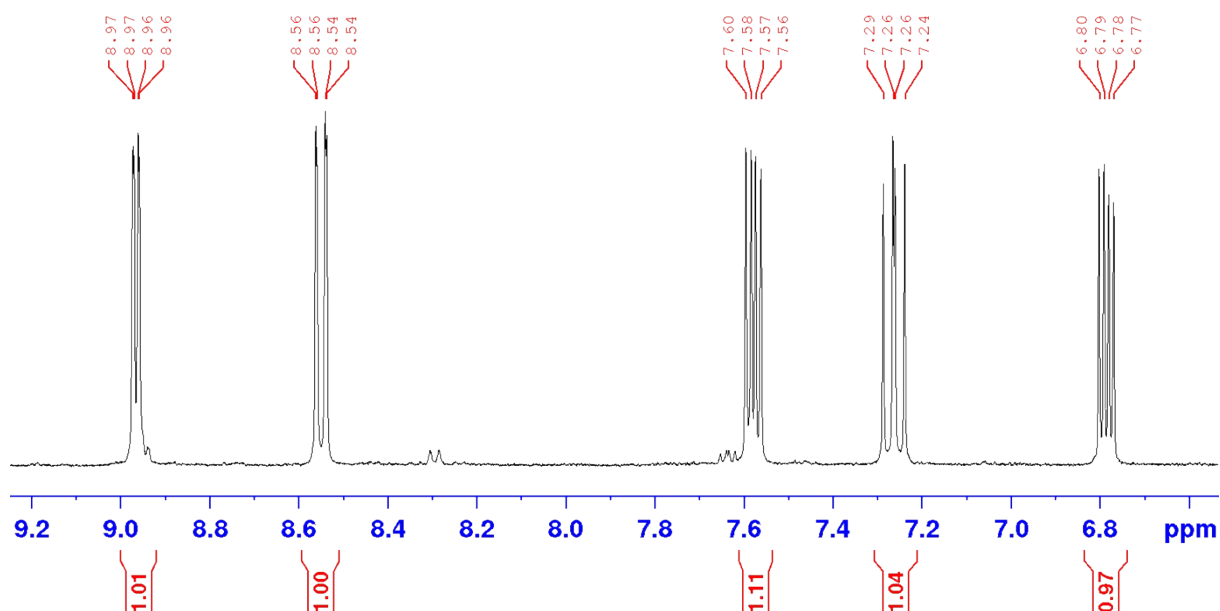


Figure S50. <sup>1</sup>H-NMR spectrum of **Re5F8HQ** in acetonitrile-d<sub>3</sub> showing the expected integration for five protons in the aromatic region. The resonance signal for the methyl group of the acetonitrilo ancillary ligand is masked behind the residual solvent peak.

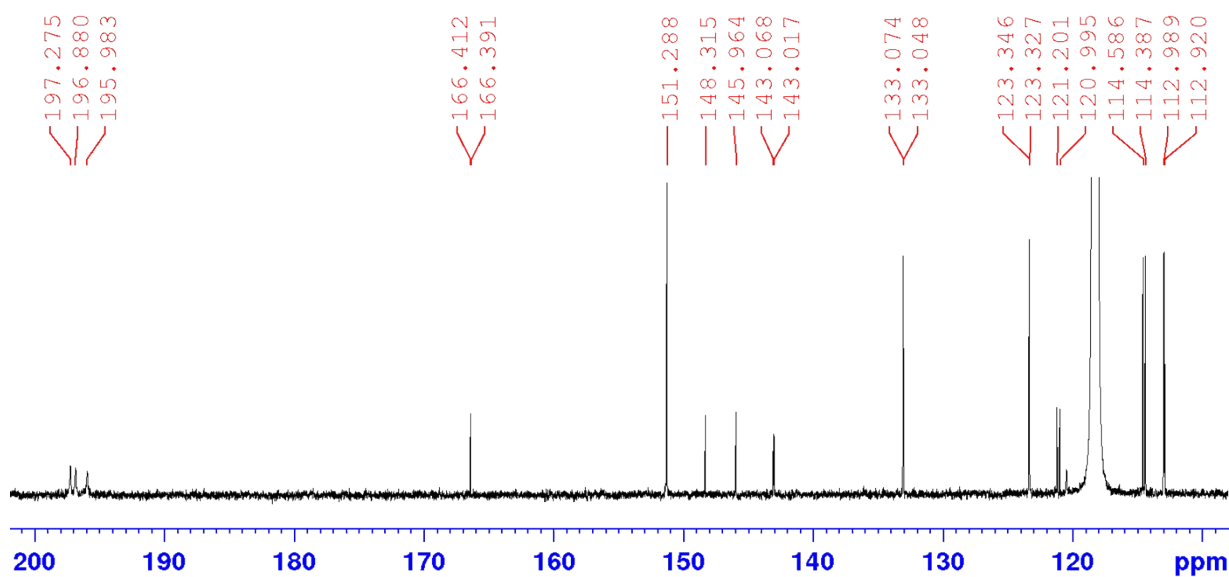


Figure S51.  $^{13}\text{C}$ -NMR spectrum of **Re5F8HQ** in acetonitrile- $\text{d}_3$  showing the three downfield shifted carbon-13 resonance signals of the carbonyl ligands and seventeen carbon-13 resonance signals in the aromatic region due to nine of the quinoline carbon-13 nuclei coupling with the fluorine-19 nucleus.

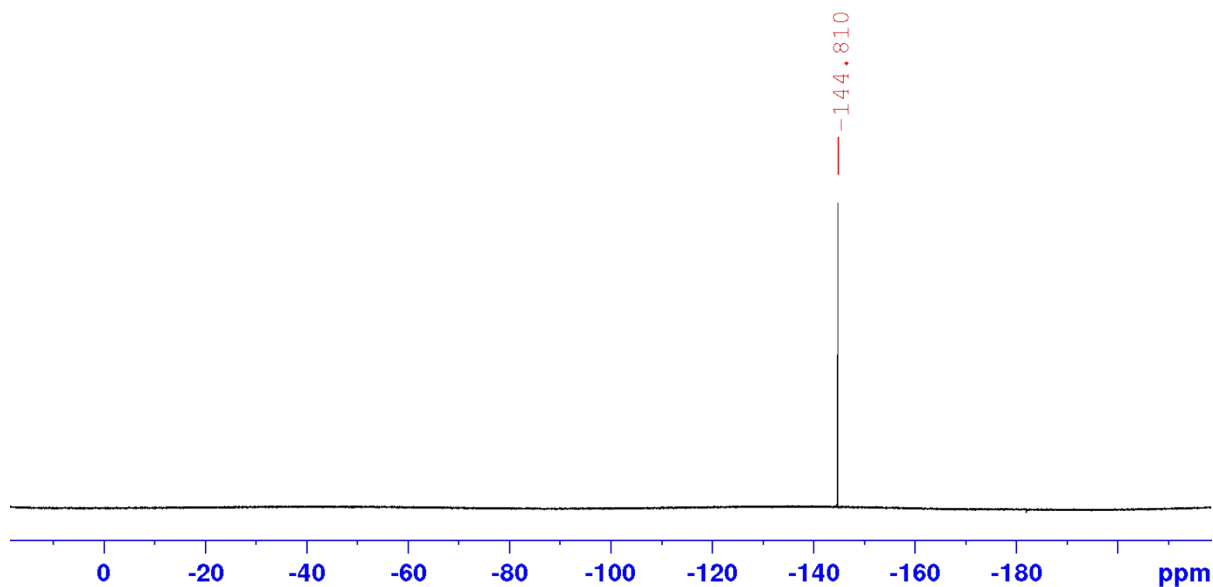


Figure S52. Lone magnetic resonance signal of the fluorine-19 nucleus in the CPD  $^{19}\text{F}$ -NMR spectrum of **Re5F8HQ**.

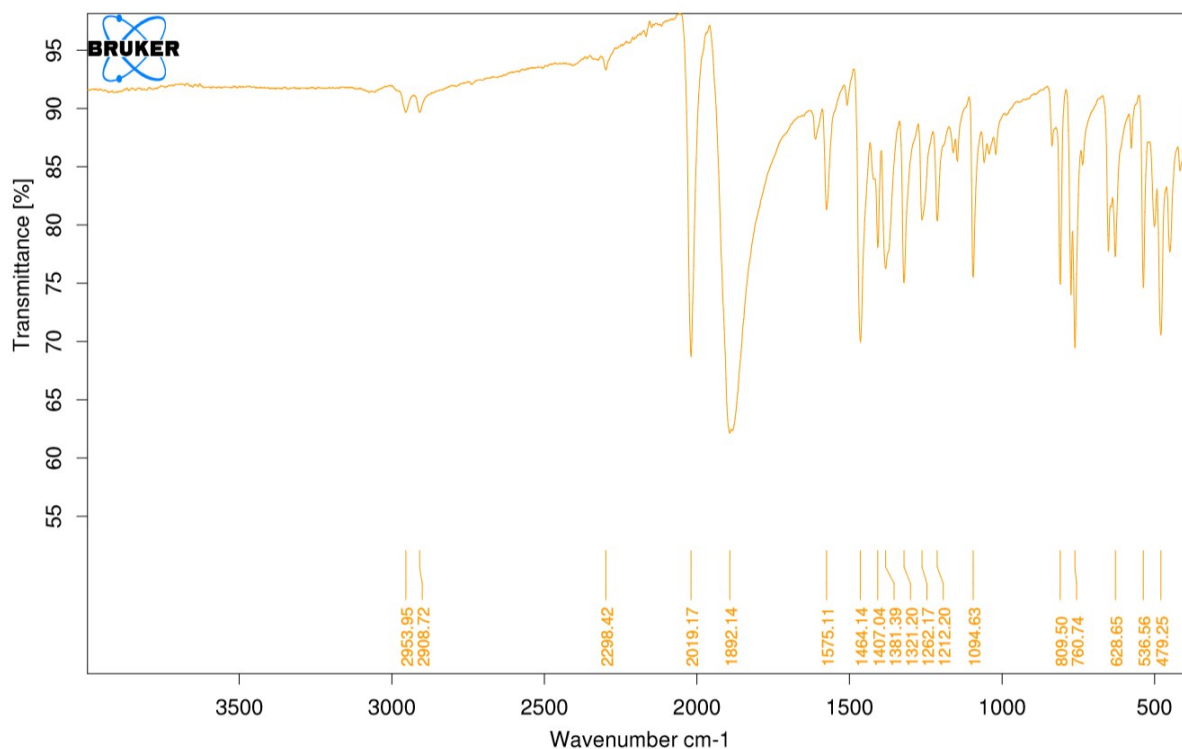


Figure S53. FTIR spectrum of **Re5F8HQ** exhibiting the distinctive A'(1) C≡O stretching frequency at 2019 cm<sup>-1</sup> and the overlapping A'(2) & A'' C≡O stretching frequencies at 1892 cm<sup>-1</sup>. Weaker sp<sup>2</sup> hybridised C–H bond stretches are also observed at higher wavenumbers (*circa* 2953 cm<sup>-1</sup>) from the quinoline ring, and the absence of a broad O–H vibrational band at higher wavenumbers suggests the absence, and thus the coordination, of the hydroxyl group.

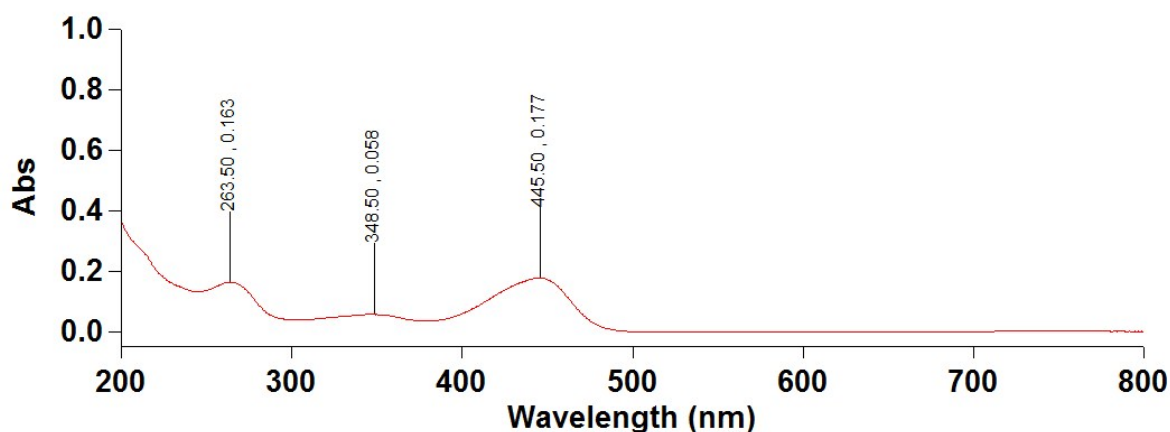


Figure S54. UV-Vis spectrum of **Re5F8HQ** (5 µg.mL<sup>-1</sup>) in acetonitrile exhibiting an absorption band for an electronic transition to either the MLCT excited state of uncharacteristically high molar absorptivity (17570 L.mol<sup>-1</sup>.cm<sup>-1</sup>) or an ILCT excited state at 437 nm.  $\pi \rightarrow \pi^*$  transitions to LC excited states at are also observed at shorter wavelengths.

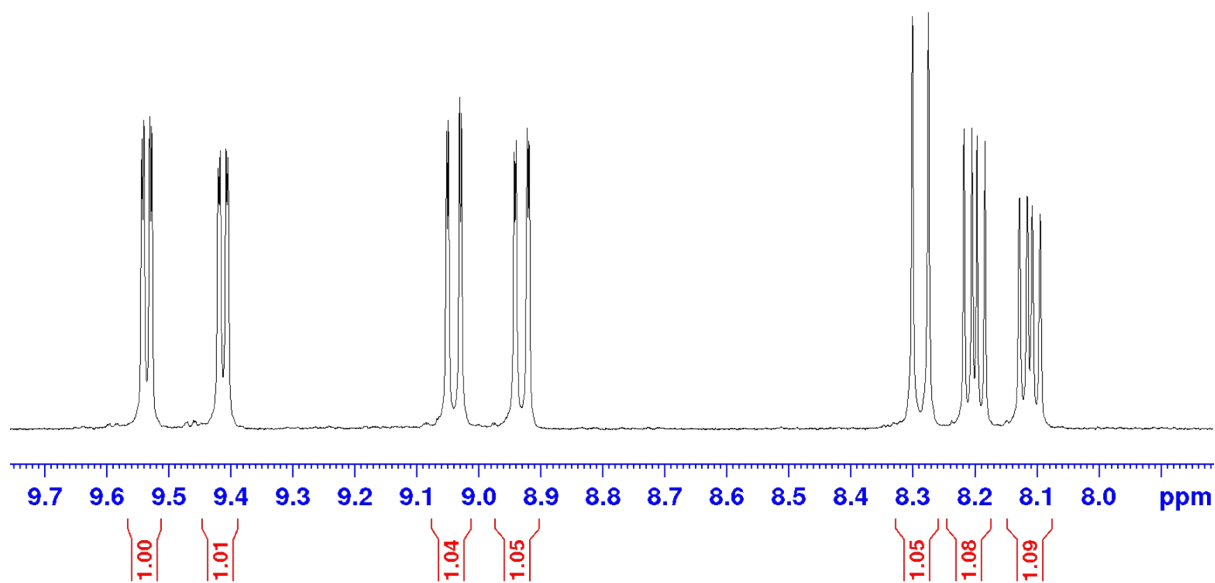


Figure S55. <sup>1</sup>H-NMR spectra of **Re5FPhen** in DMSO-D<sub>6</sub> showing the expected integration for seven protons in the aromatic region.

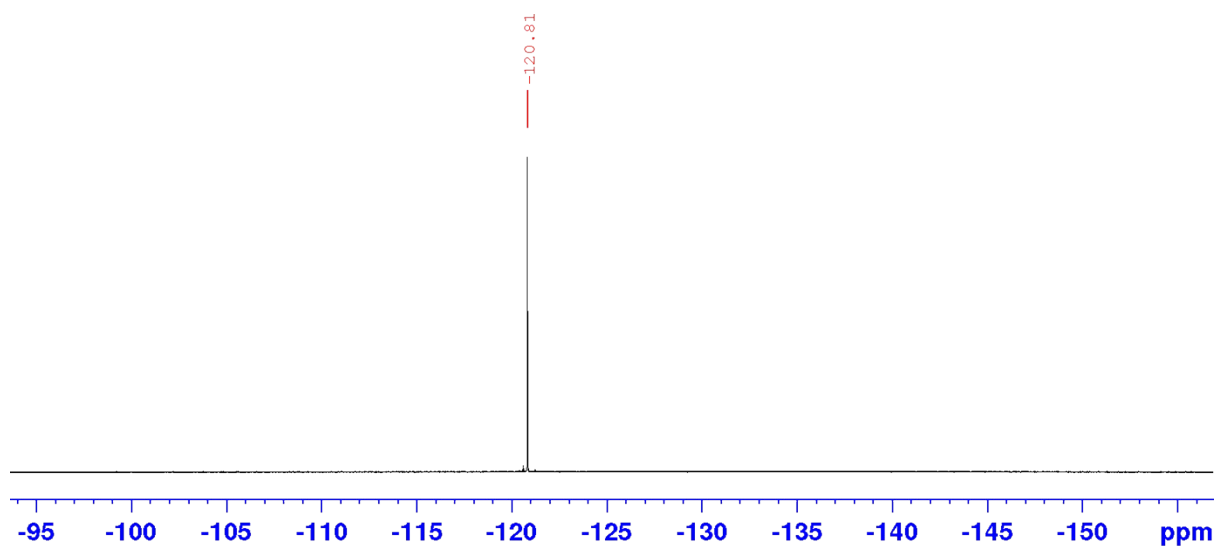


Figure S56. CPD <sup>19</sup>F-NMR spectrum of **Re5FPhen** in DMSO-D<sub>6</sub> solution showing the lone signal of the fluorine-19 nucleus at -120.8 ppm.

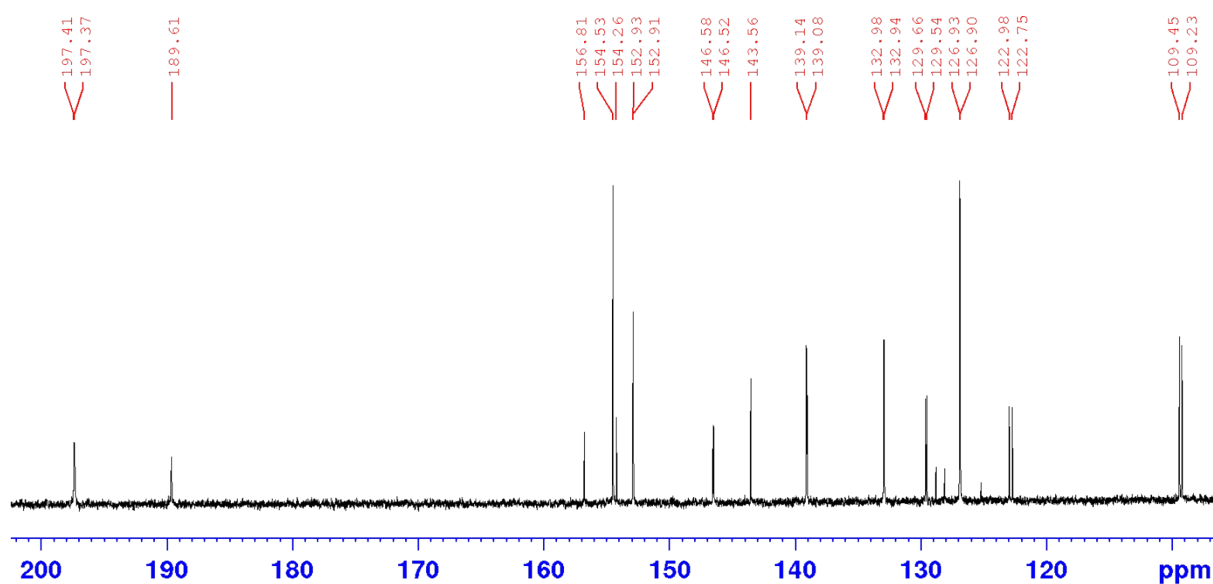


Figure S57.  $^{13}\text{C}$ -NMR spectrum of **Re5FPhen** showing 23 signals, due to the coupling of five of the twelve carbon-13 nuclei in the aromatic region to the fluorine-19 nucleus. Three of these signals at 189.61, 197.37 and 197.41 ppm are indicative of the carbon-13 nuclei in the three carbonyl ligands.

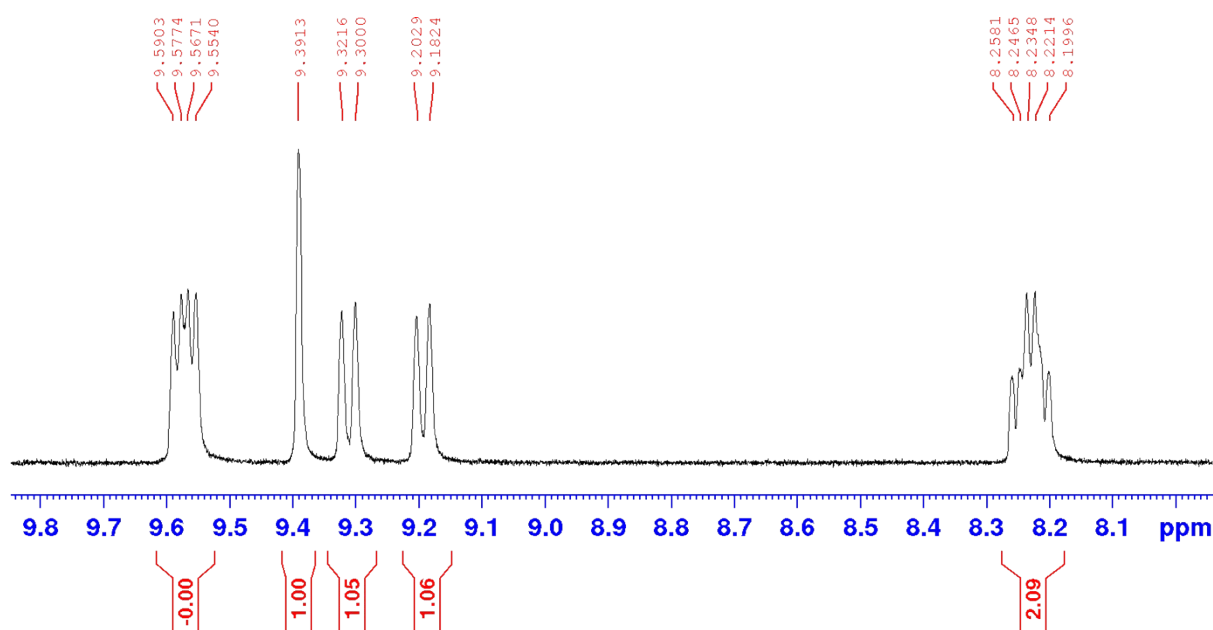


Figure S58.  $^1\text{H}$ -NMR spectrum of **Re5NO<sub>2</sub>Phen** in  $\text{DMSO-d}_6$  showing the expected integration for five protons in the aromatic region.

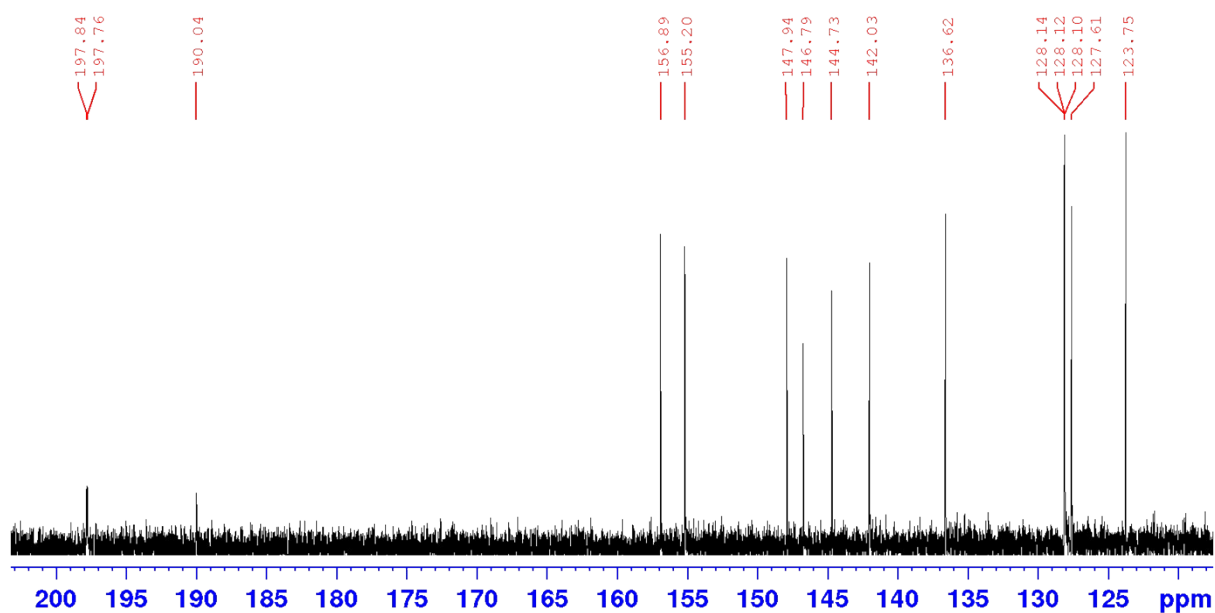


Figure S59.  $^{13}\text{C}$ -NMR spectrum of **Re5NO<sub>2</sub>Phen** in DMSO- $d_6$  showing the three downfield shifted carbon-13 resonance signals of the carbonyl ligands and the twelve carbon-13 resonance signals of the phenanthroline ring.

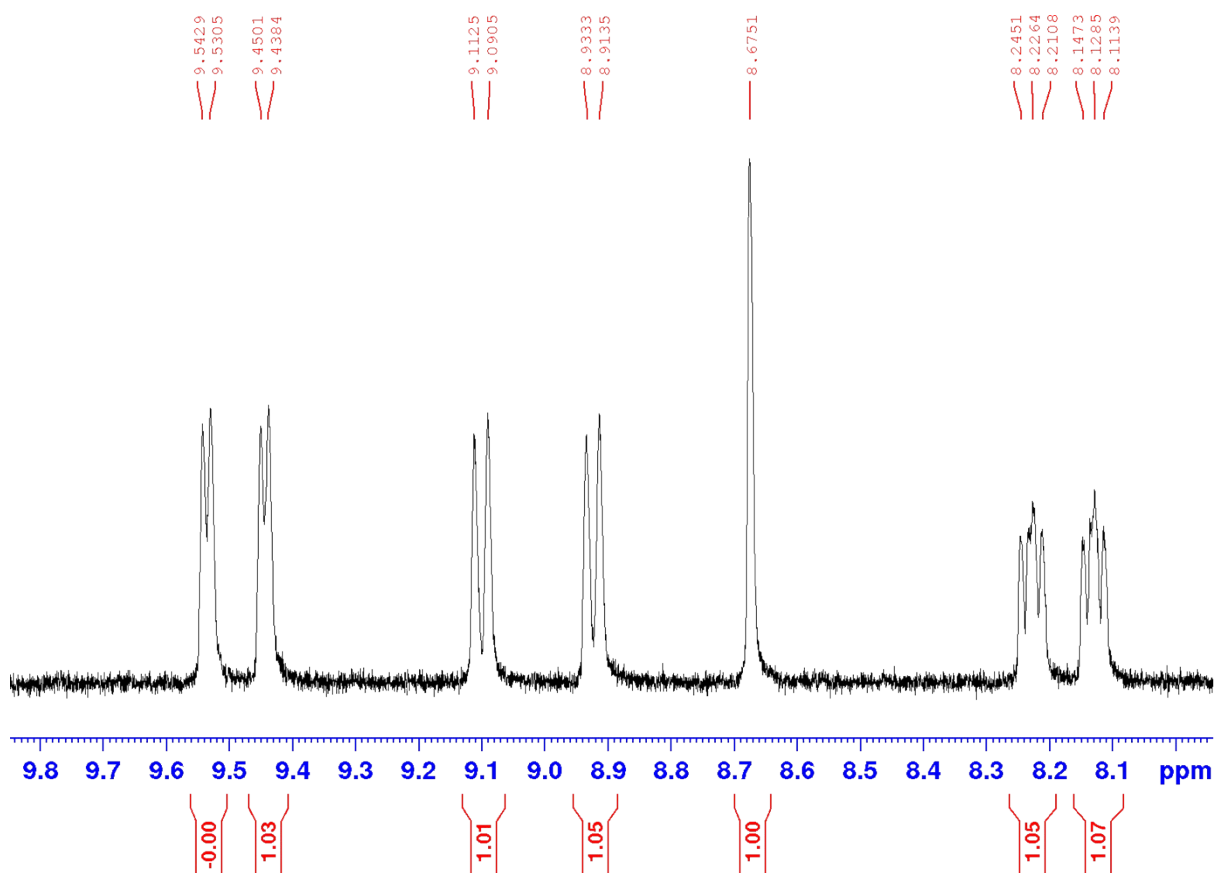


Figure S60.  $^1\text{H}$ -NMR spectrum of **Re5ClPhen** in DMSO- $d_6$  showing the expected integration for five protons in the aromatic region.

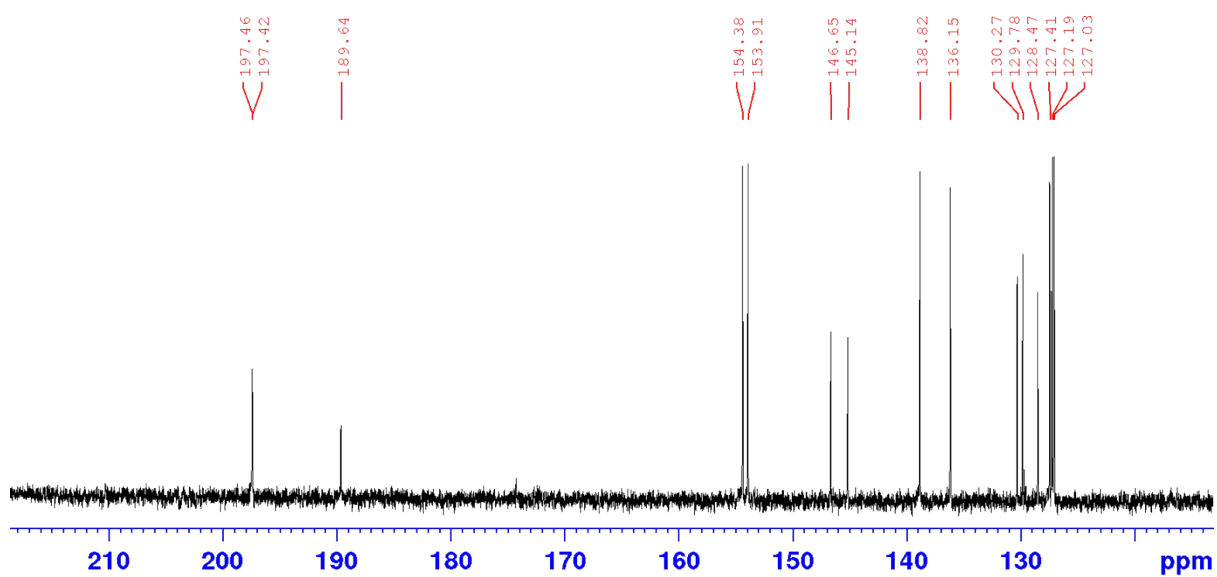


Figure S61.  $^{13}\text{C}$ -NMR spectrum of **Re5ClPhen** in  $\text{DMSO-d}_6$  showing the three downfield shifted carbon-13 resonance signals of the carbonyl ligands and the twelve carbon-13 resonance signals of the phenanthroline ring.

### S.3 Synthesis Characterisation Data of Rhenium Complexes

Tricarbonylchloro(2-chloro-1,10-phenanthroline)rhenium(I) (**Re2ClPhen**). Yellow solid; MP: 316°C (*dec.*); 89% yield. <sup>1</sup>H NMR (400 MHz, DMSO-d<sub>6</sub>, δ/ppm): δ 9.46 (dd, J<sup>d</sup> = 5.12, 1.36 Hz, 1H), δ 8.98 (d, J<sup>d</sup> = 8.52 Hz, 1H), δ 8.97 (d, J<sup>d</sup> = 8.24 Hz, 1H), δ 8.37 (d, J<sup>d</sup> = 8.56, 1H), δ 8.34 (s, 2H), δ 8.12 (dd, J<sup>d</sup> = 8.24, 5.12 Hz, 1H). <sup>13</sup>C{<sup>1</sup>H} NMR (100 MHz, CDCl<sub>3</sub>, δ/ppm): δ 197.88 (C≡O), δ 197.65 (C≡O), δ 189.83 (C≡O), δ 154.75, δ 154.11, δ 147.19, δ 146.56, δ 142.81, δ 139.92, δ 131.69, δ 129.66, δ 128.37, δ 128.09, δ 127.30, δ 127.24. FTIR (ATR *corr.*  $\tilde{\nu}/\text{cm}^{-1}$ ):  $\tilde{\nu}$  3042 (w, C–H sp<sup>2</sup> *str.*),  $\tilde{\nu}$  2021 (s, A'(1) C≡O *str.*),  $\tilde{\nu}$  1889 (s, A'(2) & A'' C≡O *str.*). UV/Vis (CH<sub>3</sub>CN,  $\lambda/\text{nm}$ ,  $\epsilon/\text{L.mol}^{-1}.\text{cm}^{-1}$ ):  $\lambda$  368 (Re( $d\pi$ )→ $\pi^*$ ,  $\epsilon$  374.65),  $\lambda$  270 ( $\pi$ → $\pi^*$ ,  $\epsilon$  2612.13),  $\lambda$  218 ( $\pi$ → $\pi^*$ ,  $\epsilon$  4703.92),  $\lambda$  204 ( $\pi$ → $\pi^*$ ,  $\epsilon$  4589.45). LRMS (ESI<sup>+</sup>): [M-Cl]<sup>+</sup> *m/z* calc. 484.97, *m/z* *obsv.* 485.07. HRMS (ESI<sup>+</sup>): [M+Na]<sup>+</sup> *m/z* *calc.* 540.9261 (C<sub>15</sub>H<sub>7</sub>N<sub>2</sub>O<sub>3</sub>FCl<sub>2</sub>ReNa<sup>+</sup>); *m/z* *obsv.* 540.9266 ( $\Delta$  0.90 ppm). EA (%): *calc.* C 34.62, H 1.36, N 5.38, Cl 13.63; *obsv.* C 34.45, H 0.95, N 5.36, Cl 13.55.

Tricarbonylchloro(2-bromo-1,10-phenanthroline)rhenium(I). (**Re2BrPhen**) Yellow solid; MP: 328 °C (*dec.*), 95% yield. <sup>1</sup>H NMR (400 MHz, DMSO-d<sub>6</sub>, δ/ppm): δ 9.46 (dd, J<sup>d</sup>=5.12 Hz, 1.36 Hz, 1H), δ 8.96 (dd, J<sup>d</sup>=8.24 Hz, 1.36 Hz, 1H), δ 8.82 (d, J<sup>d</sup>=8.56 Hz, 1H), δ 8.49 (d, J<sup>d</sup>=8.56 Hz, 1H), δ 8.34 (d, J<sup>d</sup>=1.44 Hz, 1H), δ 8.32 (d, J<sup>d</sup>=2.48 Hz, 1H), δ 8.11 (dd, J<sup>d</sup>=8.24 Hz, 5.12 Hz, 1H). <sup>13</sup>C{<sup>1</sup>H} NMR (100 MHz, CD<sub>3</sub>CN, δ/ppm): δ 198.0<sub>C=O</sub>, δ 197.1<sub>C=O</sub>, δ 189.8<sub>C=O</sub>, δ 153.5, δ 147.8, δ 147.2, δ 146.4, δ 141.4, δ 139.4, δ 131.3, δ 130.8, δ 129.4, δ 127.8, δ 127.7, δ 126.6. FTIR (ATR *corr.*  $\tilde{\nu}/\text{cm}^{-1}$ ):  $\tilde{\nu}$  3043.35 (w, C–H sp<sup>2</sup> *str.*),  $\tilde{\nu}$  2014.27 (s, A'(1) C≡O *str.*),  $\tilde{\nu}$  1883.98 (s, A'(2) & A'' C≡O *str.*). EA (%): *calc.* C 31.90, H 1.25, N 4.96. *found* C 31.94, H 1.00, N 5.08.

Tricarbonylchloro(2-fluoro-1,10-phenanthroline)rhenium(I) (**Re2FPhen**). Yellow solid; MP: 314°C (*dec.*); 65% yield. <sup>1</sup>H NMR (400 MHz, DMSO-*d*<sub>6</sub>,  $\delta/ppm$ ):  $\delta$  9.47 (dd,  $J^d = 5.04, 1.32$  Hz, 1H),  $\delta$  9.16 (dd,  $J^d = 8.84, 6.80$  Hz, 1H),  $\delta$  8.99 (dd,  $J^d = 8.32, 1.32$  Hz, 1H),  $\delta$  8.36 (*app.* q,  $J^q = 14.72, 8.84$  Hz, 2H),  $\delta$  8.14 (dd,  $J^d = 8.84, 1.48$  Hz, 1H),  $\delta$  8.12 (dd,  $J^d = 8.32, 5.04$  Hz, 1H). <sup>13</sup>C{<sup>1</sup>H} NMR (100 MHz, CDCl<sub>3</sub>,  $\delta/ppm$ ):  $\delta$  197.10 (C≡O),  $\delta$  196.54 (d,  $J^d = 14$  Hz, C≡O),  $\delta$  189.99 (C≡O),  $\delta$  163.77,  $\delta$  161.18,  $\delta$  153.90,  $\delta$  145.79 (d,  $J^d = 11$  Hz),  $\delta$  145.09 (d,  $J^d = 2$  Hz),  $\delta$  144.07 (d,  $J^d = 3$  Hz),  $\delta$  139.48,  $\delta$  130.99,  $\delta$  128.29 (d,  $J^d = 1$  Hz),  $\delta$  127.32 (d,  $J^d = 2$  Hz),  $\delta$  127.09 (d,  $J^d = 61$  Hz),  $\delta$  113.48 (d,  $J^d = 32$  Hz). <sup>19</sup>F NMR (376 MHz, DMSO-*d*<sub>6</sub>,  $\delta/ppm$ ):  $\delta$  -36.75 (dd,  $J^d = 6.92, 1.92$  Hz),  $\delta$  -106.00 (ISTD: *para*-DFB). FTIR (ATR *corr.*  $\tilde{\nu}/cm^{-1}$ ):  $\tilde{\nu}$  3077 (w, C–H *sp*<sup>2</sup> *str.*),  $\tilde{\nu}$  2021 (s, A'(1) C≡O *str.*),  $\tilde{\nu}$  1890 (s, A'(2) & A'' C≡O *str.*). UV/Vis (CH<sub>3</sub>CN,  $\lambda/nm$ ,  $\epsilon/L.mol^{-1}.cm^{-1}$ ):  $\lambda$  375 (Re(*d* $\pi$ ) $\rightarrow\pi^*$ ,  $\epsilon$  2720.95),  $\lambda$  343 ( $\pi\rightarrow\pi^*$ ,  $\epsilon$  2821.73),  $\lambda$  269 ( $\pi\rightarrow\pi^*$ ,  $\epsilon$  22069.94),  $\lambda$  262 ( $\pi\rightarrow\pi^*$ ,  $\epsilon$  22170.71),  $\lambda$  215 ( $\pi\rightarrow\pi^*$ ,  $\epsilon$  38798.75),  $\lambda$  200 ( $\pi\rightarrow\pi^*$ ,  $\epsilon$  40915.05). LRMS (ESI<sup>+</sup>): [M-Cl]<sup>+</sup> *m/z* calc. 469.00, *m/z* obsv. 469.12. HRMS (ESI<sup>+</sup>): [M+Na]<sup>+</sup> *m/z* calc. 524.9557 (C<sub>15</sub>H<sub>7</sub>N<sub>2</sub>O<sub>3</sub>FCIReNa<sup>+</sup>); *m/z* obsv. 524.9579 ( $\Delta$  4.20 ppm). EA (%): *calc.* C 35.75, H 1.40, N 5.56, Cl 7.04; *obsv.* C 35.73, H 0.98, N 5.59, Cl 6.83.

Tricarbonylchloro(6-chloro-2,2'-bipyridine)rhenium(I) (**Re6ClBiPy**) Yellow solid; MP: 255 °C; 86% yield. <sup>1</sup>H NMR (400 MHz, DMSO-*d*<sub>6</sub>,  $\delta/ppm$ ):  $\delta$  9.06 (d,  $J^d=4.76$  Hz, 1H),  $\delta$  8.76 (d,  $J^d=8.12$  Hz, 2H),  $\delta$  8.35 (*app.* td,  $J^d=1.96, J^t=8.04$  Hz, 2H),  $\delta$  8.08 (dd,  $J^d=0.68, 8.04$  Hz, 1H),  $\delta$  7.78 (*app.* td,  $J^d=1.80, J^t=4.56$  Hz, 1H). <sup>13</sup>C{<sup>1</sup>H} NMR (100 MHz, DMSO-*d*<sub>6</sub>,  $\delta/ppm$ ):  $\delta$  197.5<sub>C=O</sub>,  $\delta$  197.3<sub>C=O</sub>,  $\delta$  189.5<sub>C=O</sub>,  $\delta$  157.2,  $\delta$  155.6,  $\delta$  153.2,  $\delta$  152.8,  $\delta$  142.7,  $\delta$  140.3,  $\delta$  128.0,  $\delta$  127.7,  $\delta$  125.3,  $\delta$  123.1. FTIR (ATR *corr.*  $\tilde{\nu}/cm^{-1}$ ):  $\tilde{\nu}$  3075 (w, C–H *sp*<sup>2</sup> *str.*),  $\tilde{\nu}$  2018 (s, A'(1) C≡O *str.*),  $\tilde{\nu}$  1882 (s, A'(2) & A'' C≡O *str.*). UV/Vis ( $\lambda/nm$ ,  $\epsilon/L.mol^{-1}.cm^{-1}$ ):  $\lambda$  380 (*d* $\pi\rightarrow\pi^*$ ,  $\epsilon$  3375.36),  $\lambda$  301 ( $\pi\rightarrow\pi^*$ ,  $\epsilon$  14990.57),  $\lambda$  326 ( $\pi\rightarrow\pi^*$ ,  $\epsilon$  10920.28),  $\lambda$  233 ( $\pi\rightarrow\pi^*$ ,  $\epsilon$  19259.41). LRMS (ESI<sup>+</sup>): [M-Cl]<sup>+</sup> *m/z* calcd: 460.97, *m/z* obsv 460.95. HRMS (ESI<sup>+</sup>): [M-Cl]<sup>+</sup> *m/z* calcd:

460.9703,  $m/z$  obsvs 460.9694 ( $\Delta$  -2.0 ppm). EA (%): *calc.* C 31.46, H 1.42, N 5.64. *found* C 31.59, H 1.17, N 5.70.

*Tricarbonylchloro(6-fluoro-2,2'-bipyridine)rhenium(I)* (**Re6FBiPy**) Yellow solid; MP: 294 °C, 65% yield.  $^1\text{H}$  NMR (400 MHz, DMSO- $d_6$ ,  $\delta/ppm$ ):  $\delta$  9.06 (*app.* tq,  $J^t=5.48$  Hz,  $J^q=0.80$  Hz, 1H),  $\delta$  8.80 (d,  $J^d=8.16$  Hz, 1H),  $\delta$  8.70 (d,  $J^d=7.92$  Hz, 1H),  $\delta$  8.52 (q,  $J^q=8.04$  Hz, 1H),  $\delta$  8.36 (td,  $J^t=8.08$  Hz,  $J^d=1.52$  Hz, 1H),  $\delta$  7.80 (m, 2H).  $^{13}\text{C}\{^1\text{H}\}$  NMR (100 MHz, DMSO- $d_6$ ,  $\delta/ppm$ ):  $\delta$  197.2 $_{\text{C=O}}$ ,  $\delta$  196.6 $_{\text{C=O}}$  (d,  $J^d=16.59$  Hz),  $\delta$  188.9 $_{\text{C=O}}$ ,  $\delta$  164.0,  $\delta$  161.5,  $\delta$  154.4 (d,  $J^d=15.92$  Hz),  $\delta$  153.1,  $\delta$  145.9 (d,  $J^d=10.15$  Hz),  $\delta$  140.4,  $\delta$  128.2,  $\delta$  125.1,  $\delta$  121.4 (d,  $J^d=2.94$  Hz),  $\delta$  112.7 (d,  $J^d=30.19$  Hz).  $^{19}\text{F}\{^1\text{H}\}$  NMR (376 MHz, DMSO- $d_6$ ,  $\delta/ppm$ ):  $\delta$  -51.75. FTIR (ATR *corr.*  $\tilde{\nu}/\text{cm}^{-1}$ ):  $\tilde{\nu}$  3040 (w, C-H  $\text{sp}^2$  *str.*),  $\tilde{\nu}$  2016 (s, A'(1) C $\equiv$ O *str.*),  $\tilde{\nu}$  1880 (s, A'(2) & A'' C $\equiv$ O *str.*). UV/Vis ( $\lambda/\text{nm}$ ,  $\epsilon/\text{L.mol}^{-1}.\text{cm}^{-1}$ ):  $\lambda$  369 ( $d\pi\rightarrow\pi^*$ ,  $\epsilon$  2768.36),  $\lambda$  296 ( $\pi\rightarrow\pi^*$ ,  $\epsilon$  12485.88),  $\lambda$  235 ( $\pi\rightarrow\pi^*$ ,  $\epsilon$  15367.33). LRMS (ESI $^+$ ): [M-Cl] $^+$   $m/z$  calcd: 445.00,  $m/z$  obsvs 445.10. EA (%): *calc.* C 32.54, H 1.47, N 5.84. *found* C 32.59, H 1.16, N 5.88.

*Tricarbonylchloro(4-chloro-2,2'-bipyridine)rhenium(I)* (**Re4ClBiPy**). Yellow solid; MP: 283 °C; 89% yield.  $^1\text{H}$  NMR (400 MHz, DMSO- $d_6$ ,  $\delta/ppm$ ):  $\delta$  9.04 (d,  $J^d=4.68$  Hz, 1H),  $\delta$  9.01 (d,  $J^d=2.04$  Hz, 1H),  $\delta$  8.96 (d,  $J^d=6.00$  Hz, 1H),  $\delta$  8.85 (d,  $J^d=8.16$  Hz, 1H),  $\delta$  8.36 (*app.* td,  $J^t=8.04$  Hz,  $J^d=1.32$ , 1H),  $\delta$  7.88 (dd,  $J^d=2.12$ , 6.00 Hz, 1H),  $\delta$  8.36 (*app.* td,  $J^d=1.12$ ,  $J^t=5.56$  Hz, 1H).  $^{13}\text{C}\{^1\text{H}\}$  NMR (100 MHz, DMSO- $d_6$ ,  $\delta/ppm$ ):  $\delta$  197.6 $_{\text{C=O}}$ ,  $\delta$  197.5 $_{\text{C=O}}$ ,  $\delta$  189.7 $_{\text{C=O}}$ ,  $\delta$  156.9,  $\delta$  154.3,  $\delta$  153.8,  $\delta$  153.1,  $\delta$  147.0,  $\delta$  140.3,  $\delta$  128.4,  $\delta$  127.7,  $\delta$  125.0,  $\delta$  124.7. FTIR (ATR *corr.*  $\tilde{\nu}/\text{cm}^{-1}$ ):  $\tilde{\nu}$  3117 (w, C-H  $\text{sp}^2$  *str.*),  $\tilde{\nu}$  2019 (s, A'(1) C $\equiv$ O *str.*),  $\tilde{\nu}$  1884 (s, A'(2) & A'' C $\equiv$ O *str.*). UV/Vis ( $\lambda/\text{nm}$ ,  $\epsilon/\text{L.mol}^{-1}.\text{cm}^{-1}$ ):  $\lambda$  380 ( $d\pi\rightarrow\pi^*$ ,  $\epsilon$  7548.93),  $\lambda$  292 ( $\pi\rightarrow\pi^*$ ,  $\epsilon$  38022.44),  $\lambda$  235 ( $\pi\rightarrow\pi^*$ ,  $\epsilon$  48347.07). LRMS (ESI $^+$ ): [M-Cl] $^+$   $m/z$  calcd: 460.97,  $m/z$  obsvs 460.95. HRMS (ESI $^+$ ): [M-Cl] $^+$   $m/z$  calcd: 460.9703,  $m/z$  obsvs 460.9712 ( $\Delta$  2.0 ppm). EA (%): *calc.* C 31.46, H 1.42, N 5.64. *found* C 31.81, H 1.20, N 5.32.

*Tricarbonylchloro(4-fluoro-2,2'-bipyridine)rhenium(I)* (**Re4FBiPy**). Yellow solid; MP: 302 °C; 38% yield. <sup>1</sup>H NMR (400 MHz, DMSO-d<sub>6</sub>, δ/ppm): δ 9.04 (*app.* t, J<sup>t</sup>=6.72 Hz, 2H), δ 8.78 (m, 2H), δ 8.36 (td, J<sup>d</sup>=1.44, J<sup>t</sup>=7.92 Hz, 1H), δ 7.79 (qd, J<sup>d</sup>=1.12, J<sup>q</sup>=7.56 Hz, 1H), δ 7.69 (qd, J<sup>d</sup>=1.00, J<sup>q</sup>=7.36 Hz, 1H). <sup>13</sup>C {<sup>1</sup>H} NMR (100 MHz, DMSO-d<sub>6</sub>, δ/ppm): δ 197.6<sub>C=O</sub>, δ 197.6<sub>C=O</sub>, δ 189.9<sub>C=O</sub>, δ 168.3, δ 168.3, δ 158.9 (d, J<sup>d</sup>=10.26 Hz), δ 156.2 (d, J<sup>d</sup>=9.99 Hz), δ 154.6, δ 153.1, δ 140.5, δ 128.5, δ 124.9, δ 116.0 (d, J<sup>d</sup>=19.7 Hz), δ 113.0 (d, J<sup>d</sup>=22.79 Hz). <sup>19</sup>F {<sup>1</sup>H} NMR (376 MHz, DMSO-d<sub>6</sub>, δ/ppm): δ -94.71. FTIR (ATR corr.  $\tilde{\nu}/\text{cm}^{-1}$ ):  $\tilde{\nu}$  3117 (w, C–H sp<sup>2</sup> str.),  $\tilde{\nu}$  2018 (s, A'(1) C≡O str.),  $\tilde{\nu}$  1884 (s, A'(2) & A'' C≡O str.). LRMS (ESI<sup>+</sup>): [M-Cl]<sup>+</sup> *m/z* calcd: 445.00, *m/z* obvs 444.92. EA (%): *calc.* C 32.54, H 1.47, N 5.84. *found* C 32.52, H 1.33, N 5.81.

*Tricarbonylchloro(5-chloro-2,2'-bipyridine)rhenium(I)* (**Re5ClBiPy**). Yellow solid; MP: 292 °C, 50% yield. <sup>1</sup>H NMR (400 MHz, DMSO-d<sub>6</sub>, δ/ppm): δ 9.03 (d, J<sup>d</sup>=2.28 Hz, 2H), δ 8.80 (t, J<sup>t</sup>=8.92 Hz, 2H), δ 8.55 (dd, J<sup>d</sup>=8.84, 2.28 Hz, 1H), δ 8.35 (td, J<sup>t</sup>=8.04 Hz, J<sup>d</sup> = 1.32 Hz, 1H), δ 7.77 (*app.* qd, J<sup>q</sup>=5.68 Hz, J<sup>d</sup>=1.16 Hz, 1H). <sup>13</sup>C {<sup>1</sup>H} NMR (100 MHz, DMSO-d<sub>6</sub>, δ/ppm): δ 197.5<sub>C=O</sub>, δ 197.2<sub>C=O</sub>, δ 189.6<sub>C=O</sub>, δ 154.2, δ 154.1, δ 153.0, δ 150.9, δ 140.4, δ 140.2, δ 133.9, δ 128.1, δ 125.3, δ 124.8. FTIR (ATR corr.  $\tilde{\nu}/\text{cm}^{-1}$ ):  $\tilde{\nu}$  3113 (w, C–H sp<sup>2</sup> str.),  $\tilde{\nu}$  2021 (s, A'(1) C≡O str.),  $\tilde{\nu}$  1883 (s, A'(2) & A'' C≡O str.). UV/Vis ( $\lambda/\text{nm}$ ,  $\epsilon/\text{L}\cdot\text{mol}^{-1}\cdot\text{cm}^{-1}$ ):  $\lambda$  379 ( $d\pi\rightarrow\pi^*$ ,  $\epsilon$  7346.37),  $\lambda$  299 ( $\pi\rightarrow\pi^*$ ,  $\epsilon$  36136.21),  $\lambda$  241 ( $\pi\rightarrow\pi^*$ ,  $\epsilon$  42589.10). LRMS (ESI<sup>+</sup>): [M-Cl]<sup>+</sup> *m/z* calcd: 460.97, *m/z* obvs 460.95. HRMS (ESI<sup>+</sup>): [M-Cl]<sup>+</sup> *m/z* calcd: 460.9703, *m/z* obvs 460.9730 ( $\Delta$  5.9 ppm). EA (%): *calc.* C 31.46, H 1.42, N 5.64. *found* C 31.61, H 1.14, N 5.44.

*Tricarbonylchloro(6-bromo-2,2'-bipyridine)rhenium(I)* (**Re6BrBiPy**). Yellow solid; MP: 260 °C, 86% yield. <sup>1</sup>H NMR (400 MHz, DMSO-d<sub>6</sub>, δ/ppm): δ 9.06 (dd, J<sup>d</sup>=5.48 Hz, 0.80 Hz, 1H), δ 8.77 (q, J<sup>q</sup>=5.16 Hz, 4.08 Hz, 1H), δ 8.71 (d, J<sup>d</sup>=8.24 Hz, 1H), δ 8.33 (td, J<sup>t</sup>=8.08 Hz, J<sup>d</sup>=1.52 Hz, 1H), δ 8.20 (d, J<sup>d</sup>=1.40 Hz, 1H), δ 8.19 (s, 1H), δ 7.76 (qd, J<sup>q</sup>=5.52 Hz, 1.24 Hz, J<sup>d</sup>=1.04 Hz, 1H). <sup>13</sup>C {<sup>1</sup>H} NMR (100 MHz, CD<sub>3</sub>CN, δ/ppm): δ 198.1<sub>C=O</sub>, δ 197.2<sub>C=O</sub>, δ 190.0<sub>C=O</sub>, δ

157.6,  $\delta$  156.0,  $\delta$  152.7,  $\delta$  146.2,  $\delta$  142.0,  $\delta$  140.2,  $\delta$  131.9,  $\delta$  127.8,  $\delta$  125.3,  $\delta$  123.3. FTIR (ATR *corr.*  $\tilde{\nu}/\text{cm}^{-1}$ ):  $\tilde{\nu}$  3074 (w, C–H  $\text{sp}^2$  *str.*),  $\tilde{\nu}$  2017 (s, A'(1) C $\equiv$ O *str.*),  $\tilde{\nu}$  1884 (s, A'(2) & A'' C $\equiv$ O *str.*). LRMS (ESI<sup>+</sup>): [M–Cl]<sup>+</sup> *m/z* calcd: 504.92, *m/z* obsvs 505.04. EA (%): *calc.* C 28.87, H 1.30, N 5.18. *found* C 28.90, H 1.05, N 5.21.

*Acetonitriletricarboxyl(2-chloro-8-quinolinolate)rhenium(I)* (**Re2Cl8HQ**) Amber solid; MP: 130 °C, 32% yield. <sup>1</sup>H NMR (400 MHz, CD<sub>3</sub>CN,  $\delta/\text{ppm}$ ):  $\delta$  8.32 (d,  $J^d=8.68$  Hz, 1H),  $\delta$  7.58 (d,  $J^d=8.68$  Hz, 1H),  $\delta$  7.43 (t,  $J^t=7.96$  Hz, 1H),  $\delta$  7.01 (dd,  $J^d=7.96$ , 0.96 Hz, 1H),  $\delta$  6.92 (dd,  $J^d=7.96$ , 1.04 Hz, 1H),  $\delta$  1.96 (s, 3H). <sup>13</sup>C{<sup>1</sup>H} NMR (100 MHz, CD<sub>3</sub>CN,  $\delta/\text{ppm}$ ):  $\delta$  196.6<sub>C=O</sub>,  $\delta$  195.3<sub>C=O</sub>,  $\delta$  195.3<sub>C=O</sub>,  $\delta$  170.2,  $\delta$  152.3,  $\delta$  144.3,  $\delta$  142.6,  $\delta$  131.2,  $\delta$  130.1,  $\delta$  123.8,  $\delta$  120.8,  $\delta$  117.7,  $\delta$  112.4,  $\delta$  30.3. FTIR (ATR *corr.*  $\tilde{\nu}/\text{cm}^{-1}$ ):  $\tilde{\nu}$  2925.41 (w, C–H  $\text{sp}^2$  *str.*),  $\tilde{\nu}$  2303.92 (w, N $\equiv$ C *str.*),  $\tilde{\nu}$  2016.96 (s, A'(1) C $\equiv$ O *str.*),  $\tilde{\nu}$  1871.84 (s, A'(2) & A'' C $\equiv$ O *str.*). UV/Vis ( $\lambda/\text{nm}$ ,  $\epsilon/\text{L}\cdot\text{mol}^{-1}\cdot\text{cm}^{-1}$ ):  $\lambda$  437 ( $d\pi\rightarrow\pi^*$ ,  $\epsilon$  235.06),  $\lambda$  281 ( $\pi\rightarrow\pi^*$ ,  $\epsilon$  2340.84),  $\lambda$  237 ( $\pi\rightarrow\pi^*$ ,  $\epsilon$  3104.80). EA (%): *calc.* C 34.32, H 1.65, N 5.72. *found* C 34.89, H 1.54, N 5.60.

*Acetonitriletricarboxyl(2-fluoro-8-quinolinolate)rhenium(I)* (**Re2F8HQ**) Amber solid; MP: 134 °C (dec.), 14% yield. <sup>1</sup>H NMR (400 MHz, CD<sub>3</sub>CN,  $\delta/\text{ppm}$ ):  $\delta$  8.51 (dd,  $J^d=8.92$ , 7.04 Hz, 1H),  $\delta$  7.43 (t,  $J^t=7.96$  Hz, 1H),  $\delta$  7.33 (dd,  $J^d=8.92$ , 1.24 Hz, 1H),  $\delta$  7.06 (d,  $J^d=8.00$  Hz, 1H),  $\delta$  6.94 (d,  $J^d=7.92$  Hz, 1H). <sup>13</sup>C{<sup>1</sup>H} NMR (100 MHz, CD<sub>3</sub>CN,  $\delta/\text{ppm}$ ):  $\delta$  195.9<sub>C=O</sub>,  $\delta$  194.9<sub>C=O</sub>,  $\delta$  194.2<sub>C=O</sub>,  $\delta$  168.0 (d,  $J^d=2$  Hz),  $\delta$  161.5 (d,  $J^d=256$  Hz),  $\delta$  145.0 (d,  $J^d=2$  Hz),  $\delta$  139.7,  $\delta$  129.6 (d,  $J^d=2$  Hz),  $\delta$  128.6,  $\delta$  116.5,  $\delta$  111.5,  $\delta$  109.8 (d,  $J^d=33$  Hz). <sup>19</sup>F{<sup>1</sup>H} NMR (376 MHz, CD<sub>3</sub>CN,  $\delta/\text{ppm}$ ):  $\delta$  -56.94. FTIR (ATR *corr.*  $\tilde{\nu}/\text{cm}^{-1}$ ):  $\tilde{\nu}$  2925 (w, C–H  $\text{sp}^2$  *str.*),  $\tilde{\nu}$  2853 (w, C–H  $\text{sp}^2$  *str.*),  $\tilde{\nu}$  2322 (w, N $\equiv$ C *str.*),  $\tilde{\nu}$  2020 (s, A'(1) C $\equiv$ O *str.*),  $\tilde{\nu}$  1875 (s, A'(2) & A'' C $\equiv$ O *str.*).

*Acetonitriletricarboxyl(5-chloro-8-quinolinolate)rhenium(I)* (**Re5Cl8HQ**) Yellow solid, MP: 159–170 °C (dec.), 26% yield. <sup>1</sup>H NMR (400 MHz, CD<sub>3</sub>CN,  $\delta/\text{ppm}$ ):  $\delta$  9.98 (dd,  $J^d=4.84$ , 1.24 Hz, 1H),  $\delta$  8.64 (dd,  $J^d=8.64$ , 1.28 Hz, 1H),  $\delta$  7.64 (dd,  $J^d=8.64$ , 4.84 Hz, 1H),  $\delta$  7.55 (d,  $J^d=8.52$

Hz, 1H),  $\delta$  6.85 (d,  $J^d=8.52$  Hz, 1H),  $\delta$  1.96 (s, 3H).  $^{13}\text{C}\{^1\text{H}\}$  NMR (100 MHz,  $\text{CD}_3\text{CN}$ ,  $\delta/\text{ppm}$ ):  $\delta$  197.1 $_{\text{C}=\text{O}}$ ,  $\delta$  196.8 $_{\text{C}=\text{O}}$ ,  $\delta$  195.7 $_{\text{C}=\text{O}}$ ,  $\delta$  169.6,  $\delta$  151.0,  $\delta$  144.9,  $\delta$  136.5,  $\delta$  130.9,  $\delta$  128.9,  $\delta$  124.1,  $\delta$  115.4,  $\delta$  113.2. FTIR (ATR corr.  $\tilde{\nu}/\text{cm}^{-1}$ ):  $\tilde{\nu}$  2959 (w, C–H  $\text{sp}^2$  str.),  $\tilde{\nu}$  2911 (w, C–H  $\text{sp}^2$  str.),  $\tilde{\nu}$  2322 (w,  $\text{N}\equiv\text{C}$  str.),  $\tilde{\nu}$  2016 (s, A'(1)  $\text{C}\equiv\text{O}$  str.),  $\tilde{\nu}$  1874 (s, A'(2) & A''  $\text{C}\equiv\text{O}$  str.).

*Acetonitriletricarbonyl(5-nitro-8-quinolinolate)rhenium(I)* (**Re5NO<sub>2</sub>8HQ**) Yellow solid, MP: 190 - 194 °C (dec.), 26% yield.  $^1\text{H}$  NMR (400 MHz,  $\text{CD}_3\text{CN}$ ,  $\delta/\text{ppm}$ ):  $\delta$  9.57 (dd,  $J^d=9.00$ , 1.28 Hz, 1H),  $\delta$  9.03 (dd,  $J^d=4.84$ , 1.28 Hz, 1H),  $\delta$  8.63 (d,  $J^d=9.24$  Hz, 1H),  $\delta$  7.81 (dd,  $J^d=9.00$ , 4.84 Hz, 1H),  $\delta$  6.88 (d,  $J^d=9.24$  Hz, 1H).  $^{13}\text{C}\{^1\text{H}\}$  NMR (100 MHz,  $\text{CD}_3\text{CN}$ ,  $\delta/\text{ppm}$ ):  $\delta$  196.3 $_{\text{C}=\text{O}}$ ,  $\delta$  194.4 $_{\text{C}=\text{O}}$ ,  $\delta$  178.1 $_{\text{C}=\text{O}}$ ,  $\delta$  151.6,  $\delta$  143.3,  $\delta$  137.1,  $\delta$  132.9,  $\delta$  130.8,  $\delta$  127.0,  $\delta$  126.9,  $\delta$  121.4,  $\delta$  114.2. FTIR (ATR corr.  $\tilde{\nu}/\text{cm}^{-1}$ ):  $\tilde{\nu}$  2939 (w, C–H  $\text{sp}^2$  str.),  $\tilde{\nu}$  2918 (w, C–H  $\text{sp}^2$  str.),  $\tilde{\nu}$  2328 (w,  $\text{N}\equiv\text{C}$  str.),  $\tilde{\nu}$  2019 (s, A'(1)  $\text{C}\equiv\text{O}$  str.),  $\tilde{\nu}$  1900 (s, A'(2) & A''  $\text{C}\equiv\text{O}$  str.).

*Acetonitriletricarbonyl(5-fluoro-8-quinolinolate)rhenium(I)* (**Re5F8HQ**) Yellow solid, MP: 171-184 °C (dec.), 26% yield.  $^1\text{H}$  NMR (400 MHz,  $\text{CD}_3\text{CN}$ ,  $\delta/\text{ppm}$ ):  $\delta$  8.97 (dd,  $J^d=4.84$ , 1.08 Hz, 1H),  $\delta$  8.55 (dd,  $J^d=8.56$ , 1.12 Hz, 1H),  $\delta$  7.58 (dd,  $J^d=8.56$ , 4.84 Hz, 1H),  $\delta$  7.26 (q,  $J^q=10.52$ , 8.72 Hz, 1H),  $\delta$  6.78 (dd,  $J^d=4.40$ , 8.72 Hz, 1H).  $^{13}\text{C}\{^1\text{H}\}$  NMR (100 MHz,  $\text{CD}_3\text{CN}$ ,  $\delta/\text{ppm}$ ):  $\delta$  197.3 $_{\text{C}=\text{O}}$ ,  $\delta$  196.9 $_{\text{C}=\text{O}}$ ,  $\delta$  196.0 $_{\text{C}=\text{O}}$ ,  $\delta$  166.4 (d,  $J^d=2$  Hz),  $\delta$  151.3,  $\delta$  147.1 (d,  $J^d=235$  Hz),  $\delta$  143.0 (d,  $J^d=5$  Hz),  $\delta$  133.1 (d,  $J^d=3$  Hz),  $\delta$  123.3 (d,  $J^d=2$  Hz),  $\delta$  121.1 (d,  $J^d=21$  Hz),  $\delta$  144.5 (d,  $J^d=20$  Hz),  $\delta$  113.0 (d,  $J^d=7$  Hz).  $^{19}\text{F}\{^1\text{H}\}$  NMR (376 MHz,  $\text{CD}_3\text{CN}$ ,  $\delta/\text{ppm}$ ):  $\delta$  -144.8. FTIR (ATR corr.  $\tilde{\nu}/\text{cm}^{-1}$ ):  $\tilde{\nu}$  2954 (w, C–H  $\text{sp}^2$  str.),  $\tilde{\nu}$  2909 (w, C–H  $\text{sp}^2$  str.),  $\tilde{\nu}$  2298 (w,  $\text{N}\equiv\text{C}$  str.),  $\tilde{\nu}$  2019 (s, A'(1)  $\text{C}\equiv\text{O}$  str.),  $\tilde{\nu}$  1892 (s, A'(2) & A''  $\text{C}\equiv\text{O}$  str.).

*Tricarbonylchloro(5-fluoro-1,10-phenanthroline)rhenium(I)* (**Re5FPhen**) Yellow solid, MP: 322 °C (dec.), 26% yield.  $^1\text{H}$  NMR (400 MHz,  $\text{DMSO-d}_6$ ,  $\delta/\text{ppm}$ ):  $\delta$  9.54 (dd,  $J^d=1.28$ , 5.12 Hz, 1H),  $\delta$  9.42 (dd,  $J^d=1.20$ , 5.08 Hz, 1H),  $\delta$  9.04 (dd,  $J^d=1.28$ , 8.40 Hz, 1H),  $\delta$  8.93 (dd,  $J^d=1.28$ , 8.40 Hz, 1H),  $\delta$  8.29 (d,  $J^d=10.44$  Hz, 1H),  $\delta$  8.20 (dd,  $J^d=5.12$ , 8.40 Hz, 1H),  $\delta$  8.11 (dd,  $J^d=5.08$ ,

8.32 Hz, 1H).  $^{13}\text{C}\{^1\text{H}\}$  NMR (100 MHz, DMSO- $d_6$ ,  $\delta/ppm$ ):  $\delta$  197.4 $_{\text{C=O}}$ ,  $\delta$  197.3 $_{\text{C=O}}$ ,  $\delta$  189.6 $_{\text{C=O}}$ ,  $\delta$  156.8,  $\delta$  154.5,  $\delta$  154.3,  $\delta$  152.9 (d,  $J^d=2$  Hz),  $\delta$  146.5 (d,  $J^d=7$  Hz),  $\delta$  143.6,  $\delta$  139.1 (d,  $J^d=5$  Hz),  $\delta$  133.0 (d,  $J^d=4$  Hz),  $\delta$  129.6 (d,  $J^d=4$  Hz),  $\delta$  126.9 (d,  $J^d=3$  Hz),  $\delta$  122.8 (d,  $J^d=23$  Hz),  $\delta$  109.3 (d,  $J^d=22$  Hz).  $^{19}\text{F}\{^1\text{H}\}$  NMR (376 MHz,  $\text{CD}_3\text{CN}$ ,  $\delta/ppm$ ):  $\delta$  -120.8.

*Tricarbonylchloro(5-chloro-1,10-phenanthroline)rhenium(I)* (**Re5ClPhen**) Yellow solid, MP: 319 °C (dec.), 92% yield.  $^1\text{H}$  NMR (400 MHz, DMSO- $d_6$ ,  $\delta/ppm$ ):  $\delta$  9.54 (d,  $J^d=4.96$  Hz, 1H),  $\delta$  9.44 (d,  $J^d=4.68$  Hz, 1H),  $\delta$  9.10 (d,  $J^d=8.80$  Hz, 1H),  $\delta$  8.92 (d,  $J^d=7.92$  Hz, 1H),  $\delta$  8.23 (*app. t*,  $J^t=7.48$  Hz, 1H),  $\delta$  8.13 (*app. t*,  $J^t=7.52$  Hz, 1H).  $^{13}\text{C}\{^1\text{H}\}$  NMR (100 MHz, DMSO- $d_6$ ,  $\delta/ppm$ ):  $\delta$  197.5 $_{\text{C=O}}$ ,  $\delta$  197.4 $_{\text{C=O}}$ ,  $\delta$  189.6 $_{\text{C=O}}$ ,  $\delta$  154.4,  $\delta$  153.9,  $\delta$  146.7,  $\delta$  145.1,  $\delta$  138.8,  $\delta$  136.1,  $\delta$  130.2,  $\delta$  129.8,  $\delta$  128.5,  $\delta$  127.4,  $\delta$  127.2,  $\delta$  127.0.

*Tricarbonylchloro(5-Nitro-1,10-phenanthroline)rhenium(I)* (**Re5NO<sub>2</sub>Phen**) Yellow solid, MP: 326 °C (dec.), 93% yield.  $^1\text{H}$  NMR (400 MHz, DMSO- $d_6$ ,  $\delta/ppm$ ):  $\delta$  9.57 (dd,  $J^d=9.28$ , 5.16 Hz, 2H),  $\delta$  9.39 (s, 1H),  $\delta$  9.31 (d,  $J^d=8.64$  Hz, 1H),  $\delta$  9.19 (d,  $J^d=8.20$  Hz, 1H),  $\delta$  8.23 (m, 2H).  $^{13}\text{C}\{^1\text{H}\}$  NMR (100 MHz, DMSO- $d_6$ ,  $\delta/ppm$ ):  $\delta$  197.9 $_{\text{C=O}}$ ,  $\delta$  197.8 $_{\text{C=O}}$ ,  $\delta$  190.0 $_{\text{C=O}}$ ,  $\delta$  156.9,  $\delta$  155.2,  $\delta$  147.9,  $\delta$  146.8,  $\delta$  144.7,  $\delta$  142.0,  $\delta$  136.6,  $\delta$  128.1,  $\delta$  128.1,  $\delta$  128.1,  $\delta$  127.6,  $\delta$  123.7.

## S.4 Radiochemical Yield vs Reaction Temperature Plots

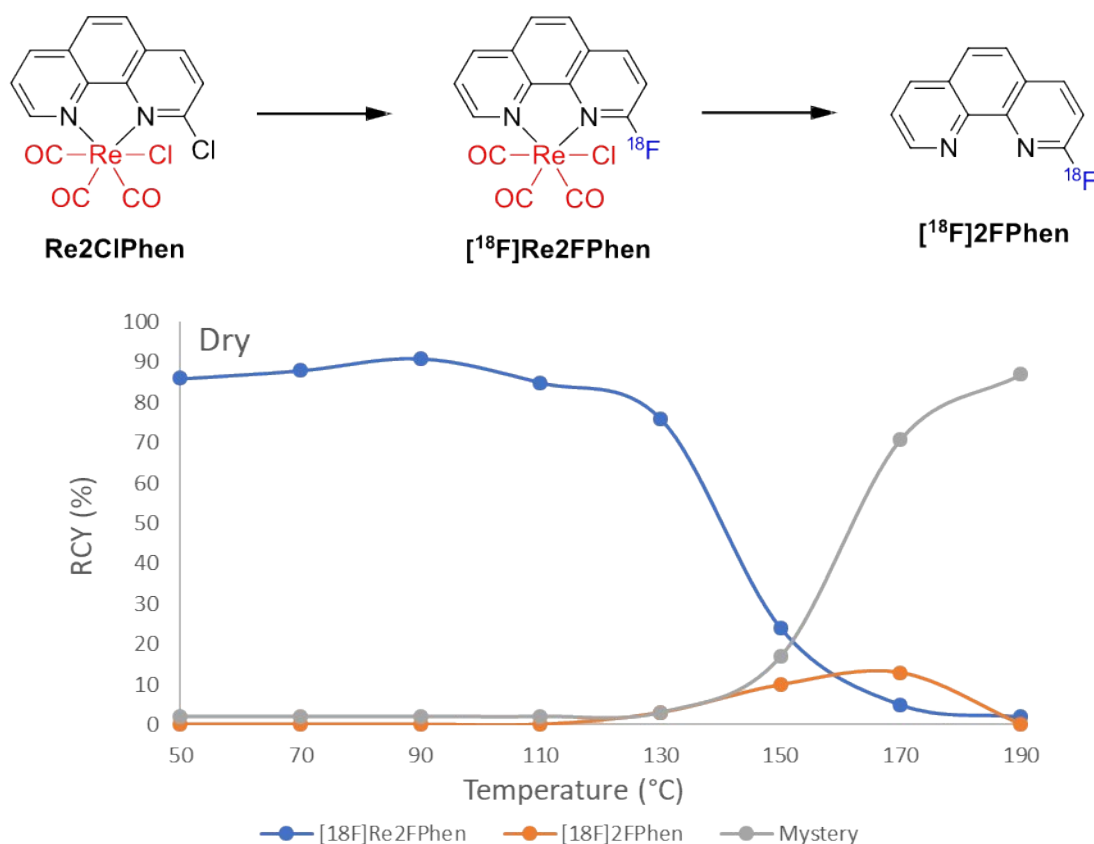


Figure S62. RCY of the [<sup>18</sup>F]Re<sub>2</sub>FPhen complex (blue), the decomplexed [<sup>18</sup>F]2FPhen ligand (orange) and the unknown by-product (grey) resulting from the radiofluorination of the **Re<sub>2</sub>ClPhen** precursor as a function of the reaction temperature under dry reaction conditions. All other variables were constant (47 s reaction time, 29±10 MBq activity, 0.08 μmol of precursor, DMSO solvent).

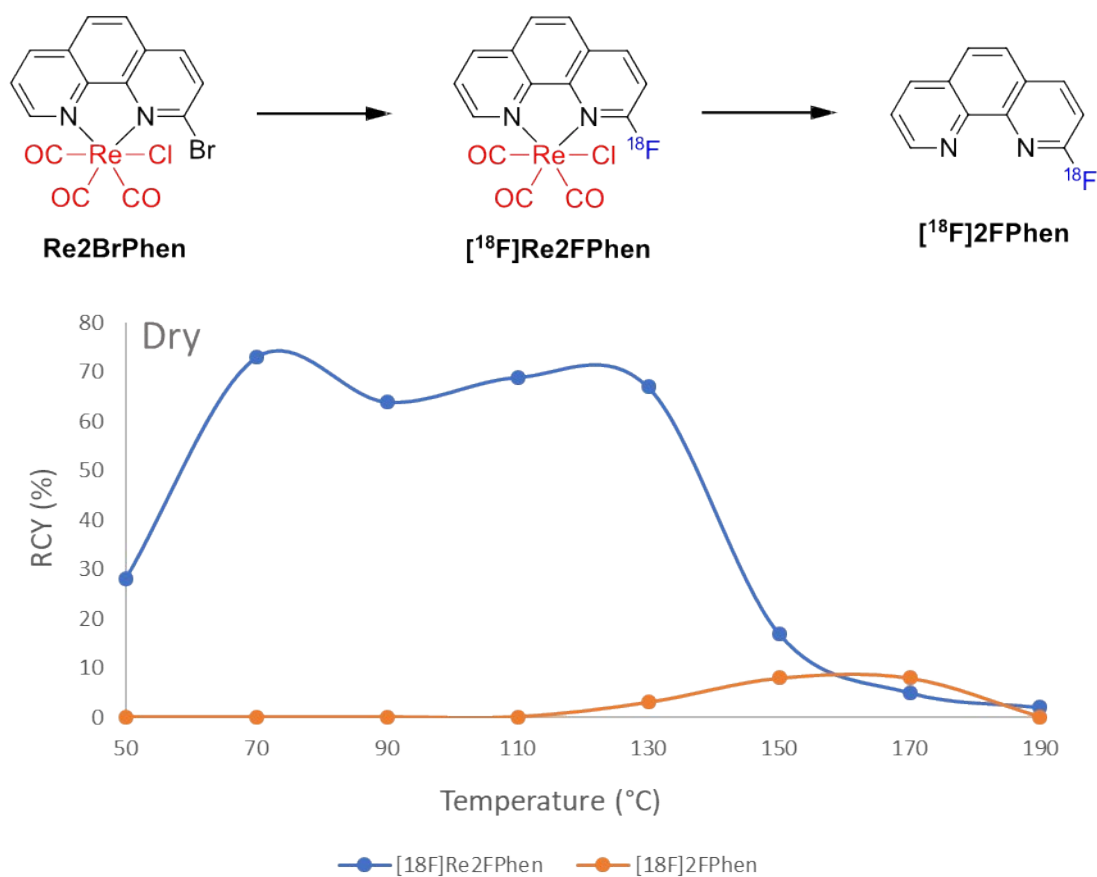


Figure S63. RCY of the [<sup>18</sup>F]Re2FPhen complex (blue), the decomplexed [<sup>18</sup>F]2FPhen ligand (orange) and the unknown by-product (grey) resulting from the radiofluorination of the **Re2BrPhen** precursor as a function of the reaction temperature under dry reaction conditions. All other variables were constant (47 s reaction time, 29±10 MBq activity, 0.08 μmol of precursor, DMSO solvent).

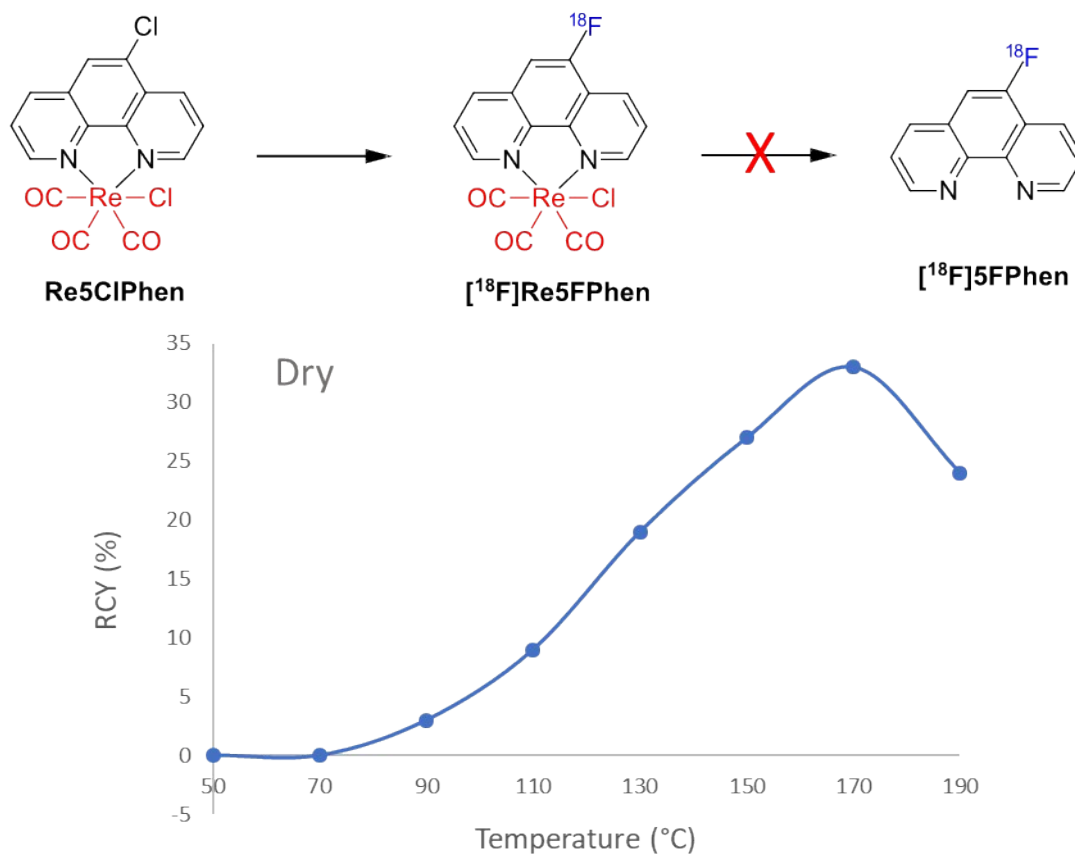


Figure S64. RCY of the [<sup>18</sup>F]Re5FPhen complex (blue) resulting from the radiofluorination of the **Re5ClPhen** precursor as a function of the reaction temperature under dry reaction conditions. All other variables were constant (47 s reaction time, 29±10 MBq activity, 0.08 μmol of precursor, DMSO solvent). The decomplexed [<sup>18</sup>F]5FPhen ligand was not observed from these reactions.

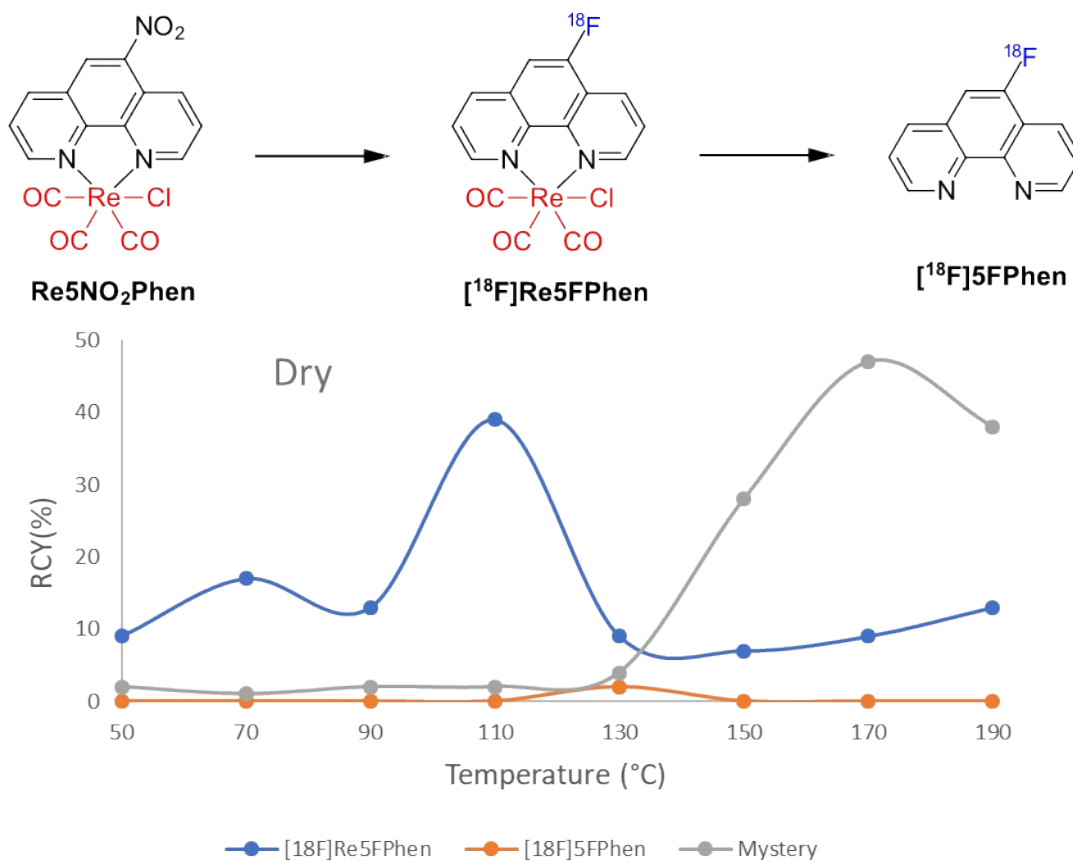


Figure S65. RCY of the [<sup>18</sup>F]Re5FPhen complex (blue), the decomplexed [<sup>18</sup>F]5FPhen ligand (orange) and the unknown by-product (grey) resulting from the radiofluorination of the **Re5NO<sub>2</sub>Phen** precursor as a function of the reaction temperature under dry reaction conditions. All other variables were constant (47 s reaction time, 29±10 MBq activity, 0.08 μmol of precursor, DMSO solvent).

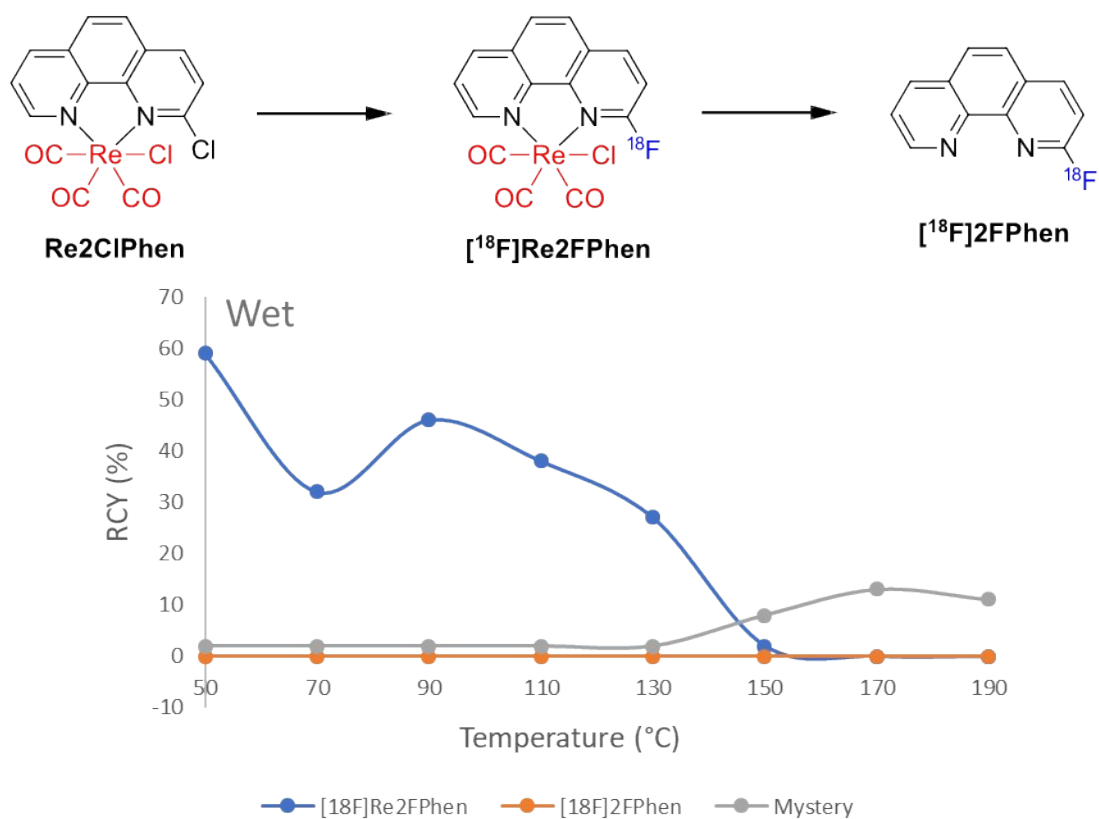


Figure S66. RCY of the [<sup>18</sup>F]Re2FPhen complex (blue), the decomplexed [<sup>18</sup>F]2FPhen ligand (orange) and the unknown by-product (grey) resulting from the radiofluorination of the **Re2ClPhen** precursor as a function of the reaction temperature under wet reaction conditions. All other variables were constant (47 s reaction time, 29±10 MBq activity, 0.08 μmol of precursor, DMSO solvent).

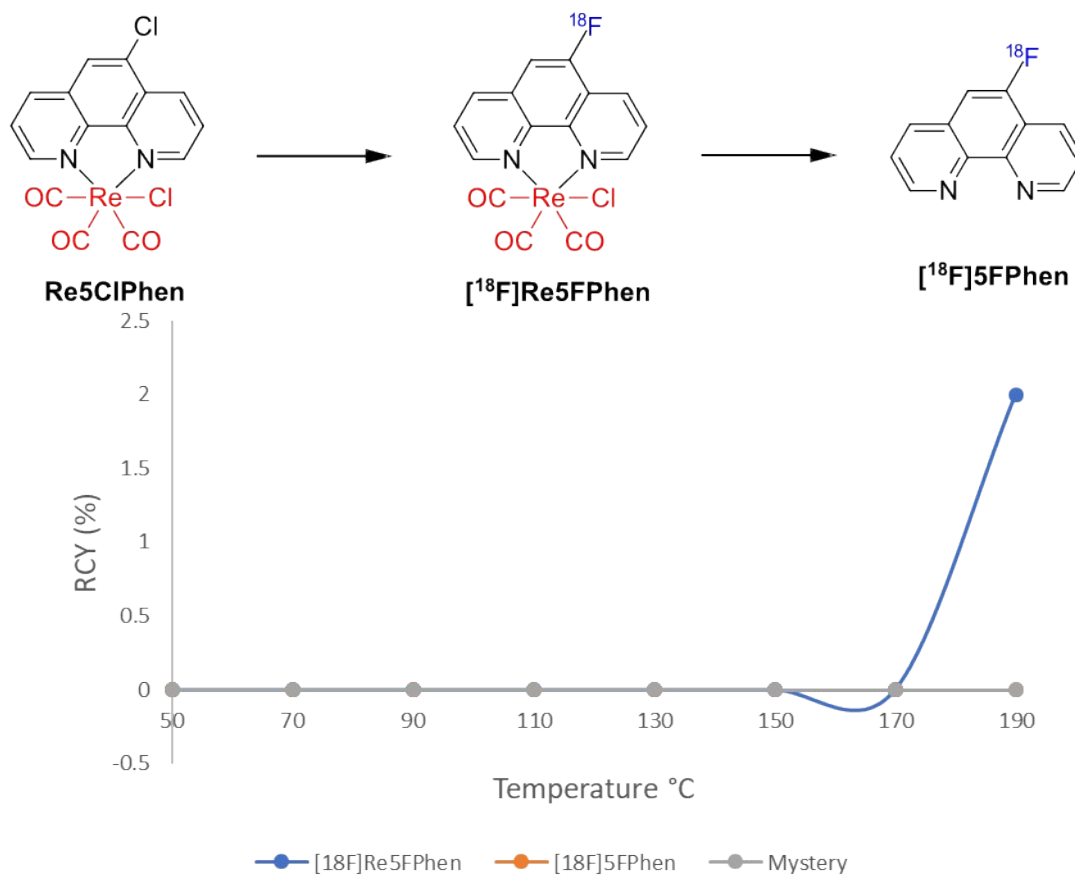


Figure 67. RCY of the **[<sup>18</sup>F]Re5FPhen** complex (blue), resulting from the radiofluorination of the **Re5ClPhen** precursor as a function of the reaction temperature under wet reaction conditions. All other variables were constant (47 s reaction time, 29±10 MBq activity, 0.08 μmol of precursor, DMSO solvent). The decomplexed **[<sup>18</sup>F]5FPhen** ligand was not observed from these reactions.

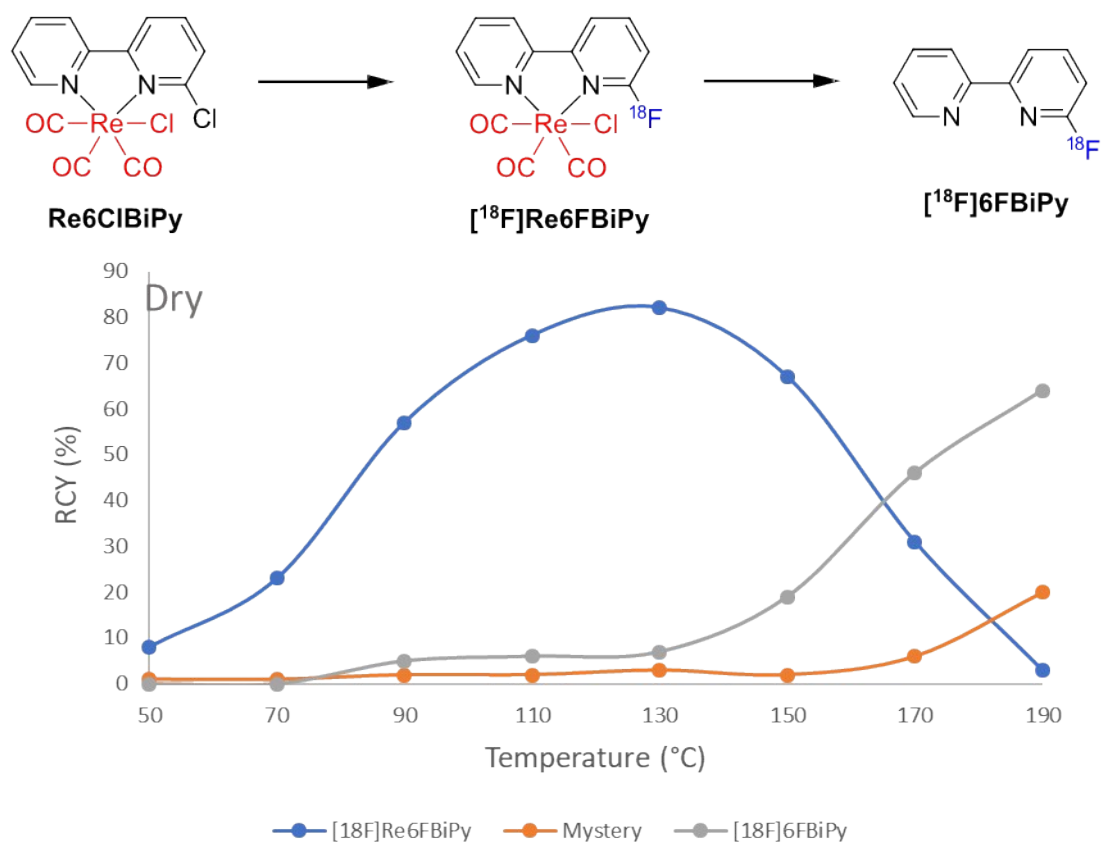


Figure S68. RCY of the [<sup>18</sup>F]Re6FBiPy complex (blue), the decomplexed [<sup>18</sup>F]6FBiPy ligand (orange) and the unknown by-product (grey) resulting from the radiofluorination of the Re6ClBiPy precursor as a function of the reaction temperature under dry reaction conditions. All other variables were constant (47 s reaction time, 29±10 MBq activity, 0.08 μmol of precursor, DMSO solvent).

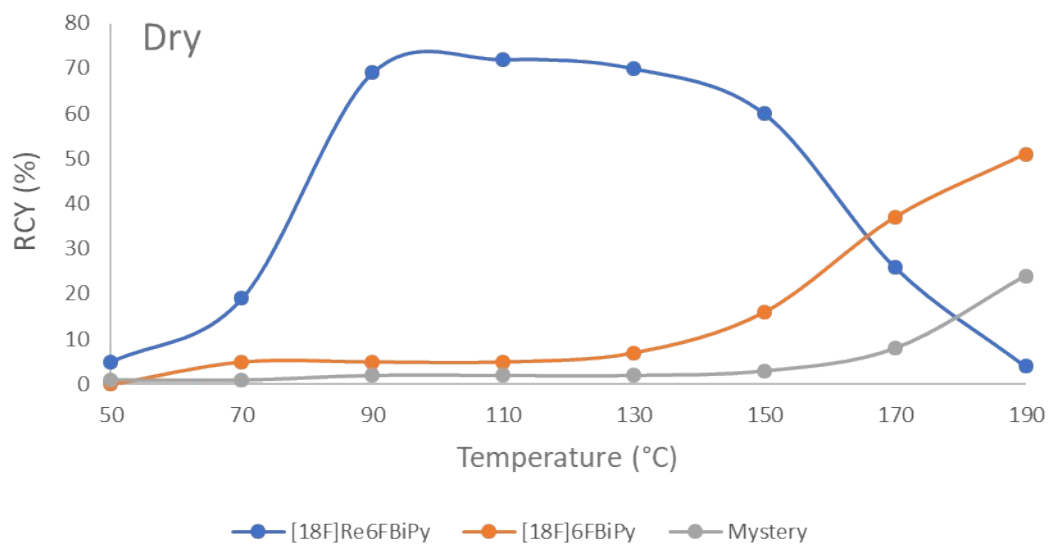
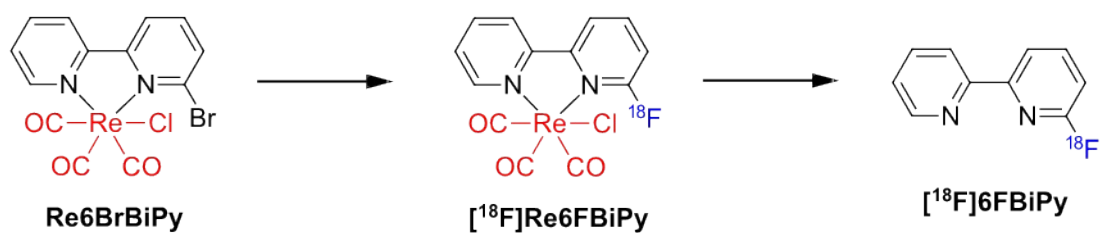


Figure S69. RCY of the [<sup>18</sup>F]Re6FBiPy complex (blue), the decomplexed [<sup>18</sup>F]6FBiPy ligand (orange) and the unknown by-product (grey) resulting from the radiofluorination of the Re6BrBiPy precursor as a function of the reaction temperature under dry reaction conditions. All other variables were constant (47 s reaction time, 29±10 MBq activity, 0.08 μmol of precursor, DMSO solvent).

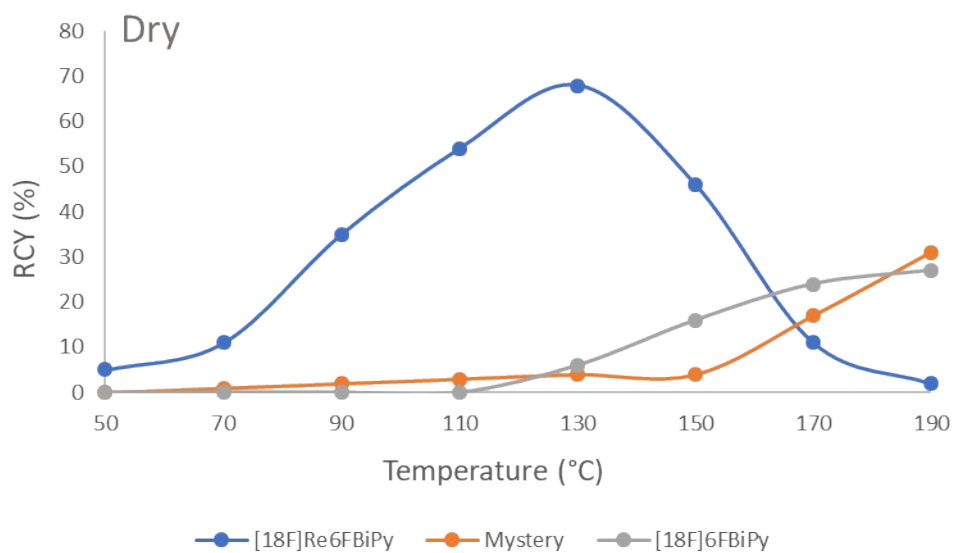
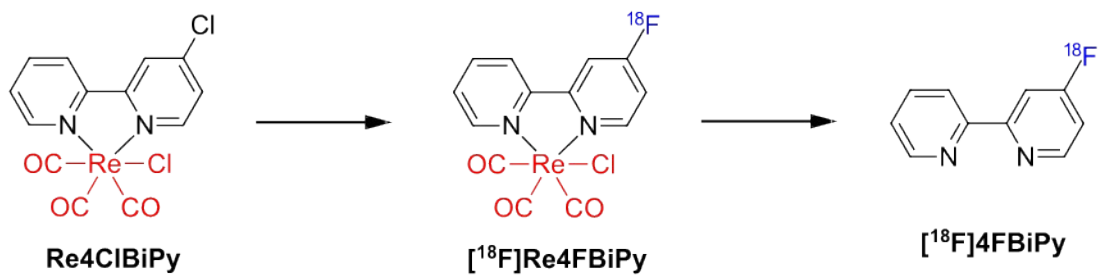


Figure S70. RCY of the [<sup>18</sup>F]Re4FBiPy complex (blue), the decomplexed [<sup>18</sup>F]4FBiPy ligand (orange) and the unknown by-product (grey) resulting from the radiofluorination of the **Re4ClBiPy** precursor as a function of the reaction temperature under dry reaction conditions. All other variables were constant (47 s reaction time, 29±10 MBq activity, 0.08 μmol of precursor, DMSO solvent).

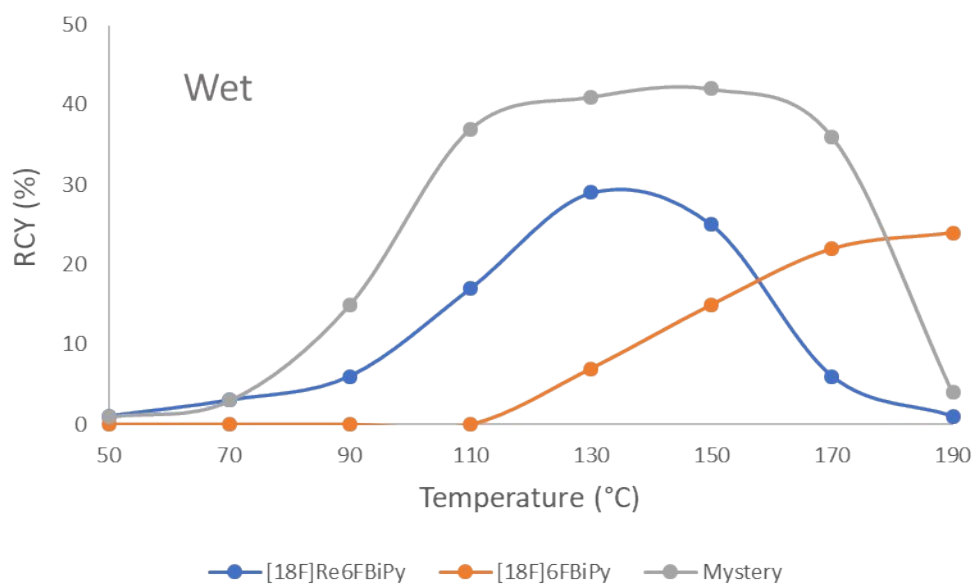
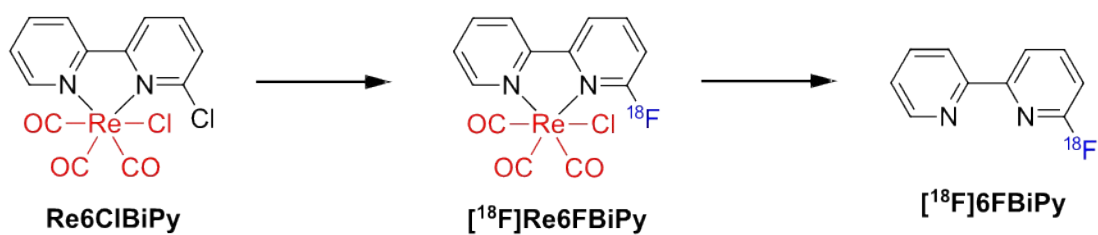


Figure S71. RCY of the [<sup>18</sup>F]Re6FBiPy complex (blue), the decomplexed [<sup>18</sup>F]6FBiPy ligand (orange) and the unknown by-product (grey) resulting from the radiofluorination of the Re6ClBiPy precursor as a function of the reaction temperature under wet reaction conditions. All other variables were constant (47 s reaction time, 29±10 MBq activity, 0.08 μmol of precursor, DMSO solvent).

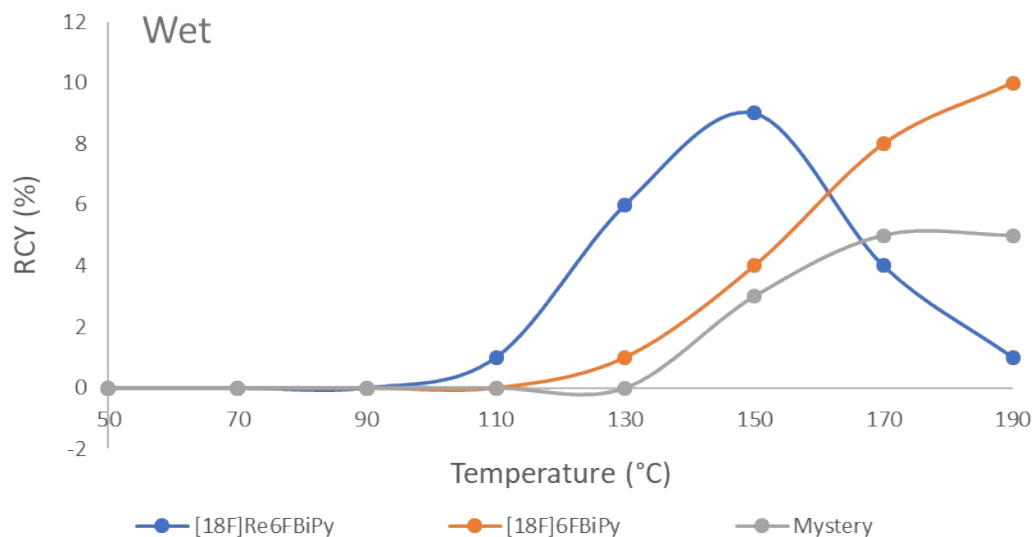
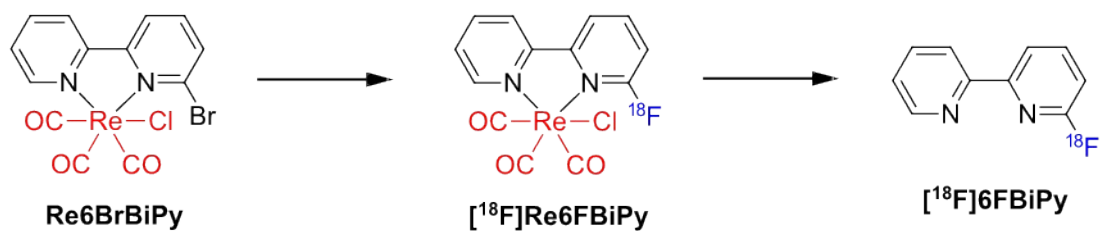


Figure S72. RCY of the [<sup>18</sup>F]Re6FBiPy complex (blue), the decomplexed [<sup>18</sup>F]6FBiPy ligand (orange) and the unknown by-product (grey) resulting from the radiofluorination of the **Re6BrBiPy** precursor as a function of the reaction temperature under wet reaction conditions. All other variables were constant (47 s reaction time, 29±10 MBq activity, 0.08 μmol of precursor, DMSO solvent).

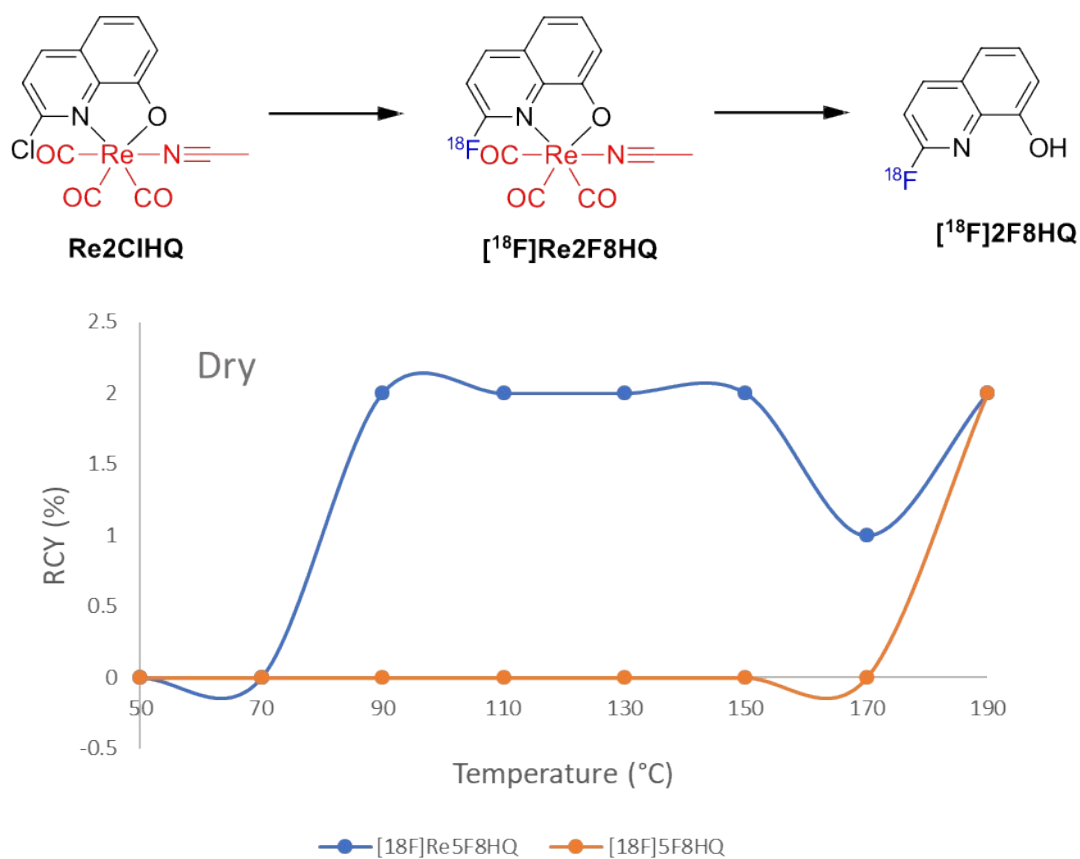


Figure S73. RCY of the [<sup>18</sup>F]Re<sub>2</sub>Cl<sub>8</sub>HQ complex (blue) and the decomplexed [<sup>18</sup>F]2F<sub>8</sub>HQ ligand (orange) resulting from the radiofluorination of the **Re<sub>2</sub>Cl<sub>8</sub>HQ** precursor as a function of the reaction temperature under dry reaction conditions. All other variables were constant (47 s reaction time, 29±10 MBq activity, 0.08 μmol of precursor, DMSO solvent). No by-product was observed in this reaction.

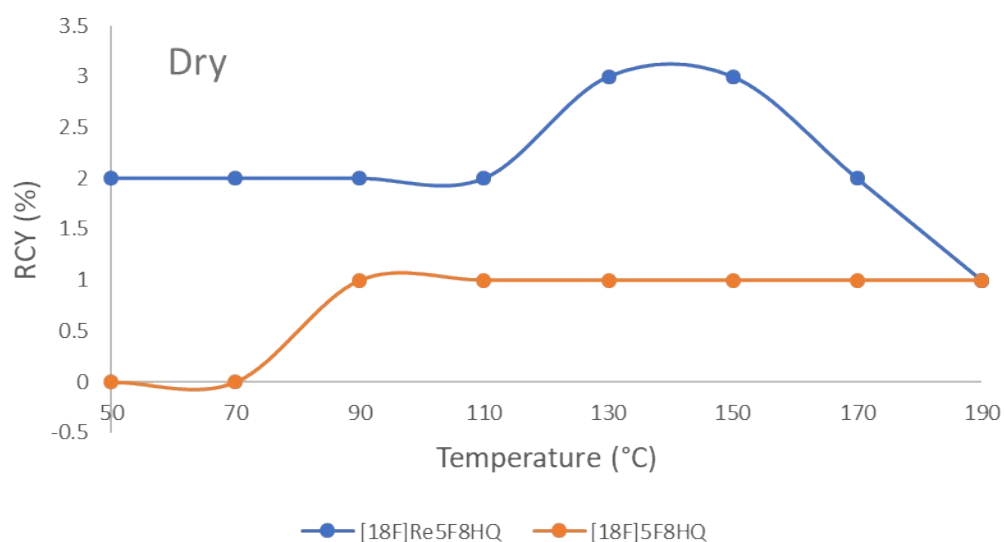
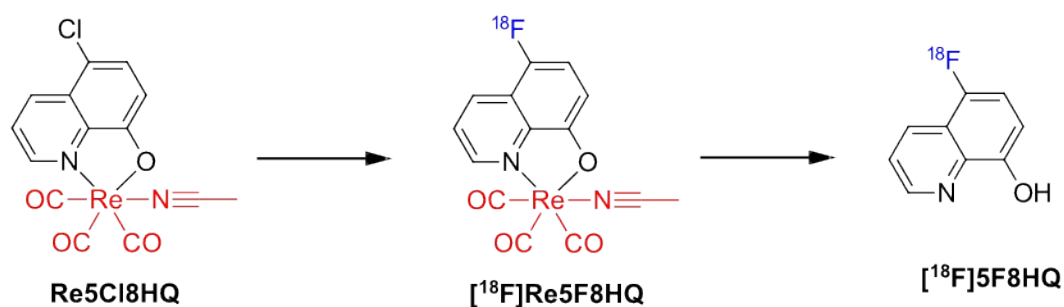


Figure S74. RCY of the [<sup>18</sup>F]Re5F8HQ complex (blue) and the decomplexed [<sup>18</sup>F]5F8HQ ligand (orange) resulting from the radiofluorination of the Re5Cl8HQ precursor as a function of the reaction temperature under dry reaction conditions. All other variables were constant (47 s reaction time, 29±10 MBq activity, 0.08 μmol of precursor, DMSO solvent). No by-product was observed in this reaction.

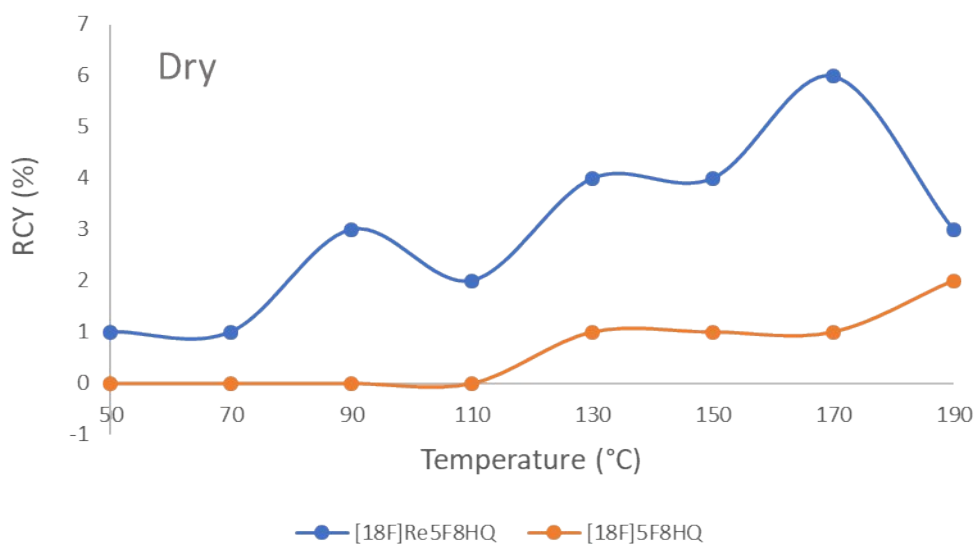
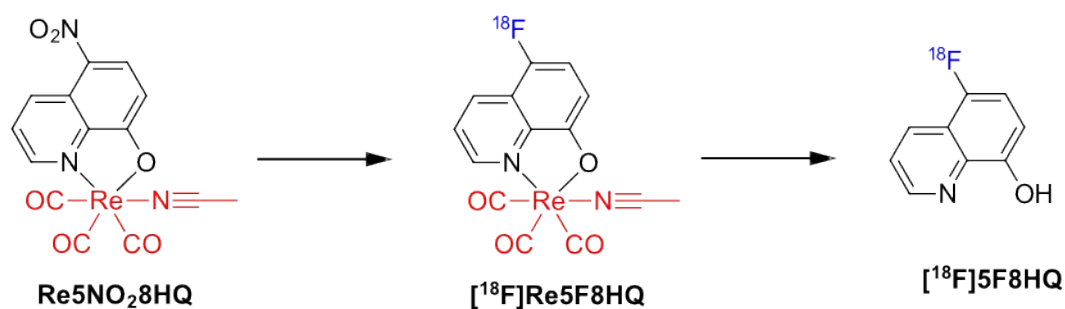


Figure S75. RCY of the [<sup>18</sup>F]Re5F8HQ complex (blue) and the decomplexed [<sup>18</sup>F]5F8HQ ligand (orange) resulting from the radiofluorination of the Re5NO<sub>2</sub>8HQ precursor as a function of the reaction temperature under dry reaction conditions. All other variables were constant (47 s reaction time, 29±10 MBq activity, 0.08 μmol of precursor, DMSO solvent). No by-product was observed in this reaction.

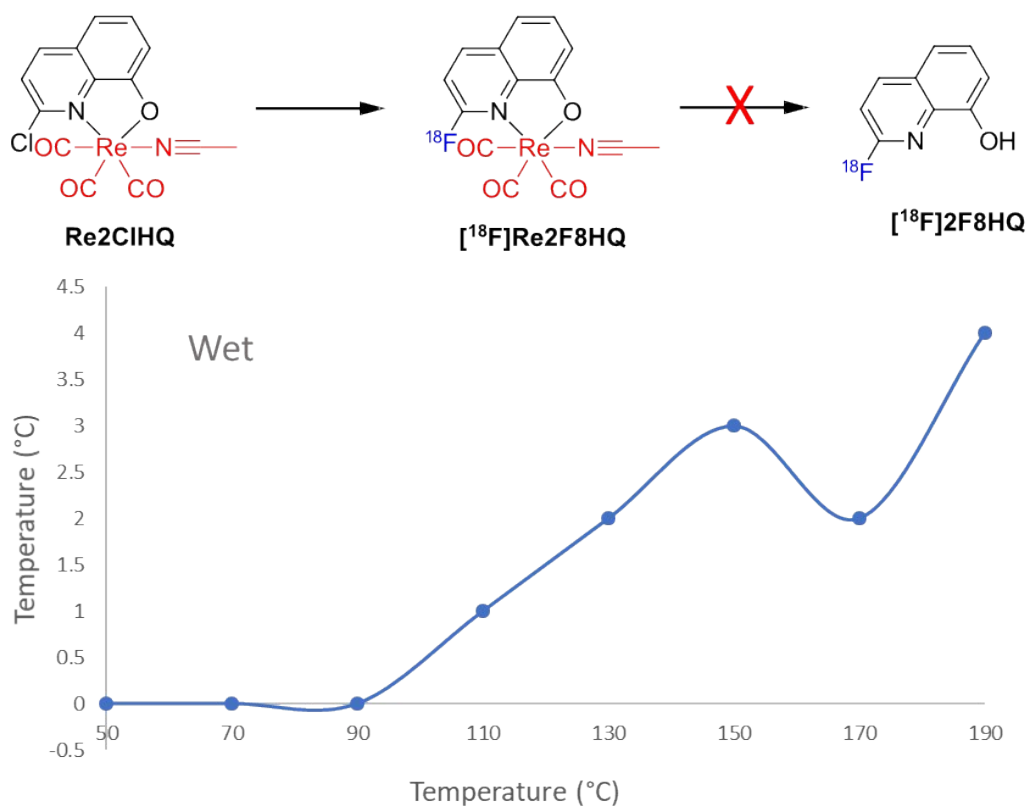


Figure S76. RCY of the [<sup>18</sup>F]Re<sub>2</sub>F<sub>8</sub>HQ complex (blue) resulting from the radiofluorination of the Re<sub>2</sub>Cl<sub>8</sub>HQ precursor as a function of the reaction temperature under wet reaction conditions. All other variables were constant (47 s reaction time, 29±10 MBq activity, 0.08 μmol of precursor, DMSO solvent). No by-product nor [<sup>18</sup>F]2F<sub>8</sub>HQ ([<sup>18</sup>F]CABS13) radioproduct was observed in this reaction.

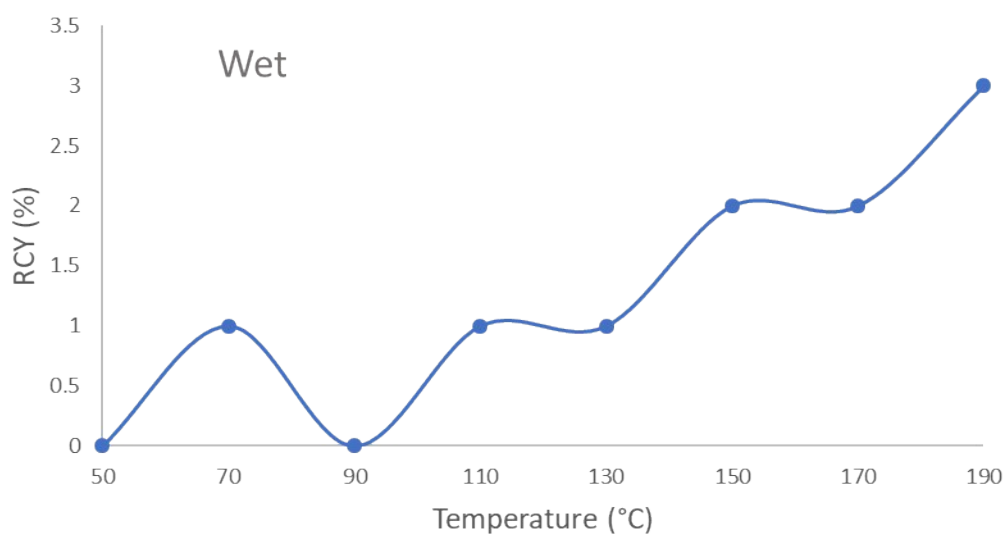
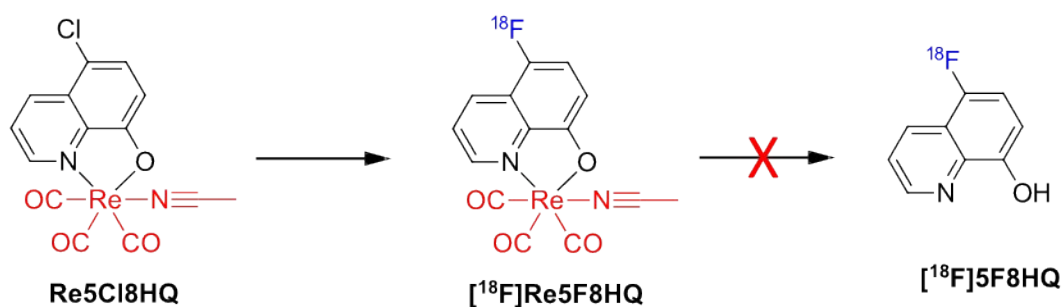


Figure S77. RCY of the [<sup>18</sup>F]Re5F8HQ complex (blue) resulting from the radiofluorination of the Re5Cl8HQ precursor as a function of the reaction temperature under wet reaction conditions. All other variables were constant (47 s reaction time, 29±10 MBq activity, 0.08 μmol of precursor, DMSO solvent). No by-product nor [<sup>18</sup>F]5F8HQ radioproduct was observed in this reaction.

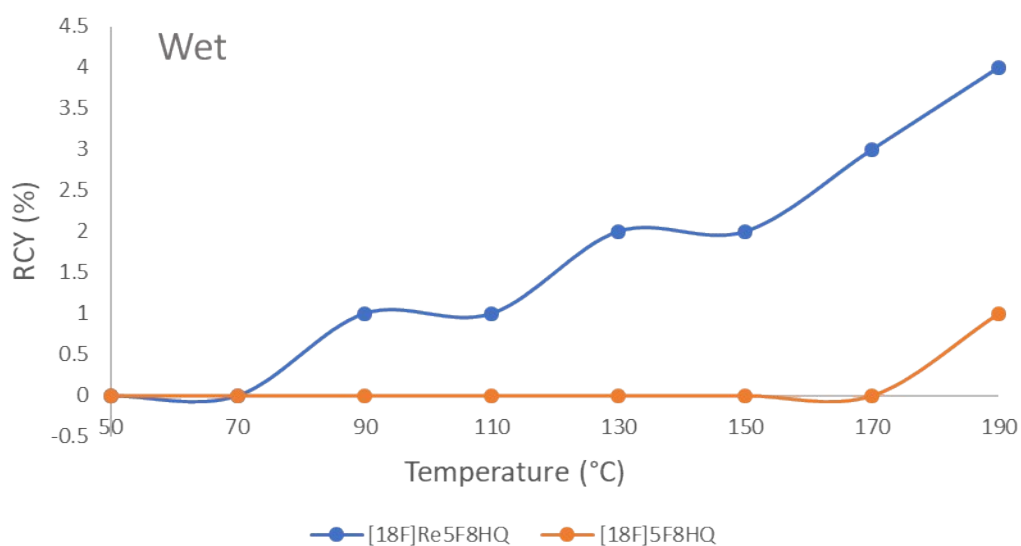
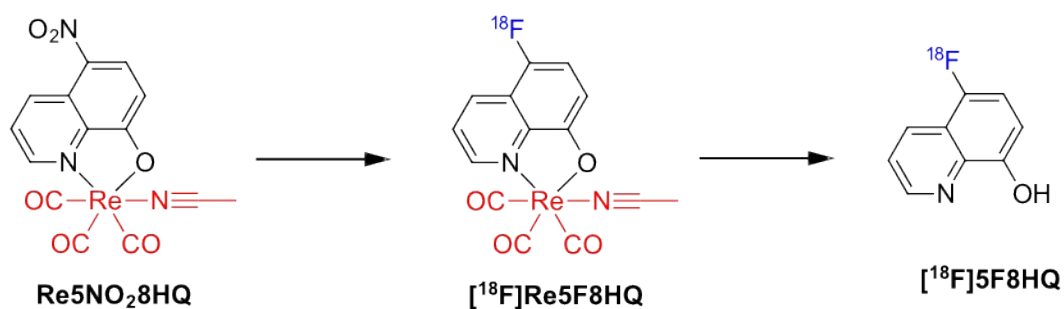


Figure S78. RCY of the [<sup>18</sup>F]Re5F8HQ complex (blue) and the decomplexed [<sup>18</sup>F]5F8HQ ligand (orange) resulting from the radiofluorination of the Re5NO<sub>2</sub>8HQ precursor as a function of the reaction temperature under wet reaction conditions. All other variables were constant (47 s reaction time, 29±10 MBq activity, 0.08 μmol of precursor, DMSO solvent). No by-product was observed in this reaction.

## S.5 Computational Details of the Reaction Mechanism

The geometry optimizations and bond analyses were computed using ORCA software<sup>1</sup> at the DFT level using def2-TZVP basis sets, B97<sup>2</sup> functional corrected using the Grimme D3 correction with Becke–Johnson damping<sup>3</sup> to the DFT energy. The resolution of identity (RI) approximation<sup>4</sup> and the Effective Core potential LANL2DZ<sup>5,6</sup> were also applied. All of the structures were confirmed to be local energy minima (no imaginary frequencies) except the transition states (one imaginary frequency). Thermodynamic properties were computed at the def2-TZVP/B97-D3 level of theory and calculated at 298 K. Zero-point energy corrections are included. The solvent (DMSO) has been taken into account through the Continuum Polarizable Medium model.<sup>7</sup>

NBO analyses were performed using the NBO6 suite of programs.<sup>8</sup>

The bond analysis between the rhenium and the N,N ligand has been carried out combining the Natural Orbitals for Chemical Valence<sup>9</sup> and Charge Displacement<sup>10</sup> frameworks (NOCV-CD<sup>11,12</sup>). Within the NOCV framework, the interaction between two fragments (in our case A, [ReCl(CO)<sub>3</sub>] and B, the N,N ligand) is analyzed comparing the wavefunction of the adduct AB ( $\psi^{(AB)}$ ), with the antisymmetrized (and re-normalized) product of the wavefunctions of the isolated fragments (the so-called “promolecule”,  $\psi^0$ ). In particular, the charge rearrangement upon the formation of the interaction between A and B is defined as

$$\Delta\rho = \sum_i |\psi_i^{(AB)}|^2 - \sum_i |\psi_i^0|^2$$

and separated in diagonal contributions through the “valence operator” (V),<sup>13–15</sup> producing pairs of complementary orbitals ( $\varphi_k, \varphi_{-k}$ ), corresponding to eigenvalues with the same absolute value but opposite sign ( $\pm v_k$ ). Accordingly,  $\Delta\rho$  can be expressed in terms of NOCV pairs:

$$\Delta\rho = \sum_k v_k (|\varphi_k|^2 - |\varphi_{-k}|^2) = \sum_k \Delta\rho_k$$

The visual inspection of each  $\Delta\rho_k$  contribution is useful to assign the bond component to which  $\Delta\rho_k$  is related. For more quantitative results, the different  $\Delta\rho_k$  can be also integrated along an axis ( $z$ ) in order to quantify the fraction of electrons ( $\Delta q$ ) involved in the  $\varphi_{-k} \rightarrow \varphi_k$  transition and, therefore, in the bond component, throughout the whole molecule.

$$\Delta q_k = \int_{-\infty}^{z'} dz \iint_{-\infty}^{\infty} \Delta \rho_k dx dy$$

In the case of interest, since the ligand is bidentate, the chosen axis crosses the metal nucleus and the middle point between the two nitrogen atoms. Choosing a plausible inter-fragment boundary, the bond component can be defined with a single value,  $CT_k$ .

### Bond analysis.

In the case of **Re6ClBiPy** the electronic rearrangements  $\Delta\rho_k$  associated with NOCV pairs with  $k < 5$  are of particular interest for the bond analysis (Figure S). With  $k \geq 5$ , the NOCV pair generally describes a polarization of the fragments with negligible contribution to the M-L bond components.

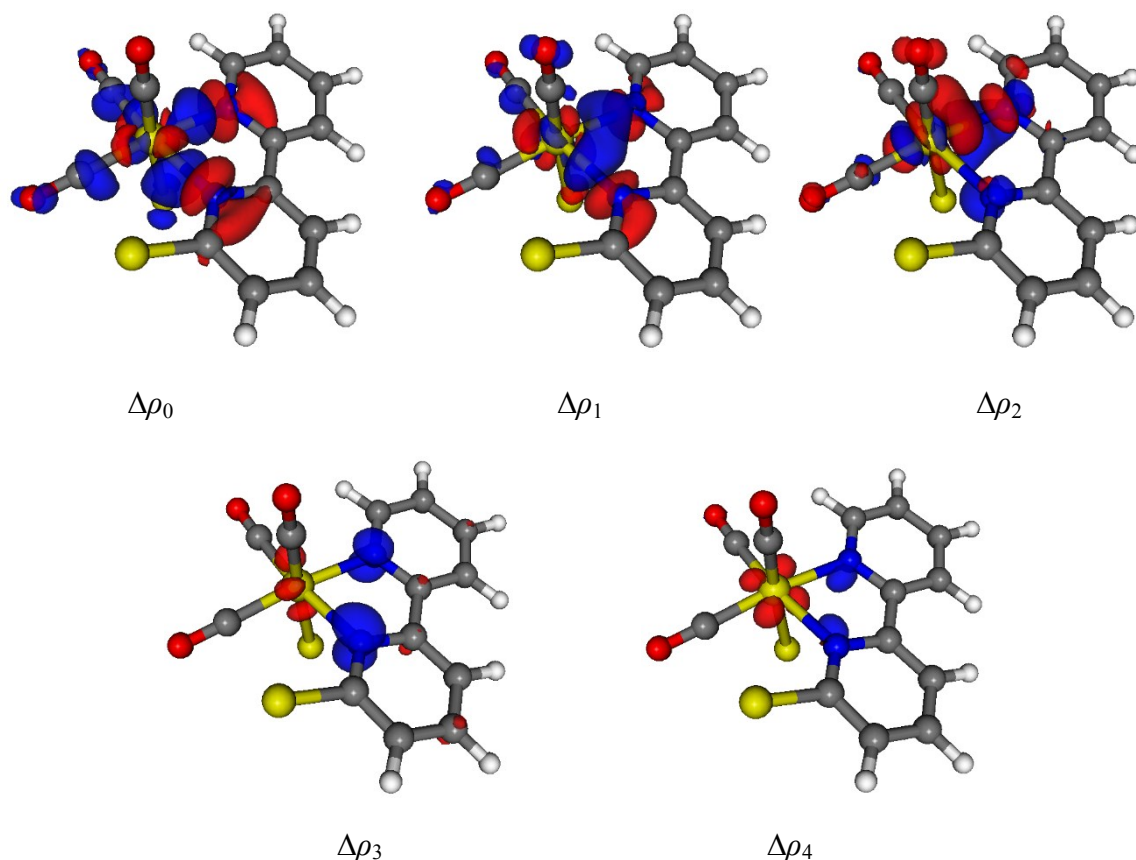


Figure S79. Isodensity surfaces ( $\pm 0.002$  e/au) for  $\Delta\rho_k$  ( $k = 0 - 3$ ) superimposed to the molecular structure of **Re6ClBiPy**. The direction of the charge flow is red  $\rightarrow$  blue.

In  $\Delta\rho_0$  and  $\Delta\rho_2$ , large depletion regions are located in correspondence of the nitrogen atoms of the ligand, whereas accumulation regions can be found around the metal and the carbonyl moieties in *trans* position with respect to the nitrogen atoms. Such contributions are clearly related to the  $\sigma$  donation from the bipyridine to the metallic fragment ( $M \leftarrow L$ ). Notably, also the carbon bound to the chlorine is particularly affected by the coordination of the ligand on the metal, showing a depletion region.

In  $\Delta\rho_1$ ,  $\Delta\rho_3$  and  $\Delta\rho_4$ , accumulation regions are located on the nitrogen atoms and depletion regions can be found on the metal, with a shape that resembles the *d* orbitals of the metal. These components are clearly associated with the  $\pi M \rightarrow L$  back-donation.

In order to see which contribution prevails, the  $\Delta\rho_k$  functions can be integrated along the *z* axis (which connects the metal and the median point between the two nitrogen atoms, Figure S). In particular,  $\Delta q_0$  and  $\Delta q_2$  (the integrated functions of  $\Delta\rho_0$  and  $\Delta\rho_2$ ) are always positive, indication of a flux from right to left in Figure S, which starts from the ligand, reaches a maximum in the inter-fragment region and decays reaching the carbonyl moieties. At the boundary,  $CT_0$  and  $CT_2$  are 0.188 and 0.078 e, respectively. Conversely,  $\Delta q_1$ ,  $\Delta q_3$  and  $\Delta q_4$  are negative in the inter-fragment region (left  $\rightarrow$  right flux, from the metal to the ligand).  $\Delta q_3$  becomes positive in correspondence of the nitrogen atoms, indicating an additional strong polarization contribution. At the boundary, the back-donation can be quantified as -0.065, -0.034 and -0.017 e, respectively.

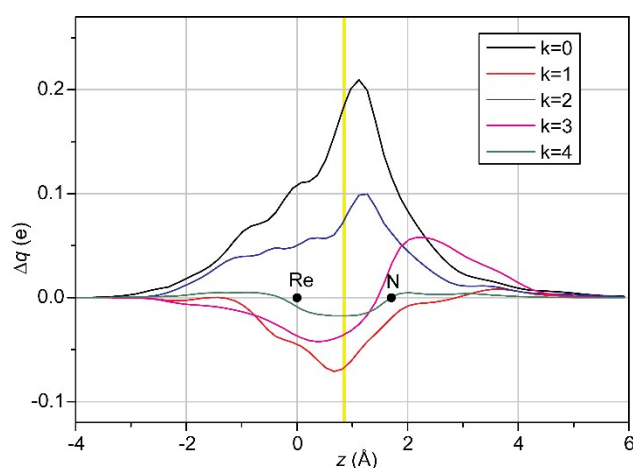


Figure S80. CD functions associated with  $\Delta\rho_k$  ( $k = 0 - 3$ ) for complex **Re6ClBiPy**. Black dots indicate the *z* position of the atomic nuclei. A yellow vertical band indicates the boundary between the two fragments.

Also the atomic charges, calculated through the Natural Bond Analysis (NBO<sup>8</sup>), evidence a substantial depletion of electronic density on the bipyridine upon the coordination on the rhenium center. In fact, the carbon bound to the chlorine passes from 0.26 to 0.29 e for the isolated and coordinated ligand, respectively.

In the reactant complex between **Re6ClBiPy** and the fluoride (**Re6ClBiPy-RC1**), the fluoride is hydrogen-bonded to the hydrogen of the bipyridine in position 3. The Gibbs free energy of **Re6ClBiPy-RC1** is -6.0 kcal/mol with respect to the isolated components. An isoergonic reactant complex (**Re6ClBiPy-RC2**) is possible, with the fluoride located over the bipyridine ligand. This adduct is favored because of the coordination of the ligand to the rhenium, which as seen before depletes the ligand of electronic density. From **Re6ClBiPy-RC2**, the fluoride attacks the carbonyl moiety *cis* to the bipyridine, leading to a -COF moiety bound to the rhenium (**Re6ClBiPy-Int1**, see Figure S). The fluoroacyl group is not common but it has been observed in the reaction between XeF<sub>2</sub> and [Ir(CO)<sub>3</sub>(PEt<sub>3</sub>)<sub>2</sub>]<sup>+</sup>.<sup>16</sup> In the transition state of this process (**Re6ClBiPy-TS1**), the carbon-fluoride distance is 2.265 Å and the Re-C-O angle is 162.2°.

Successively, the fluoride attacks the carbon bound to the chlorine, which, as seen previously, is depleted of electronic density. The geometry of the transition state is shown in Figure S. The C-Cl bond is evidently distorted, with the F-C and C-Cl distances 2.528 and 1.816 Å, respectively. The distance from the fluoride to the carbonyl is 2.341 Å. The activation free energy, ΔG<sup>‡</sup>, results to be quite low (6.3 kcal/mol).

The substitution of the chlorine with the fluorine leads to a free chloride and **Re6FBiPy**, with an energy gain of 35.3 kcal/mol with respect to the isolated reactants (**Error! Reference source not found.81**).

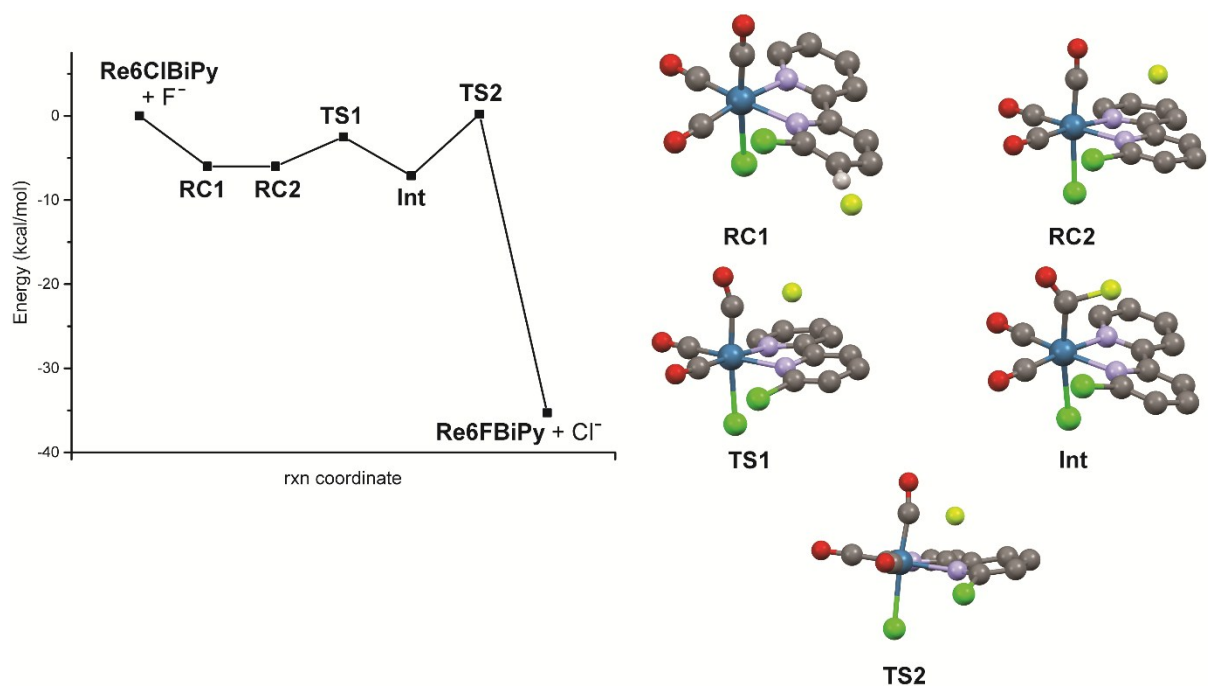


Figure S81. Energy diagram for the reaction of **Re6ClBiPy** and fluoride in DMSO and DFT-optimized geometries. Hydrogen atoms are omitted for clarity.

Modelling the reaction for an isolated **6ClBiPy** leads to a  $\Delta G^\ddagger$  of 34 kcal/mol, significantly higher than in the presence of the rhenium fragment.

The behavior of **Re2ClPhen** is qualitatively similar to that of **Re6ClBiPy**. The NOCV-CD bond analysis reveals that also in this case the ligand is substantially depleted of electronic density, with a  $M \leftarrow L$  donation of 0.24 e and a back-donation of -0.080 e. The  $\Delta G^\ddagger$  of the reaction is slightly higher than in the case of **Re6ClBiPy** (7.4 kcal/mol), but still accessible in the experimental conditions.

For the reactivity trend, a convenient and easy parameter is the partial charge of the carbon bound to the chlorine  $q(C)$ , calculated using the Natural Population Analysis as implemented in the NBO software (Table S2). It can be seen the position 5 is not enough “activated” by a chlorine and  $q(C)$  is negative even after the coordination on the rhenium centre. On the contrary, the  $\text{NO}_2$  group is electron-withdrawing enough to make  $q(C)$  positive, making that carbon susceptible of a nucleophilic attack as experimentally proven.

Table S2. Natural Population Analysis results for the atomic partial charge (in electrons) of the carbon bound to the chlorine.

<b>Complex</b>	<b>q(C)</b>	<b>Ligand</b>	<b>q(C)</b>
<b>Re6ClBiPy</b>	0.29	<b>6ClBiPy</b>	0.26
<b>Re6BrBiPy</b>	0.18	<b>6BrBiPy</b>	0.17
<b>Re5ClBiPy</b>	-0.01	<b>5ClBiPy</b>	-0.03
<b>Re4ClBiPy</b>	0.04	<b>4ClBiPy</b>	0.03
<b>Re6ClPhen</b>	0.31	<b>6ClPhen</b>	0.27
<b>Re5NO2Phen</b>	0.12	<b>5NO2Phen</b>	0.11
<b>Re5NO28HQ</b>	0.08	<b>Re5NO28HQ</b>	-

## S.6 Photophysical Analyses of Quantum Yields

In a former study we also verified the photophysical properties of the **Re2CIPhen** and **Re2FPhen** complexes for potential use of the latter as a PET-optical multimodal imaging agent.<sup>17</sup> Given the reasonable RCYs which were likewise obtained for the rhenium bipyridine complexes in this study, we further determined quantum yields of  $5.8 \times 10^{-3}$ ,  $1.1 \times 10^{-2}$ ,  $4.7 \times 10^{-3}$  and  $6.1 \times 10^{-3}$  for **Re4ClBiPy**, **Re5ClBiPy**, **Re6ClBiPy** and **Re6FBiPy** complexes in DMSO solution respectively.

The photophysical analyses were performed using an Edinburg FLS980 photospectrometer. Following confirmation of the excitation wavelength for the  $d\pi \rightarrow \pi^*$  transition to the MLCT excited state using UV-vis spectroscopy, emission scans of the rhenium complexes were subsequently performed on the same solution with the excitation wavelength set to the MLCT absorption maxima. The excitation light was emitted from a 450 W xenon arc lamp source and passed through a monochromator to selectively filter the excitation wavelength. Integration of the emission spectrum then provided an area representative of the number of emitted photons. The process was repeated with a reference standard, tris(bipyridine)ruthenium(II) chloride ( $[\text{Ru}(\text{BiPy})_3]\text{Cl}_2$ ), in an aqueous solution of known quantum yield (0.028).<sup>18</sup> By substituting the quantum yield ( $\phi$ ) of the reference solution as well as correction factors for the integrated area of the emission spectra ( $I$ ), absorbances of the solutions at the MLCT excitation wavelengths ( $A$ ) and the refractive indices of the solvents ( $n$ ) for both the reference and the analyte solution into the following equation, the quantum yield of the rhenium complexes were able to be determined:

$$\phi = \phi_r \left[ \frac{(I)(A_r)(n^2)}{(I_r)(A)(n_r^2)} \right]$$

The values determined for each of these parameters are listed in Table S3 for each of the tested rhenium(I) bipyridine complexes, alongside their calculated quantum yields. Figures S82-S85 show the emission spectra from which the integrated areas were determined.

Table S3. Quantum yields calculated for the **Re6ClBiPy**, **Re5ClBiPy**, **Re4ClBiPy** and **Re6FBiPy** complexes *via* comparison to a [Ru(BiPy)<sub>3</sub>]Cl<sub>2</sub> reference standard with correction factors applied for the refractive index of the media, absorbances at the 410 nm excitation wavelength and the integrations of the emission spectra.

Analyte	Solvent	Refractive Index	Absorbance	Emission Integration (counts·nm)	Quantum Yield (%)
[Ru(BiPy) <sub>3</sub> ]Cl	Water	1.333	0.045	4.50×10 <sup>6</sup>	2.8%
Re6ClBiPy	DMSO	1.479	0.337	5.14×10 <sup>6</sup>	0.5%
Re5ClBiPy	DMSO	1.479	0.321	9.57×10 <sup>6</sup>	1.0%
Re4ClBiPy	DMSO	1.479	0.369	6.19×10 <sup>6</sup>	0.6%
Re6FBiPy	DMSO	1.479	0.280	4.95×10 <sup>6</sup>	0.6%

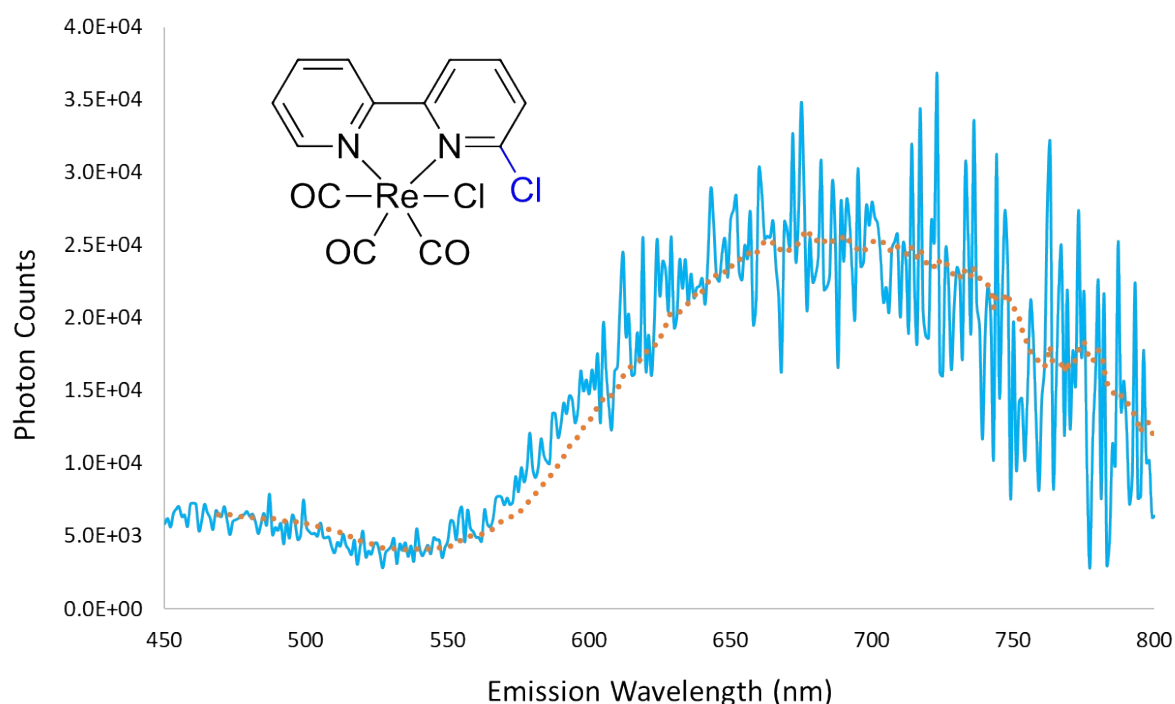


Figure S82. Emission spectrum of **Re6ClBiPy** in DMSO solution obtained using a 410 nm excitation wavelength. Dashed orange line is a moving average over 20 periods to help visualise the spectrum. The 5.14×10<sup>6</sup> counts·nm integration of this spectrum was used to calculate the quantum yield.

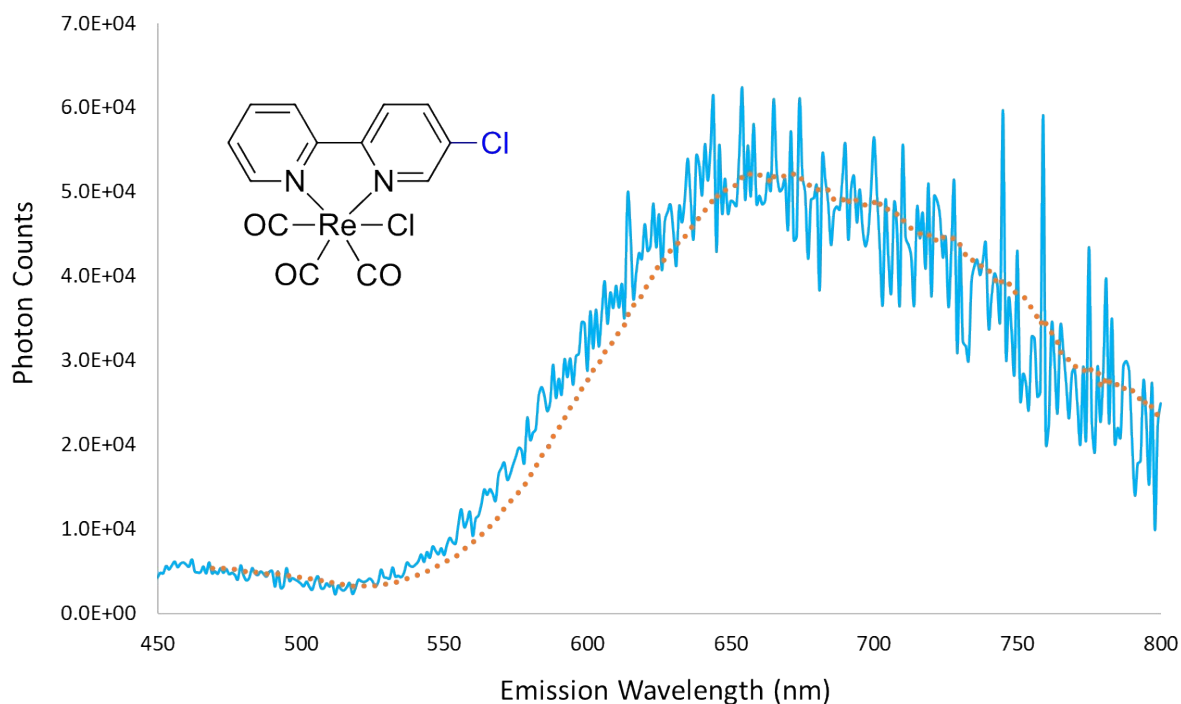


Figure S83. Emission spectrum of **Re5ClBiPy** in DMSO solution obtained using a 410 nm excitation wavelength. Dashed orange line is a moving average over 20 periods to help visualise the spectrum. The  $9.57 \times 10^6$  counts·nm integration of this spectrum was used to calculate the quantum yield.

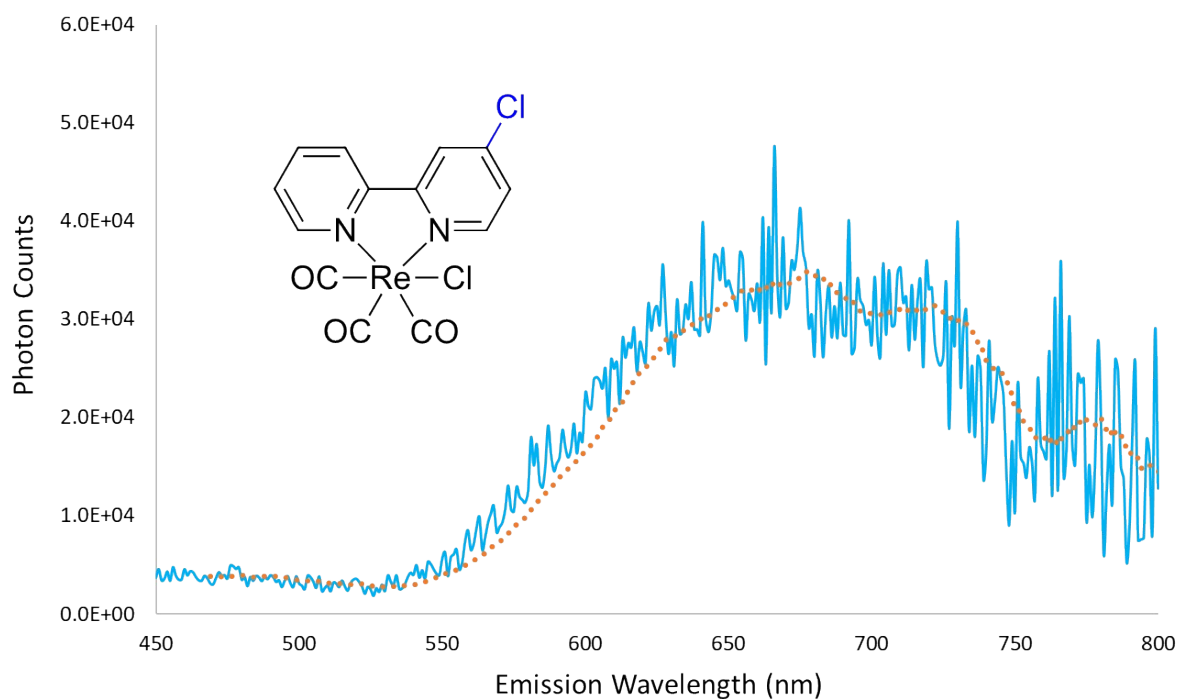


Figure S84. Emission spectrum of **Re4ClBiPy** in DMSO solution obtained using a 410 nm excitation wavelength. Dashed orange line is a moving average over 20 periods to help visualise the spectrum. The  $6.19 \times 10^6$  counts·nm integration of this spectrum was used to calculate the quantum yield.

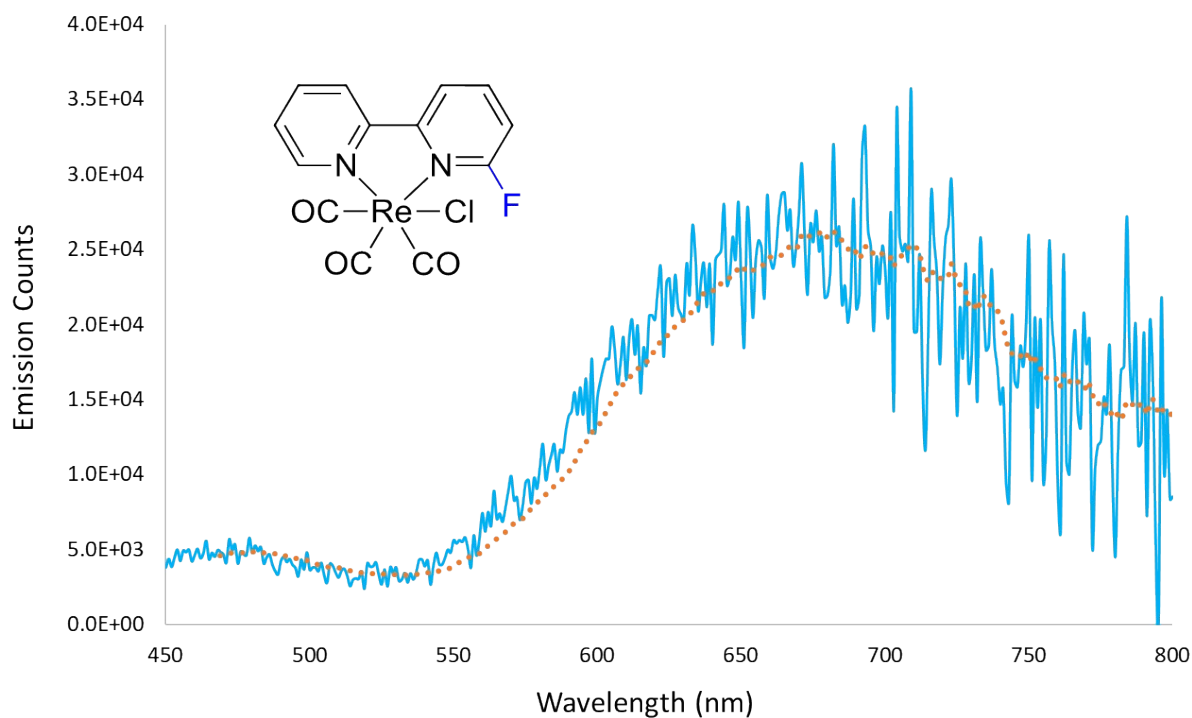


Figure S85. Emission spectrum of **Re6FBiPy** in DMSO solution obtained using a 380 nm excitation wavelength. Dashed orange line is a moving average over 20 periods to help visualise the spectrum. The  $4.95 \times 10^6$  counts·nm integration of this spectrum was used to calculate the quantum yield.

## S.7 Syntheses of Fluorinated Ligands

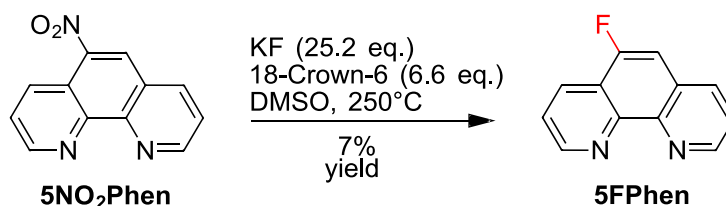


Figure S86. Nucleophilic aromatic substitution of **5NO<sub>2</sub>Phen** which afforded the desired **5FPhen** ligand in 7% yield.

A mass of potassium fluoride (5.915 g, 101.804 mmol, 25.2 eq.) was suspended over a mass of 18-crown-6 ether (7.036 g, 26.620 mmol, 6.6 eq.) and azeotropically dried *via* the addition of 20 x 1 mL aliquots of anhydrous acetonitrile while heating at 90°C under a constant stream of nitrogen gas and were subsequently dried under high vacuum. A mass of 5-nitro-1,10-phenanthroline (**5NO<sub>2</sub>Phen**, 909.7 mg, 4.039 mmol, 1.0 eq.) was concurrently dried under high vacuum before being dissolved in anhydrous DMSO (10 mL). This solution was then transferred to the fluoride complex mixture and the resulting solution was incrementally heated while monitoring by LRMS, HPLC and TLC technique. No product was found to form until the reaction temperature reached 250 °C, however. Following 2 hours of heating the solution was removed from heat due to the formation of other by-products and cooled to room temperature. The DMSO solution was filtered through a PTFE membrane (0.2 μm) and to isolate the potassium fluoride. The solution was then loaded onto a C<sub>18</sub> RP column (40 g) and eluted over a 0 to 100% gradient of acetonitrile in 0.1% TFA in water. The fractions determined to contain the purified **5FPhen** product by LRMS and HPLC analysis were combined and evaporated under reduced pressure to remove the acetonitrile. The sample was then freeze-dried overnight to remove the water and residual TFA, thus affording a pure orange powder (57.9 mg).

NMR confirmation of the product was first provided by <sup>1</sup>H-NMR analysis which showed the expected integration for seven protons in the aromatic region, as shown in Figure S87. The <sup>13</sup>C-NMR spectrum (Figure S88) for **5FPhen** shows sixteen signals due to four of the carbon-19 coupling with the lone fluorine-19 nucleus, which is evidenced by the signal at -79.5 ppm in the composite pulse decoupled <sup>19</sup>F-NMR spectrum in Figure S89. The LRMS also provides further confirmation of the **5FPhen** product, with a major ion signal with an *m/z* ratio of 199.23

depicted in the mass spectrum in Figure S90, which aligns closely with the calculated  $m/z$  ratio of 199.07 for the  $[M+H]^+$  ion ( $C_{12}H_7N_2FH^+$ ).

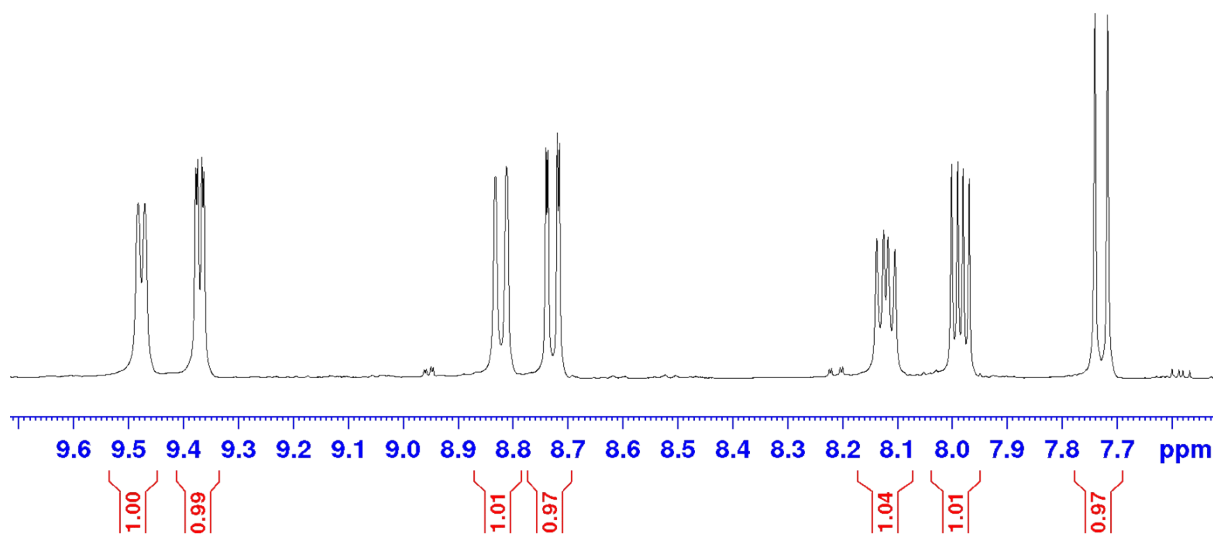


Figure S87. <sup>1</sup>H-NMR spectrum of **5FPhen** in chloroform-D<sub>3</sub> solution showing the expected integration for seven protons in the aromatic region.

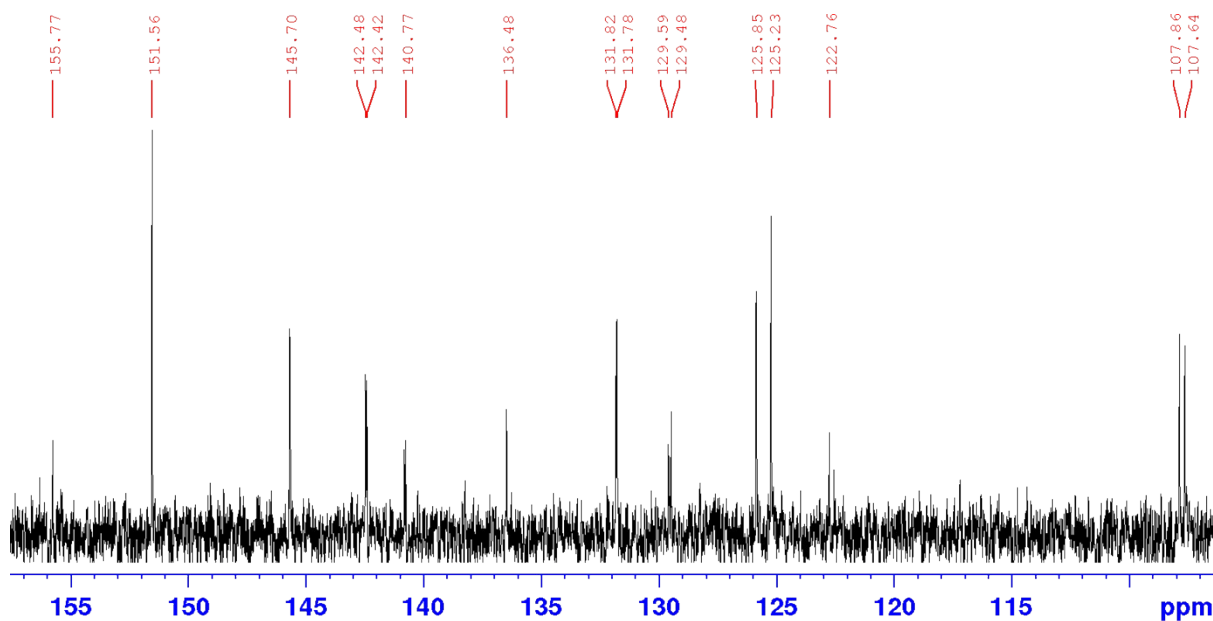


Figure S88. <sup>13</sup>C-NMR spectrum of **5FPhen** in chloroform-D<sub>3</sub> solution showing sixteen carbon-13 signals due to four of the twelve carbon-13 nuclei coupling with the fluorine-19 nucleus present within the molecule.

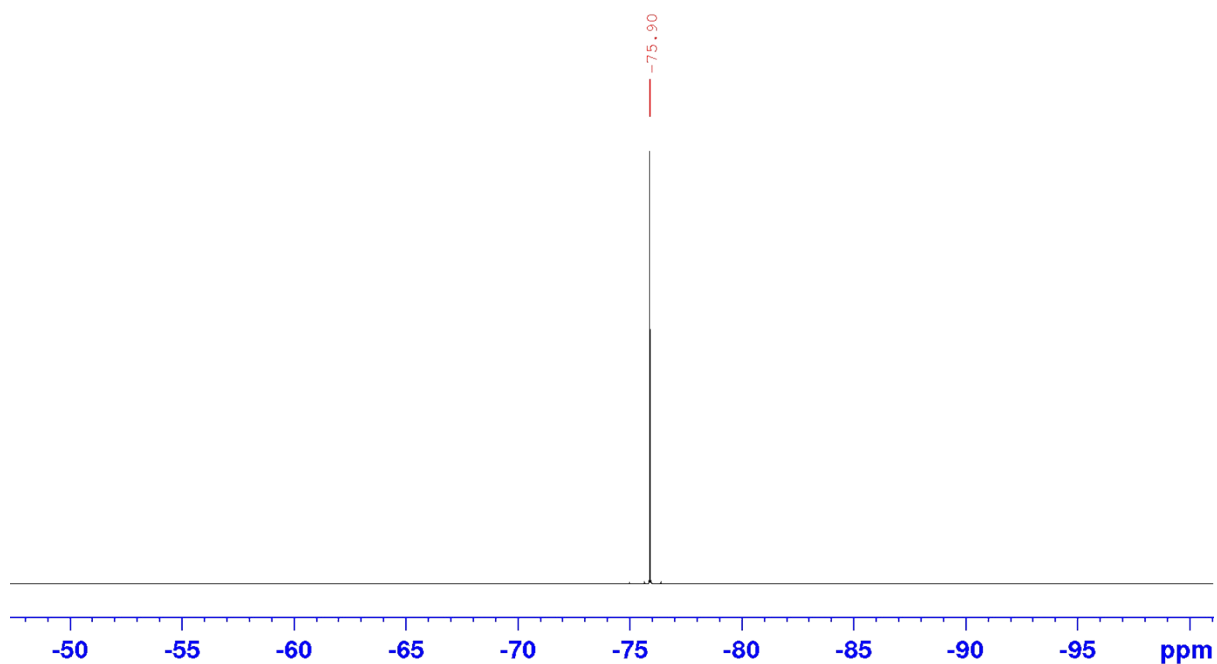


Figure S89. CPD  $^{19}\text{F}$ -NMR spectrum of **5FPhen** in chloroform- $\text{D}_3$  solution showing the lone signal of the fluorine-19 nucleus at -75.9 ppm.

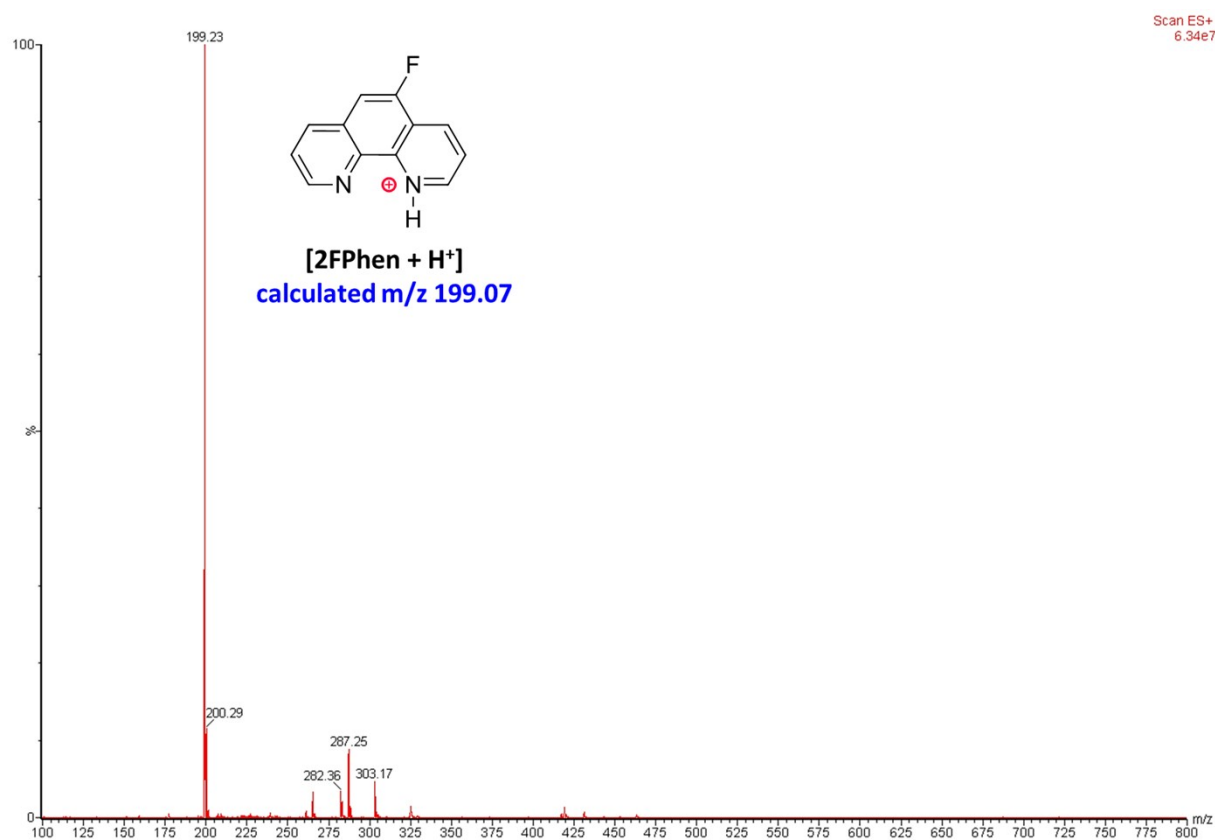


Figure S90. LRMS spectrum showing a major ion with an  $m/z$  ratio of 199.23, indicative of the protonated **5FPhen** compound with a calculated  $m/z$  ratio of 199.07.

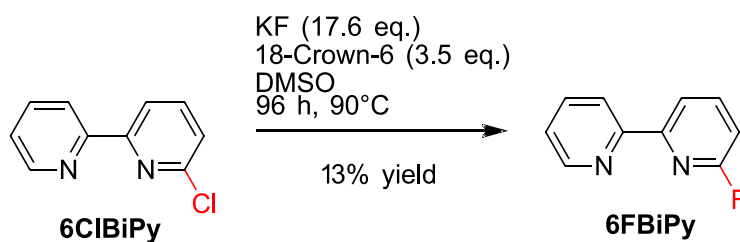


Figure S91. Synthesis of **6FBiPy** *via* nucleophilic aromatic substitution for fluoride provided by a potassium salt azeotropically dried in DMSO solvent in the presence of an 18-crown-6 ether phase transfer catalyst. The reaction afforded 13% yield following stirring at 90°C for 96 h under an inert nitrogen gas environment.

A mass of **6ClBiPy** (318.7 mg, 1.672 mmol, 1.0 eq.) was dried under high vacuum and back filled with nitrogen gas over three cycles. A volume of DMSO was distilled over calcium hydride and further dried over 4 Å molecular sieves. Masses of potassium fluoride (1.712 g, 29.466 mmol, 17.6 eq.) and 18-crown-6 ether (1.567 g, 5.928 mmol, 3.5 eq.) were azeotropically dried *via* small additions of acetonitrile (20 × 1 mL), with evaporation of the azeotrope occurring between additions, at 90°C under a constant flow of nitrogen gas. A homogeneous white crust resulted which was subsequently vacuumed and back filled with nitrogen gas over three cycles. A volume of the recently distilled anhydrous DMSO (10 mL) was then added to dissolve the 6-chloro-2,2'-bipyridine which turned yellow in solution and was then transferred to the potassium fluoride- crown ether complex under inert conditions. No product was afforded at room temperature, nor any temperature approaching 90°C while stirring in an inert nitrogen gas environment. Thus, the solution was left to stir at 90°C until the reaction achieved equilibration and no increase in the peak area of the product was identified, as confirmed by HPLC and MS monitoring (96 h). The reaction was thus cooled to room temperature and afforded a brown solution. The solution was loaded onto a silica column wet-packed with hexane and eluted over gradient conditions with a mobile phase ramped from 0% to 20% ethyl acetate in hexane. Fractions containing the co-eluting 6-chloro-2,2'-bipyridine and 6-fluoro-2,2'-bipyridine were then evaporated down under reduced pressure which afforded a white crystalline powder. The crude white powder was then dissolved in a minimum of methanol (2.2 mL) for preparative chromatography and a series of optimised 32 µL injections were loaded onto an Atlantis T3 C<sub>18</sub> reverse phase column (5 µm, 4.6 × 150 mm) and eluted with an isocratic mobile phase consisting of 9% acetonitrile and 91% of Milli-Q water with 0.1% TFA modifier at a flow rate of 1.5 mL.min<sup>-1</sup> and PDA detection wavelength set at 254 nm. The collected fractions were combined and evaporated under reduced pressure

to remove the acetonitrile before sublimating off the water *via* overnight lyophilisation, which afforded a pink salt. The pink salt was dissolved in a minimum of water (20 mL), neutralised with saturated sodium bicarbonate solution and extracted into DCM (15 × 10 mL) *via* liquid-liquid extraction. The resulting organic fractions were then combined, dried over sodium sulphate, vacuum filtered and evaporated under reduced pressure before dried under high vacuum which afforded a white powder (39.2 mg).

Confirmation of **6FBiPy** was verified by <sup>1</sup>H-NMR which affirmed the expected peak area integration for seven protons in the aromatic region, as shown in Figure S92. The <sup>13</sup>C-NMR spectrum of **6FBiPy**, shown in Figure S93, afforded twelve signals in the aromatic region due to two of the ten carbon-13 nuclei exhibiting coupling with the fluorine-19 nucleus. The <sup>19</sup>F-NMR spectrum of the compound shows the signal for the lone fluorine-19 nucleus alongside in Figure S94, alongside a *para*-difluorobenzene (*p*-DFB) internal standard.

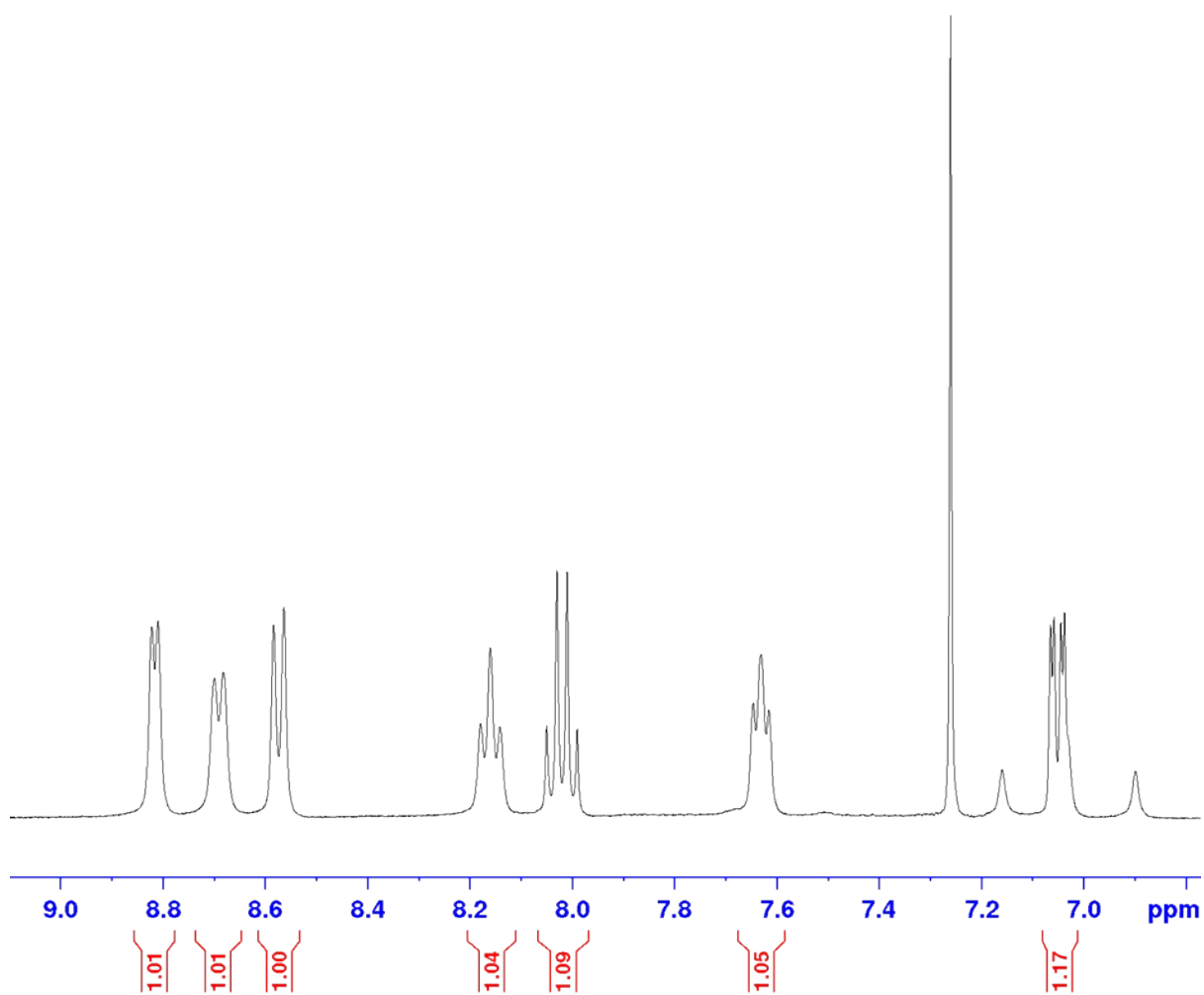


Figure S92.  $^1\text{H-NMR}$  spectrum of **6FBiPy** in  $\text{CDCl}_3$ , showing the expected peak area integration for seven protons in the aromatic region. Note the unintegrated peaks belong to the solvent signal and two satellite peaks of the upfield doublet of doublets.

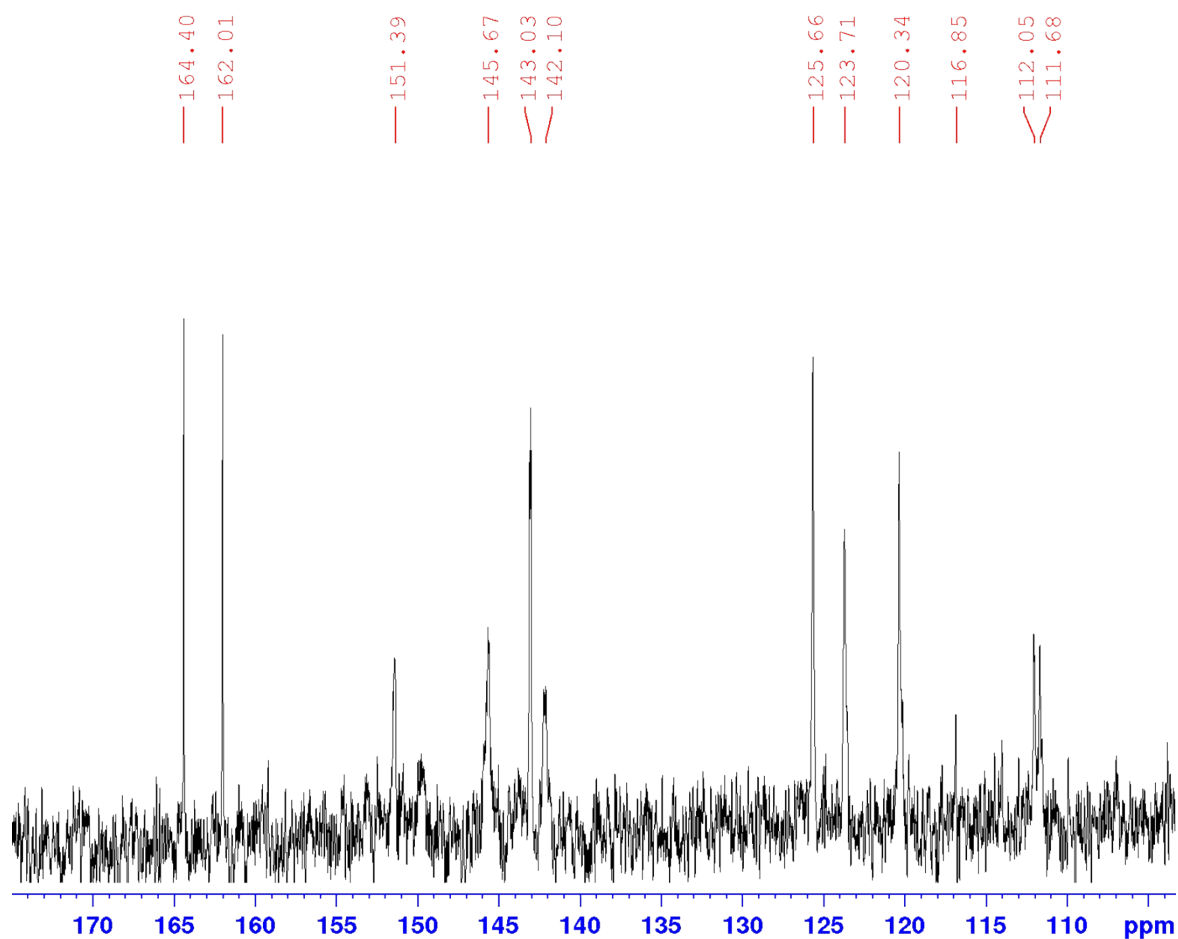


Figure S93.  $^{13}\text{C}$ -NMR spectrum of **6FBiPy** in  $\text{CDCl}_3$ , affording twelve signals in the aromatic region due to two additional signals appearing from two of the ten carbon atoms exhibiting observable coupling with the  $^{19}\text{F}$  nucleus present in the molecule.

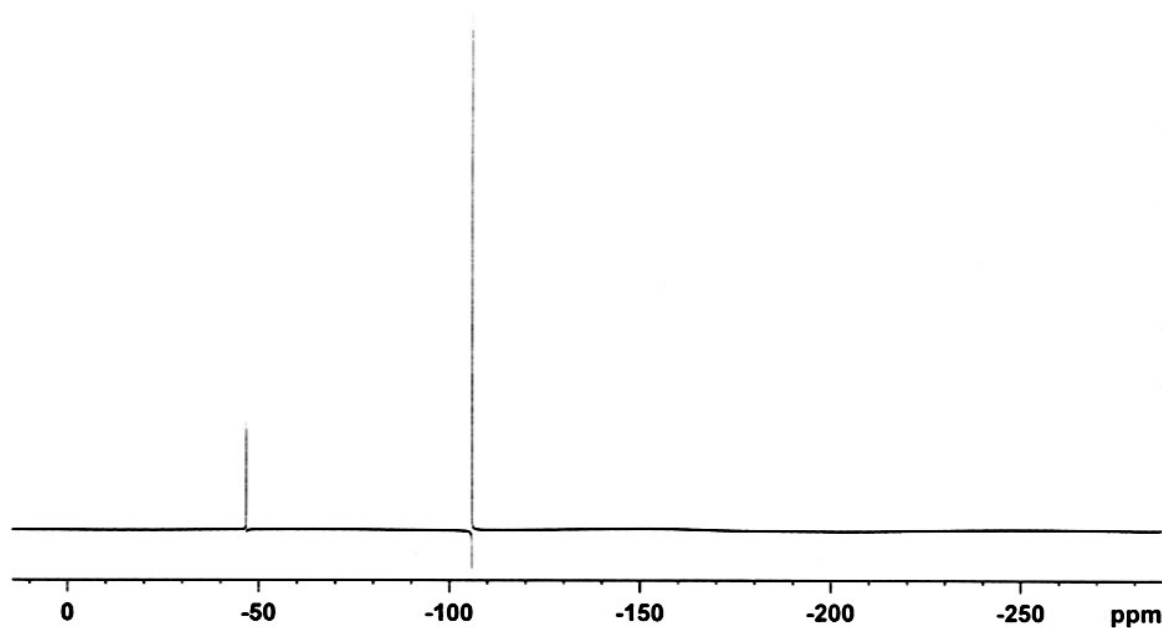


Figure S94.  $^{19}\text{F}$ -NMR spectrum of **6FBiPy** in  $\text{CDCl}_3$ . The signal at -106.00 ppm is the *para*-DFB internal standard.

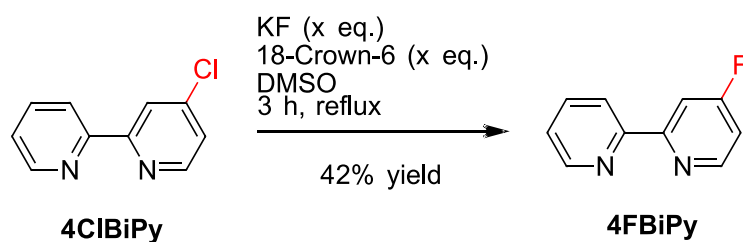


Figure S95. Synthesis of **4FBiPy** *via* nucleophilic aromatic substitution for fluoride provided by a potassium salt azeotropically dried in DMSO solvent in the presence of an 18-crown-6 ether phase transfer catalyst. The reaction afforded 42% yield following stirring at reflux for 3 h under an inert nitrogen gas environment.

A mass of 18-crown-6 ether (4.060 g, 0.0154 mol, 9.8 eq.) was added alongside a mass of potassium fluoride (1.890 g, 0.0325 mol, 20.8 eq.) and dried under high vacuum before heating under an inert nitrogen environment to form a yellow crust which was then azeotropically dried *via* the dropwise addition of acetonitrile to the heated solid. A mass of **4ClBiPy** (298.2 mg, 1.564 mmol, 1.0 eq.) was then dried under high vacuum and backfilled with nitrogen gas in a separate flask before being dissolved in a volume of anhydrous DMSO (4 mL) resulting in a pale-yellow solution. The solution was then transferred to the potassium fluoride-crown ether complex and was heated at reflux whilst stirring in an inert nitrogen environment (3 h). The solution was then cooled to room temperature following HPLC-UV and MS confirmation of the desired product. The cooled solution was filtered through PTFE membrane filters (0.2  $\mu\text{m}$ ) to remove the excess potassium fluoride and the filtered solution was then loaded onto a C<sub>18</sub> RP column (80 g) primed with 0.1% TFA in water and eluted over 20 column volumes with a flow rate of 40 mL.min<sup>-1</sup> with increasing acetonitrile composition (0 to 100%). Each of the eluted fractions were analysed for purity by HPLC, TLC and MS. Those fractions confirmed to contain the purified product were combined and evaporated under reduced pressure to remove the acetonitrile before freeze-drying the resulting aqueous suspension overnight. A yellow oil resulted which was washed first with chloroform and evaporated under reduced pressure to afford a yellow solid. The yellow solid was then dissolved in a minimum of water and extracted with DCM (10  $\times$  20 mL). The organic extracts were then combined, dried over sodium sulphate, filtered *via* vacuum filtration and evaporated under reduced pressure to afford a white solid which was then further dried under high vacuum and weighed (115.1 mg).

<sup>1</sup>H-NMR analysis of the final product (Figure S96) showed the expected integration for seven protons in the aromatic region, <sup>13</sup>C-NMR analysis (Figure S97) showed splitting of three of the

ten carbon-13 nuclei due to coupling to the fluorine-19 nucleus, the resonance signal of which is shown in the CPD  $^{19}\text{F}$ -NMR spectrum of **4FBiPy** in Figure S98. The LRMS spectrum of **4FBiPy**, shown in Figure S99, shows a detected signal for the  $[\text{M}+\text{H}]^+$  ion at  $m/z$  175.12 closely matching the calculated  $m/z$  ratio of 175.07.

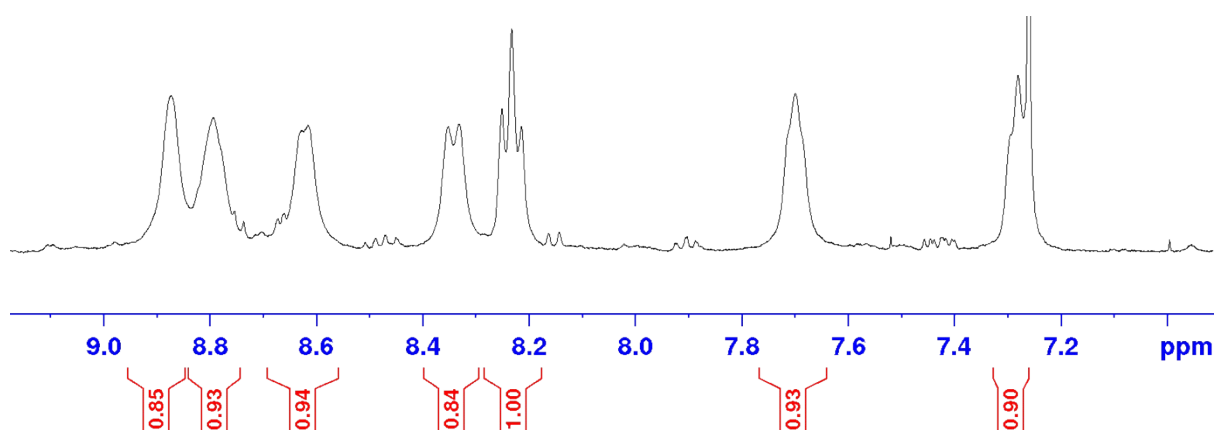


Figure S96.  $^1\text{H}$ -NMR spectrum of **4FBiPy** in chloroform- $d$ , showing the expected peak area integration for seven protons in the aromatic region. Note that the most upfield shifted peak integral overlaps with the solvent signal.

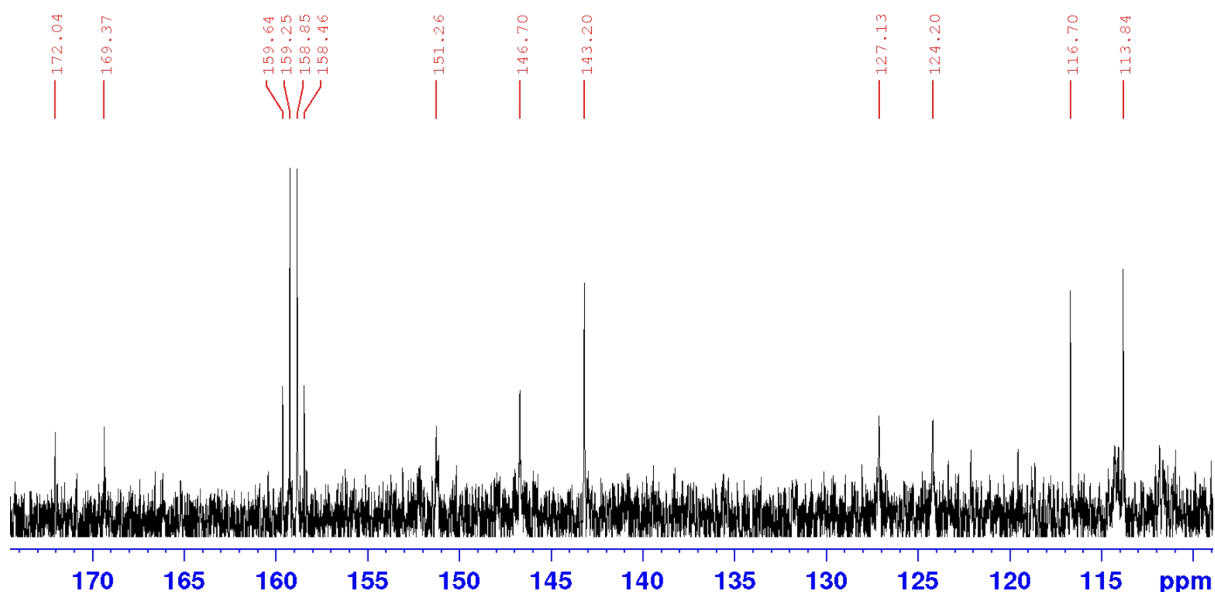


Figure S97.  $^{13}\text{C}$ -NMR spectrum of **4FBiPy** in chloroform- $d$ , affording thirteen signals in the aromatic region due to three additional signals appearing from three of the ten carbon nuclei exhibiting observable coupling with the fluorine-19 nucleus present in the molecule.

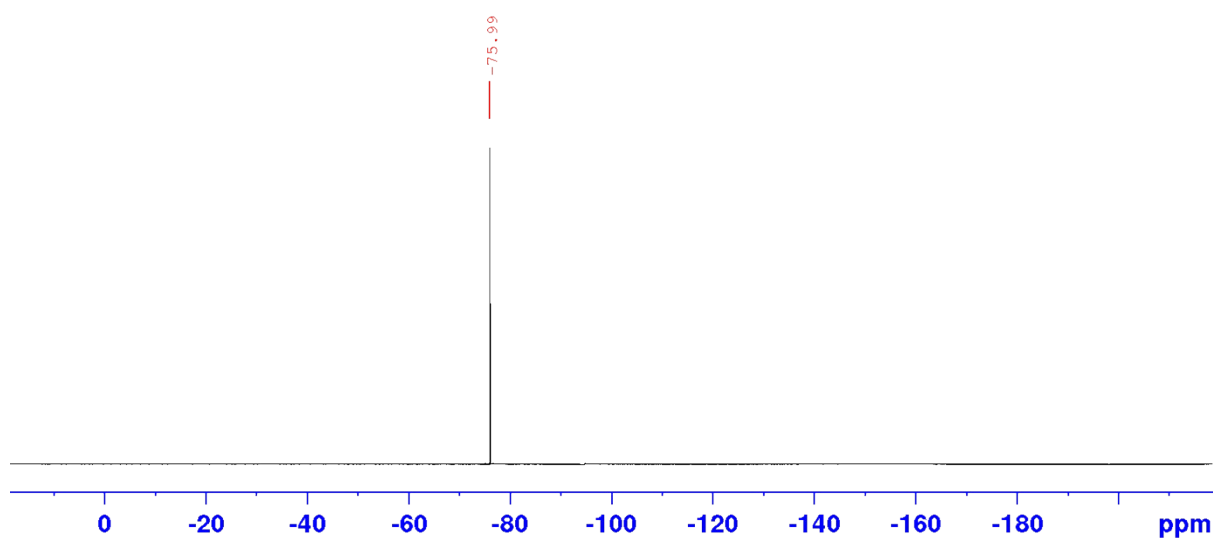


Figure S98. CPD <sup>19</sup>F-NMR spectrum for **4FBiPy** exhibiting one lone single for the sole fluorine-19 nucleus in the molecule at -75.99 ppm.

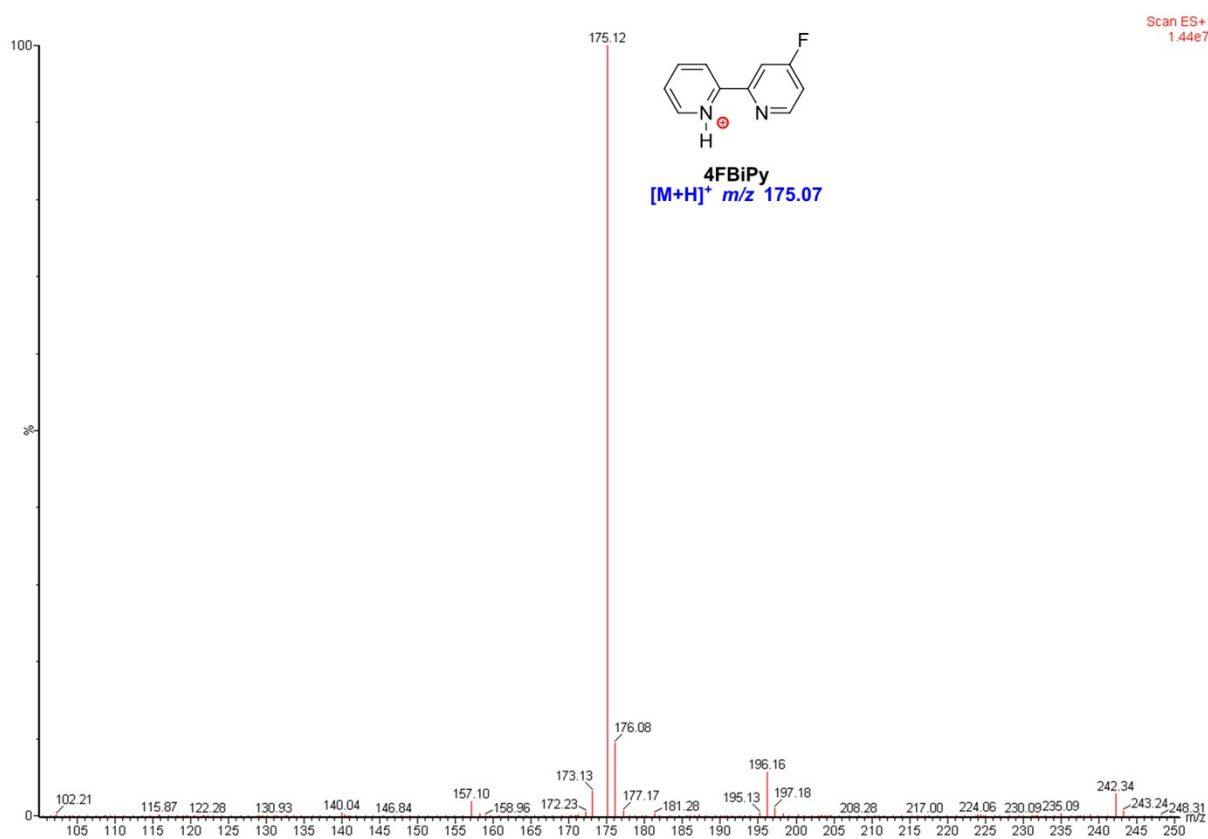


Figure S99. LRMS spectrum of **4FBiPy** showing detection of the [M+H]<sup>+</sup> ion at  $m/z$  175.12 against a calculated ratio of  $m/z$  175.07.

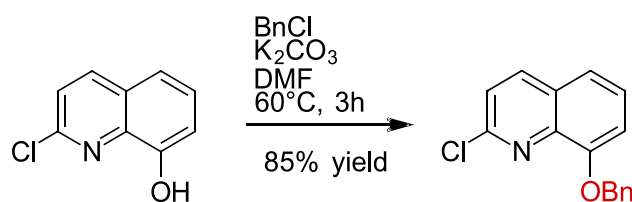


Figure S100. Protection of the **2Cl8HQ** alcohol in the 8-position using benzyl chloride to afford **2Cl8HQ-OBn** in 85% yield.

A mass of **2Cl8HQ** (2.40 g, 13.362 mmol, 1.0 eq.) was dissolved in a volume of anhydrous DMF (2.5 mL) to which a mass of potassium carbonate (3.69 g, 26.693 mmol, 2.0 eq.) was added. A volume of benzyl chloride (3.1 mL, 27.360 mmol, 2.0 eq.) was then added dropwise to the solution. The reaction mixture was stirred at 60 °C for 3 hours, where after HPLC reaction monitoring confirmed near complete conversion to the product. The product was extracted into DCM (20 × 10 mL) and the combined organic fractions were back extracted with brine (2 × 20 mL). The organic layer was then dried over sodium sulphate, filtered *via* vacuum filtration and evaporated under reduced pressure to afford a light pink solid. The solid was then recrystallised from hot ethanolic solution and filtered *via* vacuum filtration to afford a purified pink product (3.02 g).

Confirmation of the product was assessed by NMR analysis, with the <sup>1</sup>H-NMR spectrum of **2Cl8HQ-OBn** shown in Figure S101 exhibiting the expected integration for twelve protons. Ten of which existed in the aromatic region, pertaining to the hydrogen atoms bonded within the quinoline and benzene rings, and the other two being relatively upfield shifted as expected for the methylene group protons. The <sup>13</sup>C-NMR spectrum, shown in in Figure S102, further evidenced the assigned structure with fourteen carbon-13 nuclear resonance signals found present, as expected given the similar magnetic environment for two pairs of the sixteen carbon atoms.

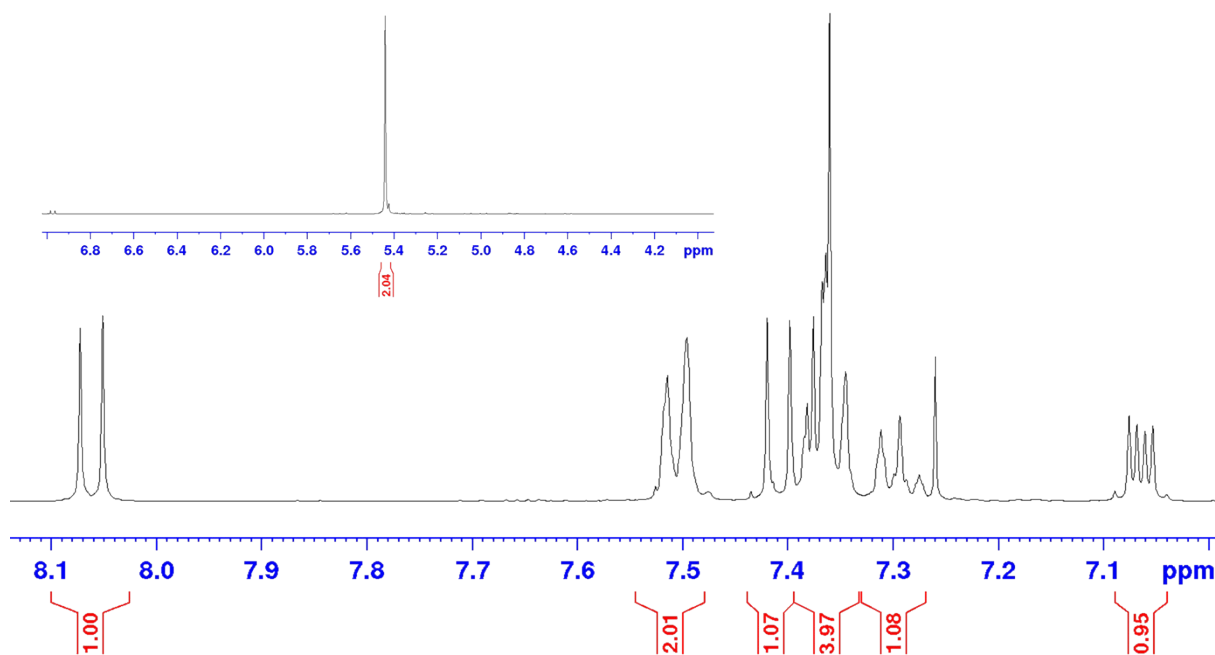


Figure S101.  $^1\text{H}$ -NMR spectrum depicting the integrations of the resonance signals for the twelve expected protons in **2Cl8HQ-OBn**. Ten of these protons exhibit resonance in the aromatic region, whereas the two protons of the methyl group are upfield shifted by comparison (top left corner).

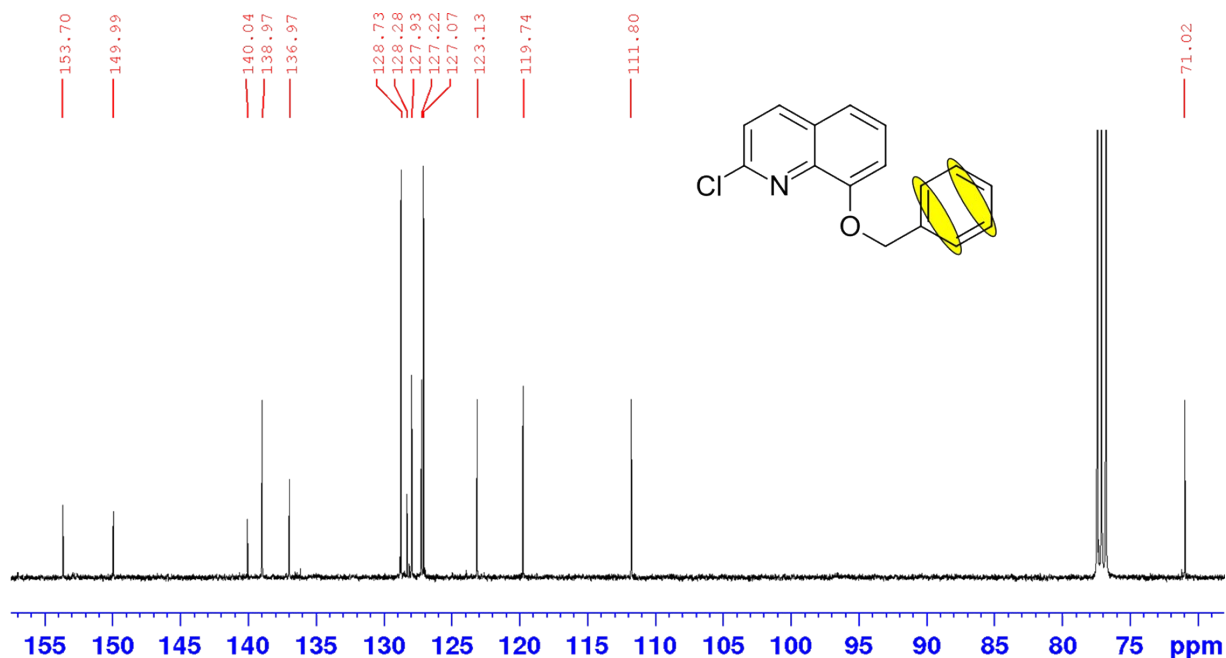


Figure S102.  $^{13}\text{C}$ -NMR spectrum of **2Cl8HQ-OBn** in chloroform- $d$ , depicting the fourteen expected fourteen signals for the sixteen carbon-13 nuclei as two pairs of carbon atoms share the same magnetic environment as shown by the yellow highlighted regions of the molecule. The carbon-13 nucleus of the methyl group is notably upfield shifted by comparison.

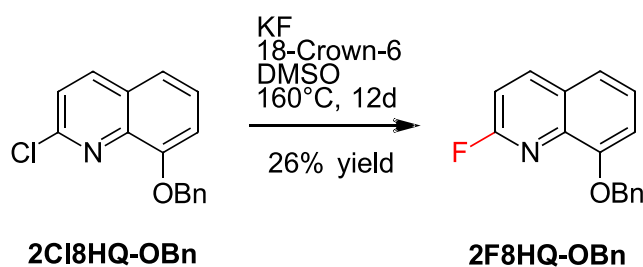


Figure S103. Fluorination of **2Cl8HQ-OBn** using potassium fluoride and an 18-crown-6 ether phase transfer catalyst to afford **2F8HQ-OBn** in 26% yield.

A mass of **2Cl8HQ-OBn** (1.48 g, 5.487 mmol, 1.0 eq.) was purged under nitrogen and vacuum before being dissolved in a volume of anhydrous DMSO (10 mL). Masses of potassium fluoride (3.84 g, 66.093 mmol, 12.0 eq.) and 18-crown-6 ether (5.84 g, 22.094 mmol, 4.0 eq.) were azeotropically dried at 90 °C *via* the dropwise addition of anhydrous acetonitrile under an inert nitrogen environment. The ligand solution was then transferred to the vial containing the potassium-crown ether complex and the solution was slowly heated to 160 °C and stirred in an inert nitrogen environment for 12 days. As reaction monitoring suggesting no greater product formation was eventuating, the solution was then cooled to room temperature. The solution was then filtered through a PTFE membrane (0.2 μm) before loading onto a C<sub>18</sub> reverse phase column (220 g, 40 μm) and eluted over a gradient mobile phase consisting of 1 to 100% acetonitrile in water, each containing 0.1% TFA modifier. Fractions found to contain the desired **2F8HQ-OBn** product were combined and evaporated under reduced pressure to remove the acetonitrile before freeze-drying overnight to pink salt. The presumed TFA salt was then dissolved in a minimum volume of water and extracted into DCM (10 × 5 mL). The combined organic extracts were then dried over sodium sulphate, filtered *via* vacuum filtration and evaporated under reduced pressure to afford the pure product (357.4 mg).

<sup>1</sup>H-NMR spectrometry revealed differing splitting patterns, owing to coupling with the fluorine-19 nucleus, though still retained the expected integration for twelve protons with ten of those signals existing within the aromatic region of the spectrum, shown in Figure S104, as expected. The <sup>13</sup>C-NMR spectrum, shown in Figure S105, exhibited twenty-one signals due to five instances of carbon-13 nuclei coupling to the sole fluorine-19 nucleus whose resonance signal is shown at -31.07 ppm in the <sup>19</sup>F-NMR spectrum of **2F8HQ-OBn**, as shown in Figure S106.

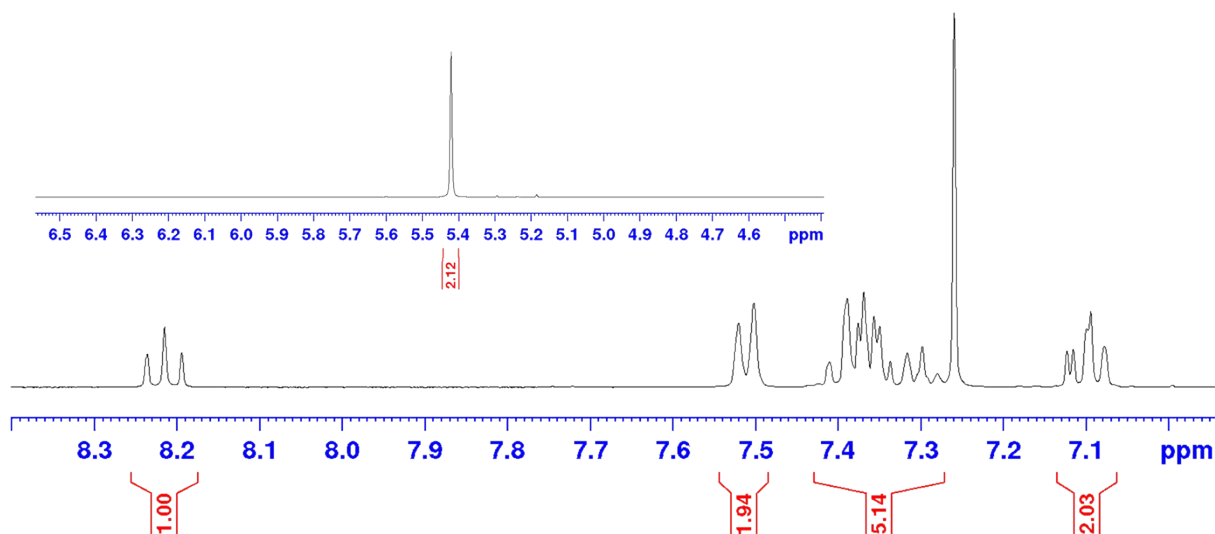


Figure S104.  $^1\text{H}$ -NMR spectrum depicting the integrations of the resonance signals for the twelve expected protons in **2F8HQ-OBn**. Ten of these protons exhibit resonance in the aromatic region, whereas the two protons of the methyl group are upfield shifted by comparison (top left corner).

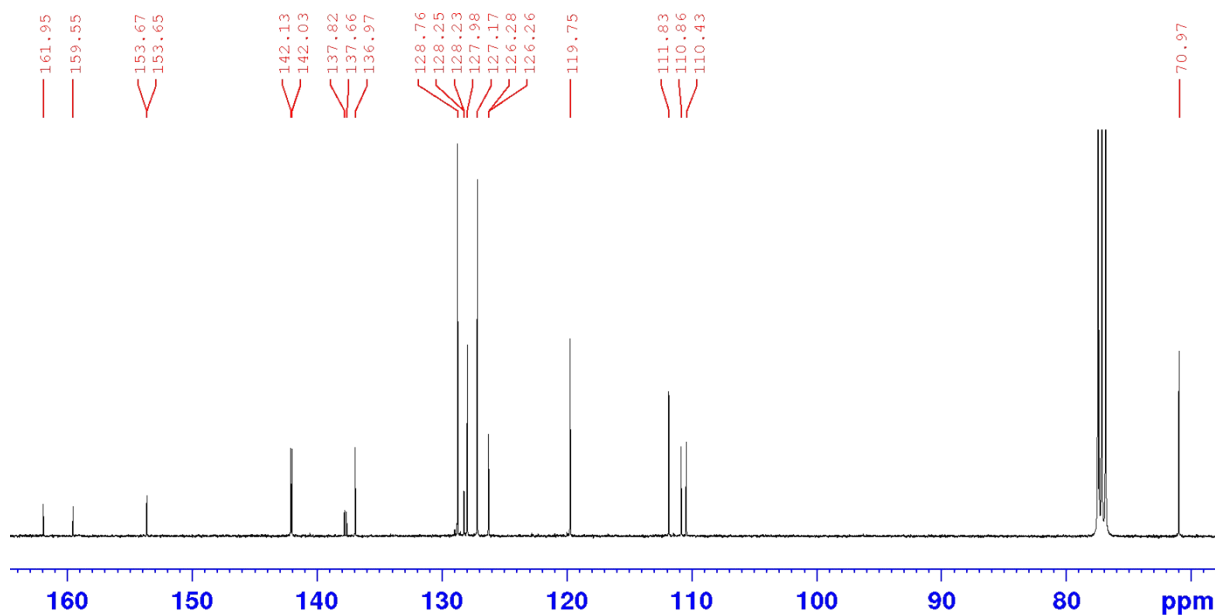


Figure S105.  $^{13}\text{C}$ -NMR spectrum of **2F8HQ-OBn** in chloroform- $d$  exhibiting twenty-one resonance signals due to five of the carbon-13 nuclei coupling to the fluorine-19 nucleus.

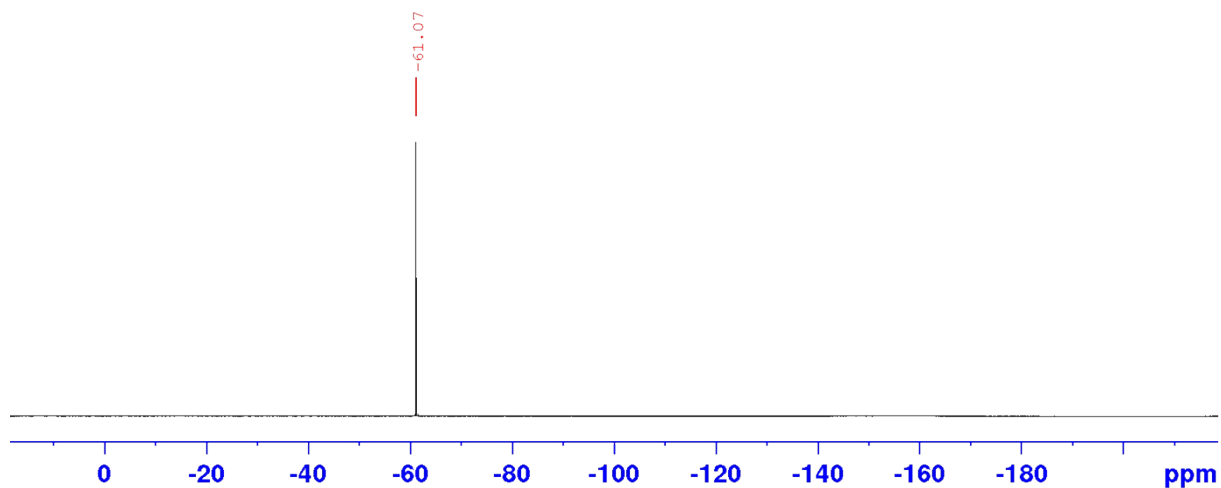


Figure S106. CPD  $^{19}\text{F}$ -NMR spectrum of **2F8HQ-OBn** in chloroform-d showing the fluorine-19 magnetic resonance signal at -61.07 ppm pertaining to the lone fluorine-19 nucleus in the molecule.

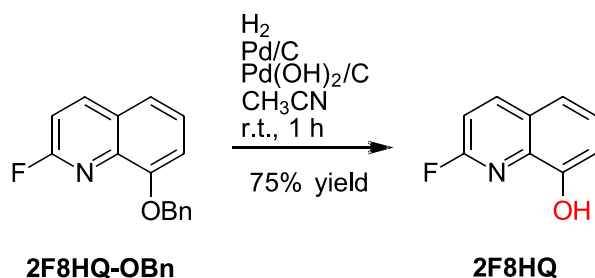


Figure S107. Deprotection of **2F8HQ-OBn** using hydrogen gas in the presence of palladium on activated carbon catalysts to afford **2F8HQ** in 75% yield.

A mass of **2F8HQ** (217.6 mg, 0.859 mmol, 1.0 eq.) was dissolved in a volume of acetonitrile (6 mL). Masses of 10% wt. palladium on activated carbon (123.4 mg) and 20% wt. palladium hydroxide on activated carbon (124.7 mg) were added to the reaction mixture under an inert nitrogen gas environment. The nitrogen gas was then displaced with hydrogen gas and the mixture left to stir for 1 hour. The solution was then filtered over diatomaceous earth *via* vacuum filtration to afford a pale-yellow solution which was evaporated under reduced pressure to afford a golden crystalline solid (105.7 mg).

The  $^1\text{H-NMR}$  spectrum of the product (Figure S108) shows the expected integration for six protons in the aromatic region alongside a broad and significantly downfield shifted signal suggestive of the O–H bond. The  $^{13}\text{C-NMR}$  spectrum in Figure S109 exhibits fourteen carbon-13 nuclear resonance signals due to coupling of five carbon-13 nuclei with the fluorine-19 nucleus. This fluorine-19 nucleus is evident from the single resonance signal in the CPD  $^{19}\text{F-NMR}$  spectrum of **2F8HQ** in Figure S110.

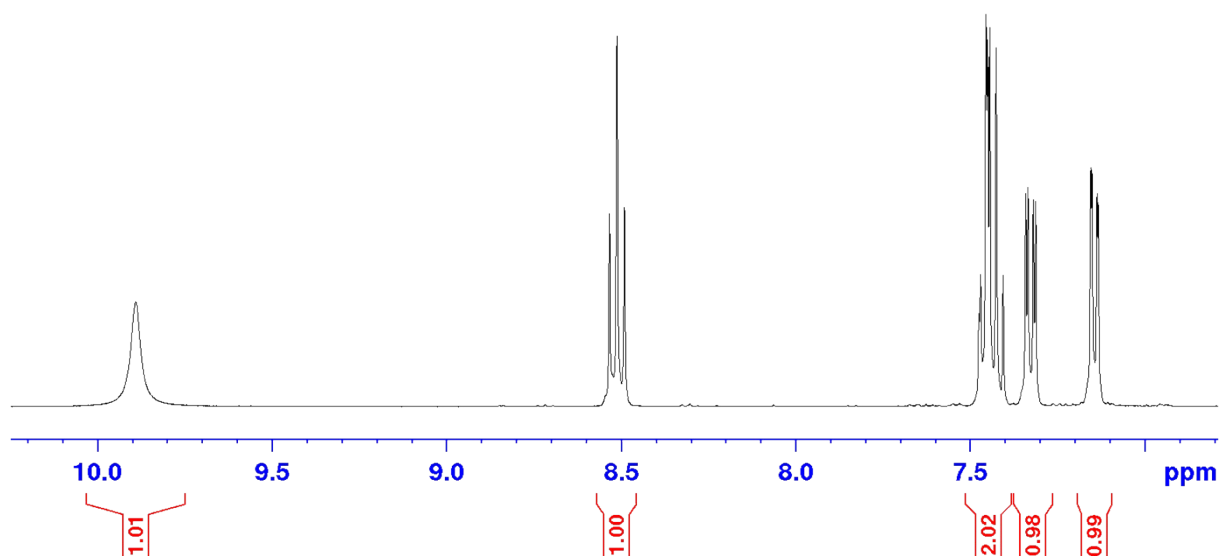


Figure S108.  $^1\text{H}$ -NMR spectrum of **2F8HQ** in  $\text{DMSO-d}_6$  showing the expected integration for six protons in the aromatic region including a broad signal pertaining to the O–H bonded hydrogen atom.

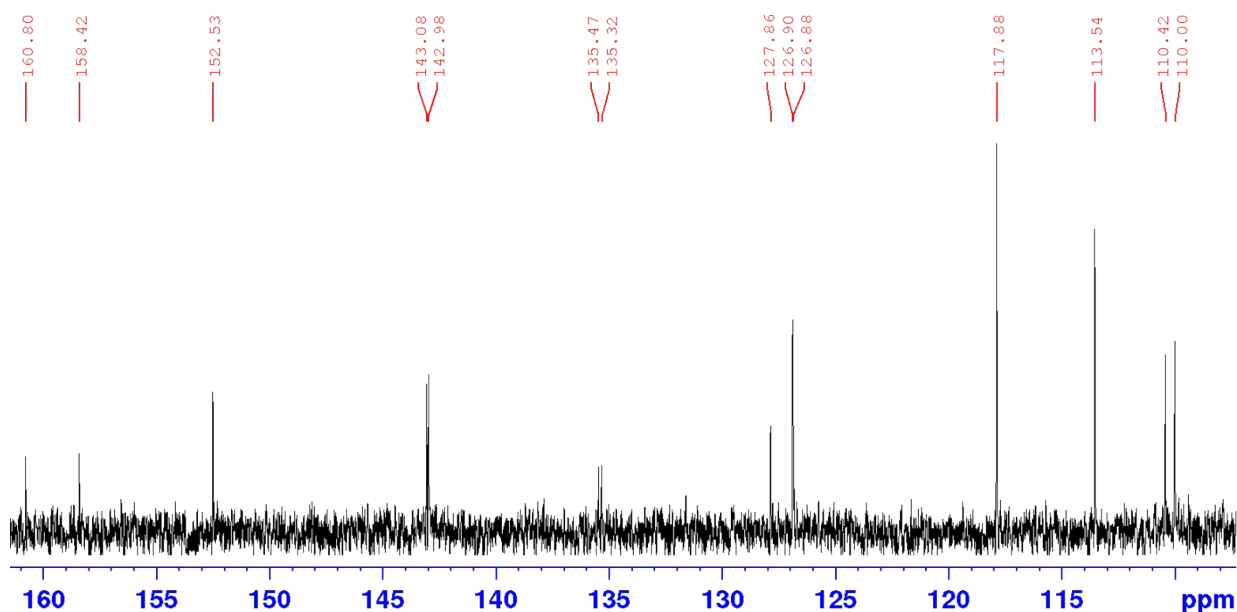


Figure S109.  $^{13}\text{C}$ -NMR spectrum of **2F8HQ** in  $\text{DMSO-d}_6$  showing fourteen carbon-13 nuclear resonance signals due to the carbon-13 nuclei in the pyridinyl ring coupling with the fluorine-19 nucleus.

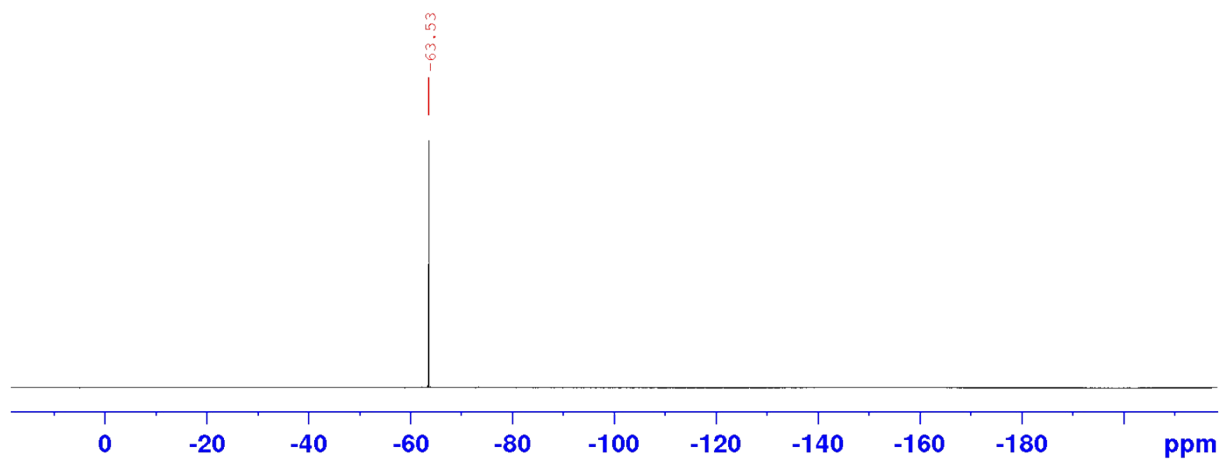


Figure S110. CPD  $^{19}\text{F}$ -NMR spectrum of **2F8HQ** showing the resonance single for the sole fluorine-19 nucleus in the molecule at -63.53 ppm.

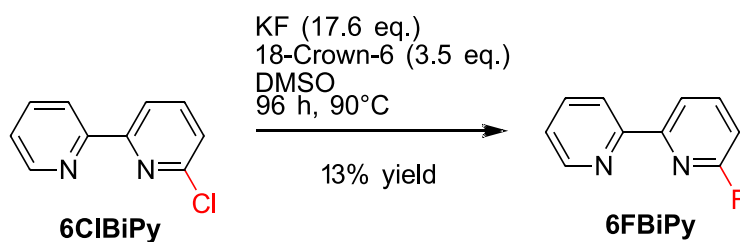


Figure S111. Synthesis of **6FBiPy** *via* nucleophilic aromatic substitution for fluoride provided by a potassium salt azeotropically dried in DMSO solvent in the presence of an 18-crown-6 ether phase transfer catalyst. The reaction afforded 13% yield following stirring at 90°C for 96 h under an inert nitrogen gas environment.

A mass of **6ClBiPy** (318.7 mg, 1.672 mmol, 1.0 eq.) was dried under high vacuum and back-filled with nitrogen gas over three cycles. A volume of DMSO was distilled over calcium hydride and further dried over 4 Å molecular sieves. Masses of potassium fluoride (1.712 g, 29.466 mmol, 17.6 eq.) and 18-crown-6 ether (1.567 g, 5.928 mmol, 3.5 eq.) were azeotropically dried *via* small additions of acetonitrile (20 × 1 mL), with evaporation of the azeotrope occurring between additions, at 90°C under a constant flow of nitrogen gas. A homogeneous white crust resulted which was subsequently vacuumed and back-filled with nitrogen gas over three cycles. A volume of the recently distilled anhydrous DMSO (10 mL) was then added to dissolve the 6-chloro-2,2'-bipyridine which turned yellow in solution and was then transferred to the potassium fluoride- crown ether complex under inert conditions. No product was afforded at room temperature, nor any temperature approaching 90°C while stirring in an inert nitrogen gas environment. Thus, the solution was left to stir at 90°C until the reaction achieved equilibration and no increase in the peak area of the product was identified, as confirmed by HPLC and MS monitoring (96 h). The reaction was thus cooled to room temperature and afforded a brown solution. The solution was loaded onto a silica column wet-packed with hexane and eluted over gradient conditions with a mobile phase ramped from 0% to 20% ethyl acetate in hexane. Fractions containing the co-eluting 6-chloro-2,2'-bipyridine and 6-fluoro-2,2'-bipyridine were then evaporated down under reduced pressure which

afforded a white crystalline powder. The crude white powder was then dissolved in a minimum of methanol (2.2 mL) for preparative chromatography and a series of optimised 32  $\mu$ L injections were loaded onto an Atlantis T3 C<sub>18</sub> reverse phase column (5  $\mu$ m, 4.6  $\times$  150 mm) and eluted with an isocratic mobile phase consisting of 9% acetonitrile and 91% of Milli-Q water with 0.1% TFA modifier at a flow rate of 1.5 mL.min<sup>-1</sup> and PDA detection wavelength set at 254 nm. The collected fractions were combined and evaporated under reduced pressure to remove the acetonitrile before sublimating off the water *via* overnight lyophilisation, which afforded a pink salt. The pink salt was dissolved in a minimum of water (20 mL), neutralised with saturated sodium bicarbonate solution and extracted into DCM (15  $\times$  10 mL) *via* liquid-liquid extraction. The resulting organic fractions were then combined, dried over sodium sulphate, vacuum filtered and evaporated under reduced pressure before dried under high vacuum which afforded a white powder (39.2 mg).

Confirmation of **6FBiPy** was verified by <sup>1</sup>H-NMR which affirmed the expected peak area integration for seven protons in the aromatic region, as shown in Figure . The <sup>13</sup>C-NMR spectrum of **6FBiPy**, shown in Figure , afforded twelve signals in the aromatic region due to two of the ten carbon-13 nuclei exhibiting coupling with the fluorine-19 nucleus. The CPD <sup>19</sup>F{<sup>1</sup>H}-NMR spectrum of the compound shows the signal for the lone fluorine-19 nucleus in Figure , alongside the *para*-DFB internal standard.

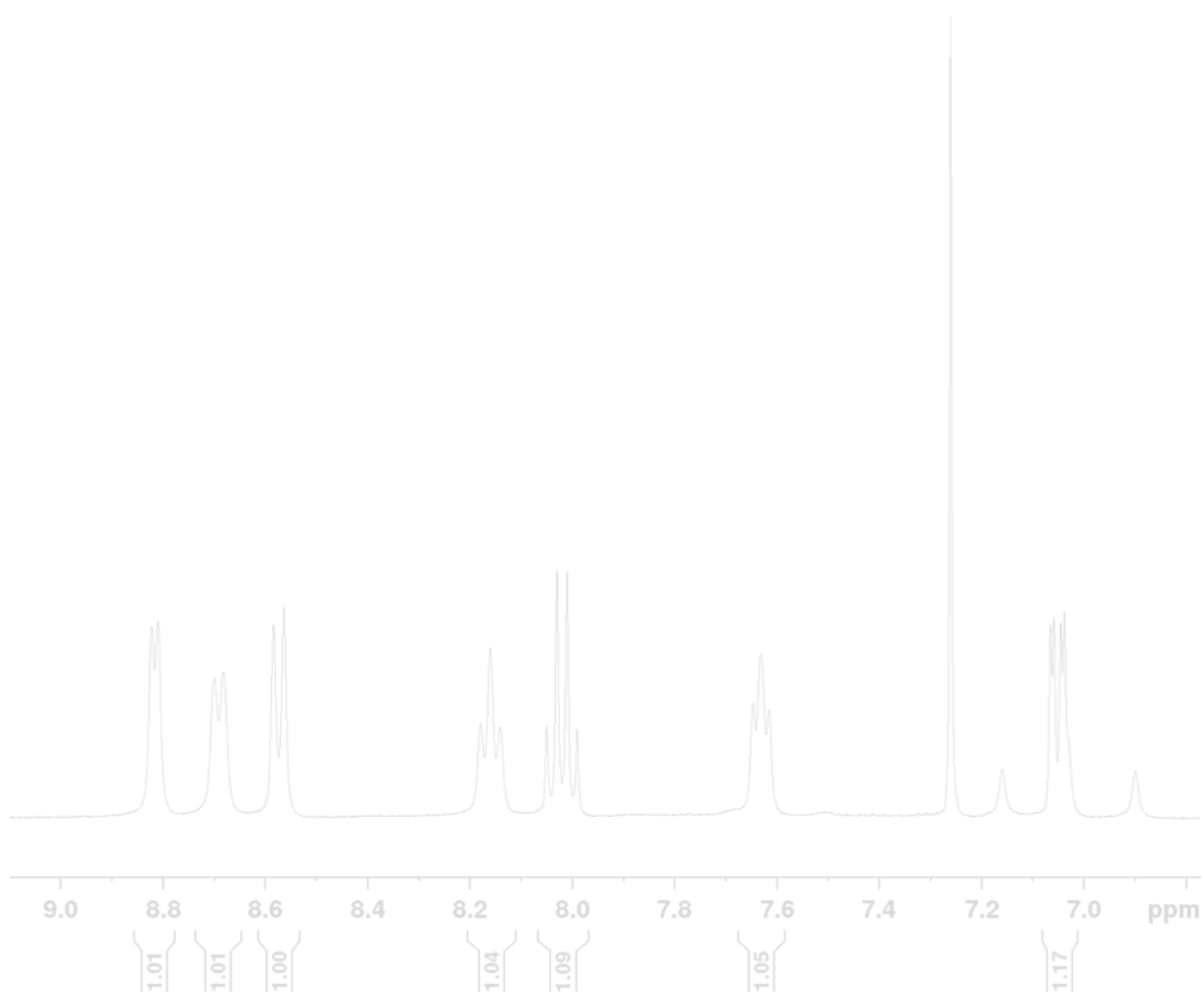


Figure S112. <sup>1</sup>H-NMR spectrum of **6FBiPy** in CDCl<sub>3</sub>, showing the expected peak area integration for seven protons in the aromatic region. Note the non-integrated peaks belong to the solvent signal and two satellite peaks of the upfield doublet of doublets.

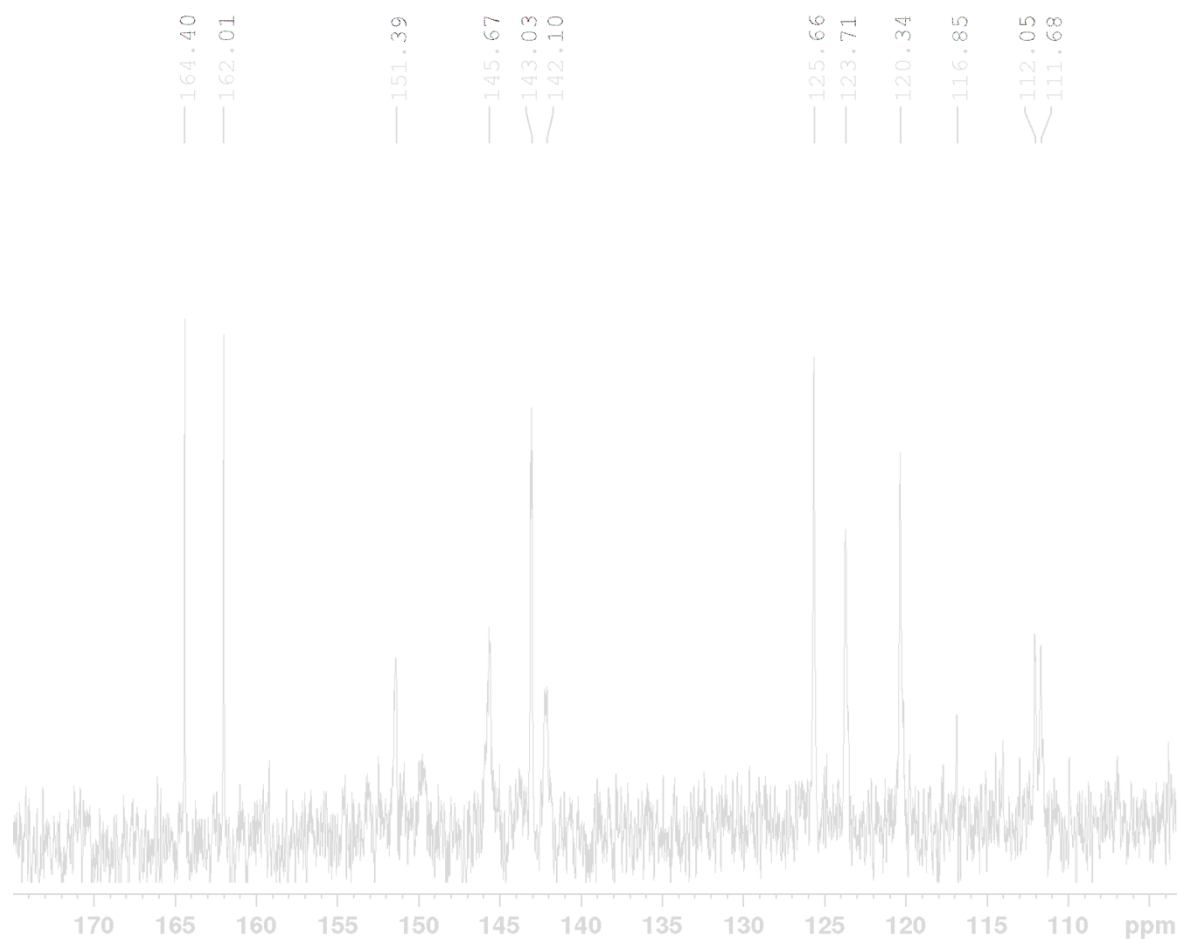


Figure S113.  $^{13}\text{C}$ -NMR spectrum of **6FBiPy** in  $\text{CDCl}_3$ , affording twelve signals in the aromatic region due to two additional signals appearing from two of the ten carbon atoms exhibiting observable coupling with the  $^{19}\text{F}$  nucleus present in the molecule.

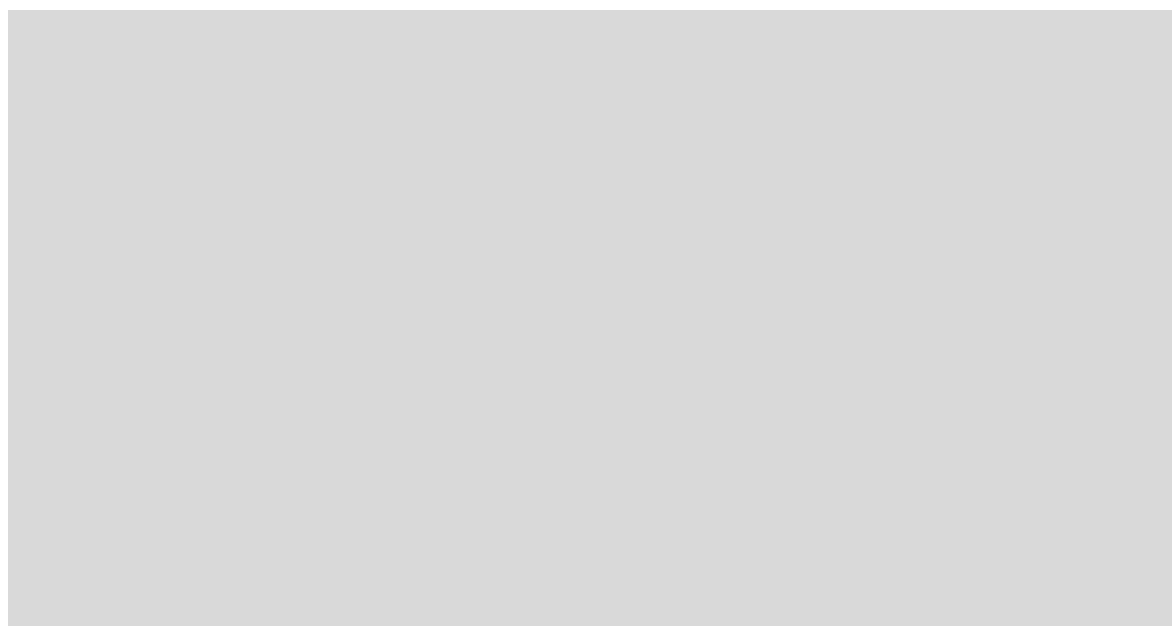


Figure S114. CPD  $^{19}\text{F}\{^1\text{H}\}$ -NMR spectrum of **6FBiPy** in  $\text{CDCl}_3$ . The signal at -106.00 ppm is the *para*-DFB internal standard.

## S.8 Instruments and Reagents

NMR analyses were performed using a Bruker Spectrospin 400 MHz UltraShield NMR spectrometer. Fourier transform infrared (FTIR) analyses were performed using a Bruker ALPHA-p IR spectrometer. UV-Vis analyses were performed using an Agilent technologies Cary 100 UV-Vis spectrometer. MP analyses were performed using a Stanford Research Systems Optimelt automated MP system with digital imaging processing technology. Low resolution mass spectrometry (LRMS) analyses were performed using a Waters micromass ZQ, equipped with an electrospray ionisation (ESI) source running in positive ionisation mode with the following parameters applied; voltages: 3 kV capillary voltage, 25 V cone voltage for organic molecules or 70 V cone voltage for rhenium complexes (required to dissociate Re–Br & Re–Cl bonds), 5 V extractor voltage and 0.2 V radiofrequency (RF) lens voltage; Temperatures: 45 °C source temperature and 300 °C desolvation temperature; and gas flows: 350 L.h<sup>-1</sup> desolvation nitrogen gas flow and 90 L.h<sup>-1</sup> cone nitrogen gas flow. Samples for HRMS were sent to the mass spectrometry user resource and research facility at the University of Wollongong and samples for EA were sent to the Campbell Microanalytical Laboratory at the University of Otago. All synthetic reagents were purchased from Sigma-Aldrich except for trifluoroacetic acid (TFA) and 18-crown-6 ether which were purchased from Alfa Aesar. Any precursor compounds whose syntheses are not described herein were additionally purchased from Bepham. Finally, all solvents were purchased from Merck and any water used for syntheses and analyses were first purified using a Merck Millipore Milli-Q integral water purification system.

## S.9 Microfluidic Set-up

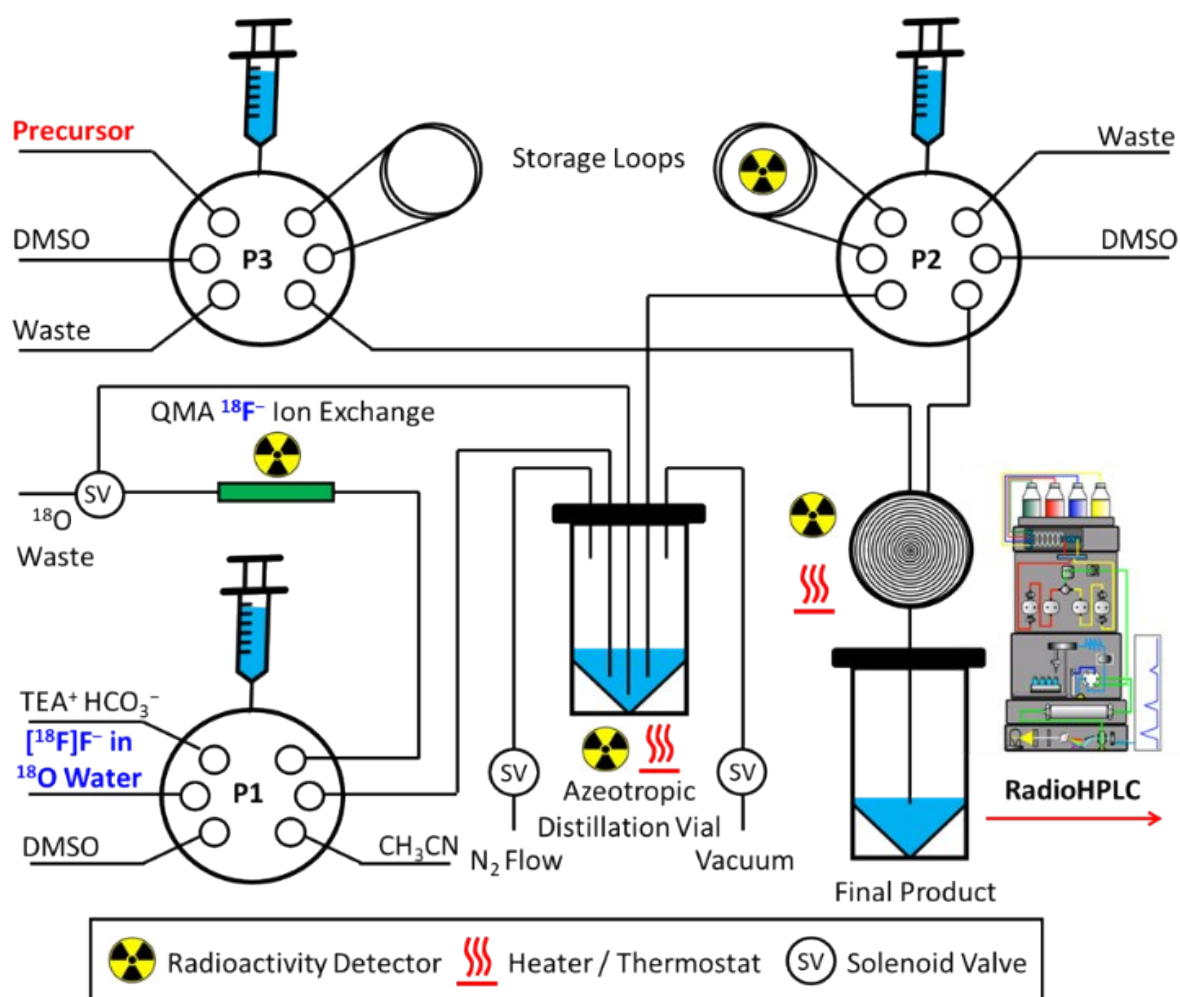


Figure S115. Automated synthesis module for the azeotropic drying of cyclotron generated [<sup>18</sup>F]fluoride and subsequent microfluidic set-up for the rhenium complexation-dissociation reactions under varying reaction environments.

Each precursor was reacted under microfluidic conditions using an automated synthesis module assembled as per the schematic in Figure 1.<sup>19</sup> Herein cyclotron generated [<sup>18</sup>F]fluoride was trapped on an ion-exchange cartridge and eluted to an azeotropic distillation vial using a solution of tetraethylammonium (TEA) bicarbonate in acetonitrile/water (9:1) solution. *Dry* reaction conditions were then achieved by azeotropically drying the [<sup>18</sup>F]fluoride complex *via* the heated dropwise addition of acetonitrile followed by reconstitution in anhydrous DMSO to enhance the nucleophilicity of the fluoride. Whereas *wet* reaction conditions omitted this distillation step and thus consisted of a 10% v/v content of water in acetonitrile. Both the [<sup>18</sup>F]fluoride (29±10 MBq) and precursor solution in DMSO (0.08 μmol) were then dispensed concurrently from pumps 2 and 3 (P2, P3) through a heated microreactor (15.6 μL) at a total rate of 20 μL.min<sup>-1</sup> (47 s reaction time). Reaction temperatures between 50 and 190 °C were trialed for each experiment in 20 °C increments. The solution was then dispensed into a final product vial where the solution was subsequently analysed by radioHPLC and/or radioTLC to determine the non-isolated RCYs of the radioproducts.



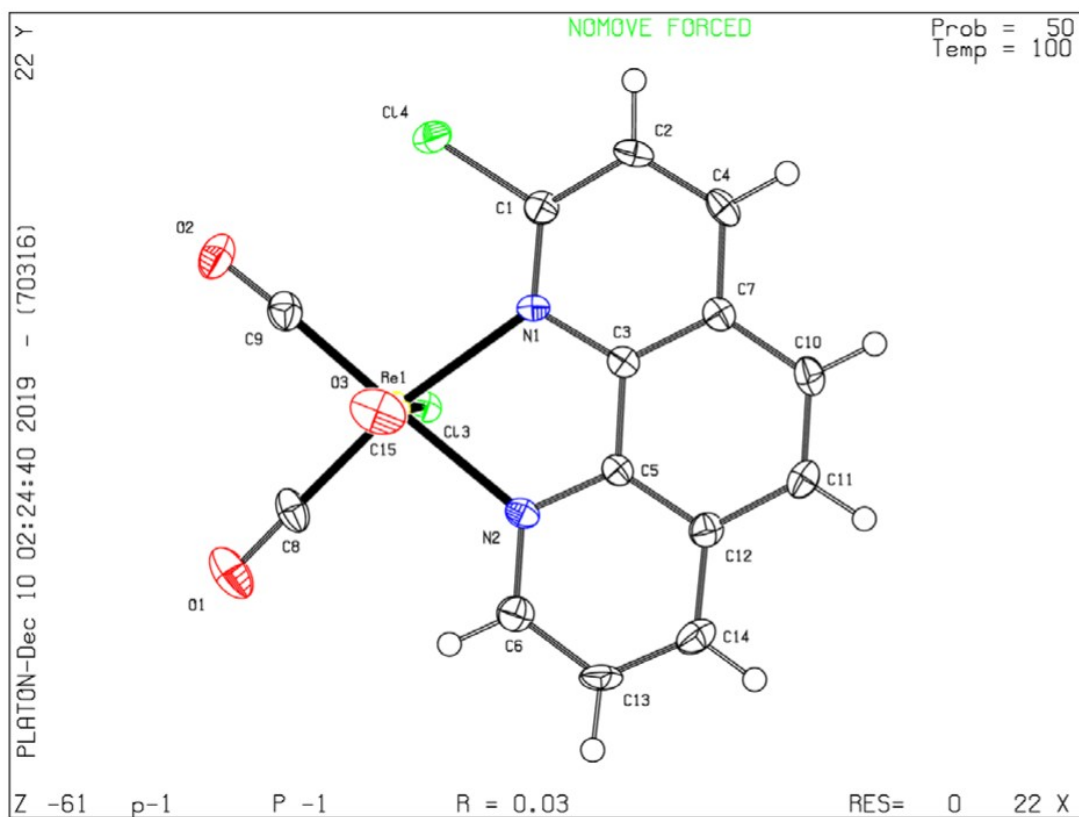


Figure S117. Ellipsoid plot for **Re<sub>2</sub>ClPhen**.

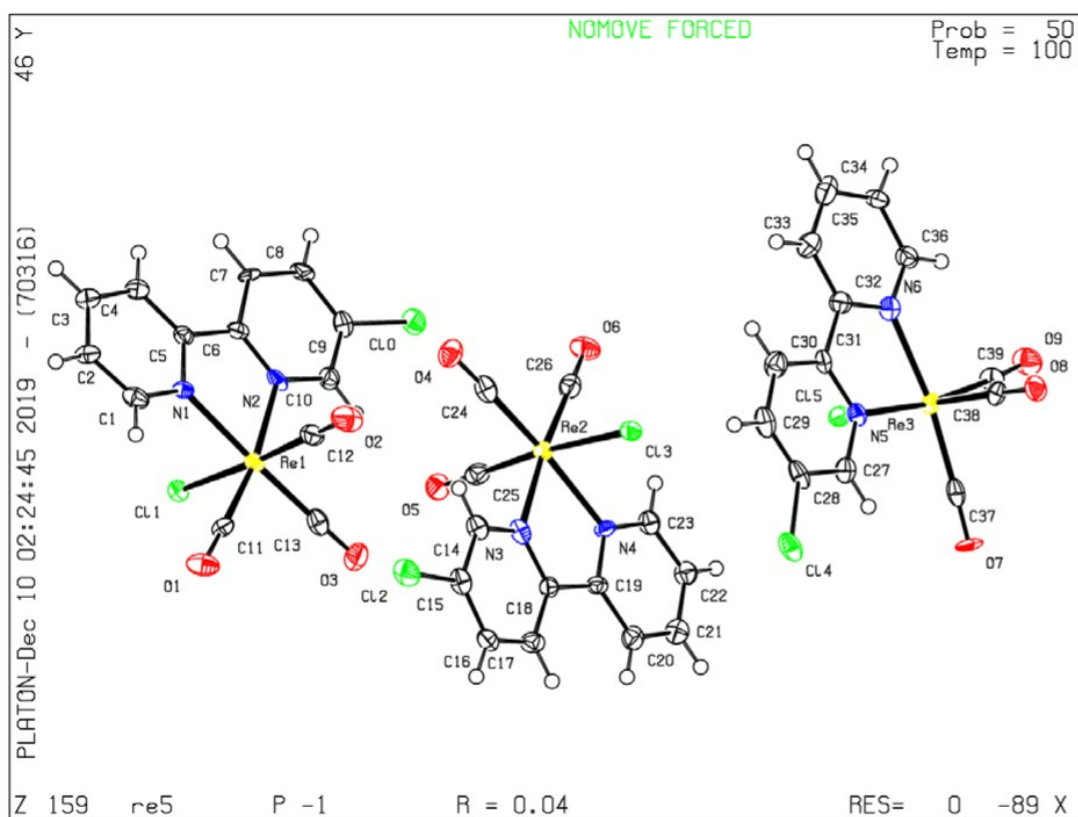


Figure S118. Ellipsoid plot for **Re<sub>5</sub>ClBiPy**.

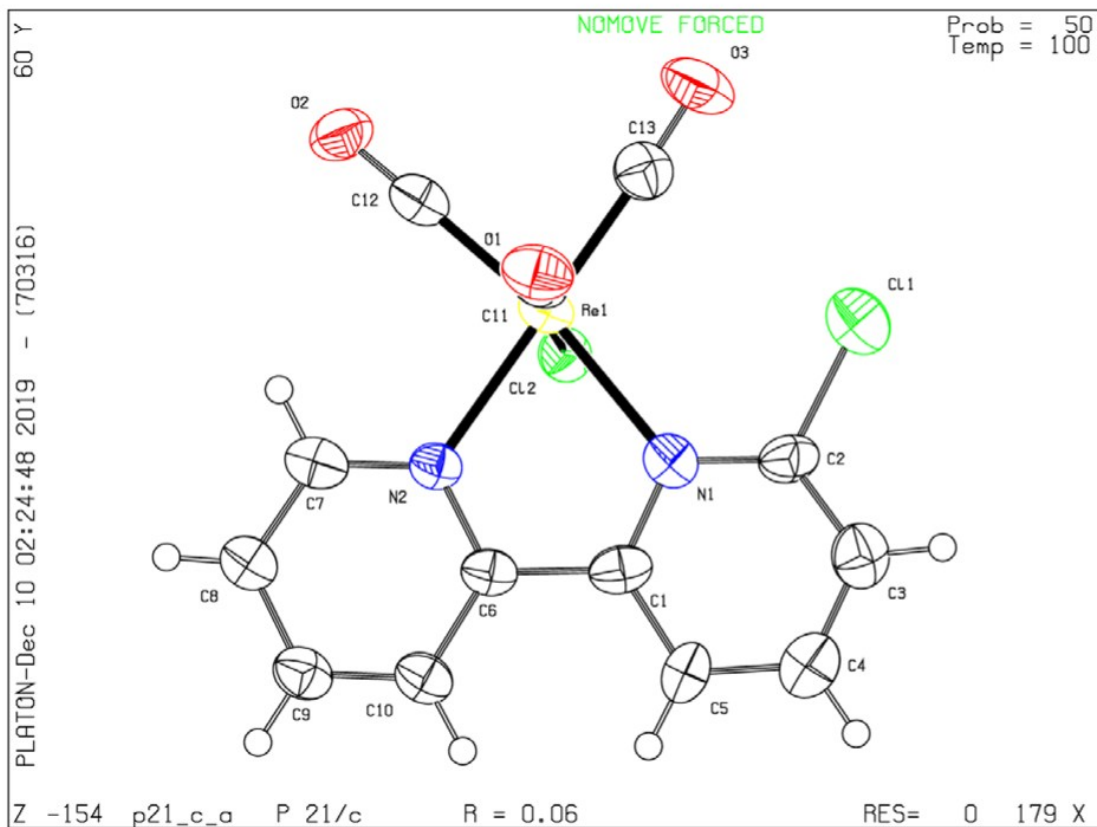


Figure S119. Ellipsoid plot for **Re6ClBiPy**.

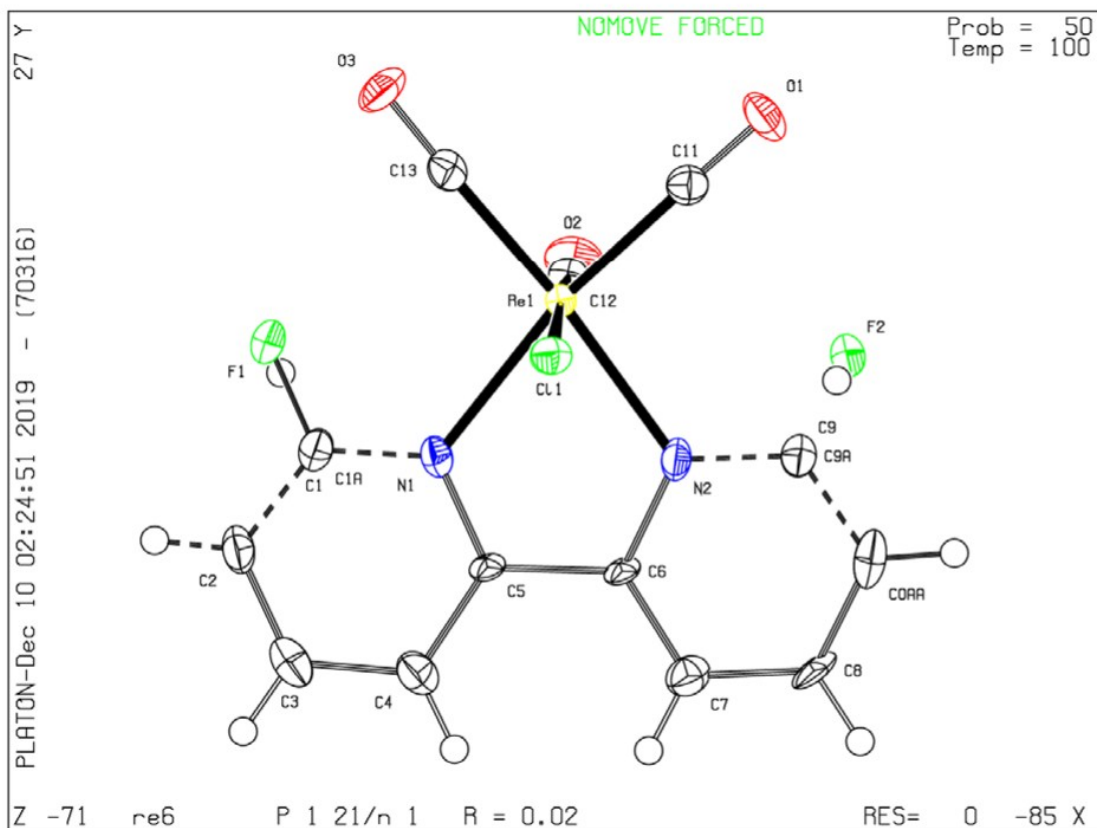


Figure S120. Ellipsoid plot for **Re6FBiPy**.

## S.11 References

- (1) Neese, F. Software Update: The ORCA Program System, Version 4.0. *Wiley Interdisciplinary Reviews: Computational Molecular Science*. Wiley Periodicals, Inc. July 17, 2017, p e1327.
- (2) Becke, A. D. Density-Functional Thermochemistry. V. Systematic Optimization of Exchange-Correlation Functionals. *J. Chem. Phys.* **1997**, *107* (20), 8554–8560.
- (3) Grimme, S.; Antony, J.; Ehrlich, S.; Krieg, H. A Consistent and Accurate Ab Initio Parametrization of Density Functional Dispersion Correction (DFT-D) for the 94 Elements H-Pu. *J. Chem. Phys.* **2010**, *132* (15), 154104.
- (4) Kendall, R. A.; Früchtl, H. A. The Impact of the Resolution of the Identity Approximate Integral Method on Modern Ab Initio Algorithm Development. *Theor. Chem. Accounts Theory, Comput. Model. (Theoretica Chim. Acta)* **1997**, *97* (1–4), 158–163.
- (5) Hay, P. J.; Wadt, W. R. Ab Initio Effective Core Potentials for Molecular Calculations. Potentials for K to Au Including the Outermost Core Orbitals. *J. Chem. Phys.* **1985**, *82* (1), 299–310.
- (6) Wadt, W. R.; Hay, P. J. Ab Initio Effective Core Potentials for Molecular Calculations. Potentials for Main Group Elements Na to Bi. *J. Chem. Phys.* **1985**, *82* (1), 284–298.
- (7) Klamt, A.; Schüürmann, G. COSMO: A New Approach to Dielectric Screening in Solvents with Explicit Expressions for the Screening Energy and Its Gradient. *J. Chem. Soc., Perkin Trans. 2* **1993**, *0* (5), 799–805.
- (8) Glendening, E. D.; Badenhop, J. K.; Reed, A. E.; Carpenter, J. E.; Bohmann, J. A.; Morales, C. M.; Landis, C. R.; Weinhold, F. *NBO 6 (Theoretical Chemistry Institute, University of Wisconsin, Madison, WI, 2013)*; [Http://Nbo6.Chem.Wisc.Edu/](http://Nbo6.Chem.Wisc.Edu/).
- (9) Mitoraj, M.; Michalak, A. Natural Orbitals for Chemical Valence as Descriptors of Chemical Bonding in Transition Metal Complexes. *J. Mol. Model.* **2007**, *13* (2), 347–355.
- (10) Belpassi, L.; Infante, I.; Tarantelli, F.; Visscher, L. The Chemical Bond between Au(I) and the Noble Gases. Comparative Study of NgAuF and NgAu<sup>+</sup> (Ng = Ar, Kr, Xe) by Density Functional and Coupled Cluster Methods. *J. Am. Chem. Soc.* **2008**, *130* (3),

- 1048–1060.
- (11) Bistoni, G.; Rampino, S.; Tarantelli, F.; Belpassi, L. Charge-Displacement Analysis via Natural Orbitals for Chemical Valence: Charge Transfer Effects in Coordination Chemistry. *J. Chem. Phys.* **2015**, *142* (8), 084112.
  - (12) Altun, A.; Neese, F.; Bistoni, G. The Effect of Electron Correlation on Intermolecular Interactions: A Pair Natural Orbitals Coupled Cluster Based Local Energy Decomposition Study. *J. Chem. Theory Comput.* doi: 10.1021/acs.jctc.8b00915.
  - (13) Nalewajski, R. F.; Köster, A. M.; Jug, K. Chemical Valence from the Two-Particle Density Matrix. *Theor. Chim. Acta* **1993**, *85* (6), 463–484.
  - (14) Nalewajski, R. F.; Mrozek, J.; Michalak, A. Two-Electron Valence Indices from the Kohn-Sham Orbitals. *Int. J. Quantum Chem.* **1997**, *61* (3), 589–601.
  - (15) Nalewajski, R. F.; Ozek, J. Modified Valence Indices from the Two-particle Density Matrix. *Int. J. Quantum Chem.* **1994**, *51* (4), 187–200.
  - (16) Blake, A. J.; Cockman, R. W.; Ebsworth, E. A. V.; Holloway, J. H. Novel Reaction of an Iridium Carbonyl Complex with Xenon Difluoride: The First Metal Fluoroacyl Complex. *J. Chem. Soc. Chem. Commun.* **1988**, *0* (8), 529–530.
  - (17) Klenner, M.A.; Pascali, G.; Zhang, B.; Sia, T.R.; Spare, L.K.; Krause-Heuer, A.M.; Aldrich-Wright; J.R.; Greguric, I.; Guastella, A.J.; Massi, M.; Fraser, B.H. A Fluorine-18 Radiolabeling Method Enabled by Rhenium(I) Complexation Circumvents the Requirement of Anhydrous Conditions. *Chem. Euro. J.* **2017**, *23*, 6499-6503.
  - (18) Wright, P.J.; Muzzilloi, S.; Werrett, M.V.; Raiteri, P.; Skelton, B.W.; Silvester, D. S.; Stagni, S.; Massi, M. Synthesis, Photophysical and Electrochemical Investigation of Dinuclear Tetrazolato-Bridged Rhenium Complexes. *Organometallics* **2012**, *31*, 7566-7578.
  - (19) G. Pascali, L. Matesic, T. L. Collier, N. Wyatt, B.H.Fraser, T. Q. Pham, P. A. Salvadori, I. Greguric. Optimization of Nucleophilic <sup>18</sup>F Radiofluorinations using a Microfluidic Reaction Approach. *Nat. Protoc.* **2014**, *9*, 2017-2029.